The infrared SEDs of starforming galaxies

by

Anna Sajina

B.Sc., The University of British Columbia, 2000
M.Sc., The University of British Columbia, 2002

A THESIS SUBMITTED IN PARTIAL FULFILMENT OF
THE REQUIREMENTS FOR THE DEGREE OF

DOCTOR OF PHILOSOPHY

in

THE FACULTY OF GRADUATE STUDIES

(Department of Physics and Astronomy)

We accept this thesis as conforming
to the required standard

.....

.....

.....

.....

THE UNIVERSITY OF BRITISH COLUMBIA

July 24, 2005

In presenting this thesis in partial fulfilment of the requirements for an advanced degree at the University of British Columbia, I agree that the Library shall make it freely available for reference and study. I further agree that permission for extensive copying of this thesis for scholarly purposes may be granted by the head of my department or by his or her representatives. It is understood that copying or publication of this thesis for financial gain shall not be allowed without my written permission.

(Signature) _____

Department of Physics and Astronomy

The University Of British Columbia
Vancouver, Canada

Date _____

ABSTRACT

The spectral energy distribution (SED) is one of the key observational features of galaxies. It allows us to both gain insight into the physical properties of galaxies and compare populations selected at different wavelengths or redshifts. In this thesis, we address all steps in the study of SEDs including how to constrain it from the available data, how to derive the underlying properties of the galaxies, and how to use it to interpret and predict survey data.

The first step is accomplished with a phenomenological SED model and MCMC fitting technique. General trends in the mid-IR spectra of a wide range of galaxy types are discussed as well as argument made for considering a continuum of SED shapes as opposed to discrete templates. Based on this approach, predictions are made for the evolution of diagnostic mid-IR colours.

We extend our model into the far-IR/sub-mm regime, and apply it to a sample of 22 170 μm-selected, star-forming galaxies representing the brightest $\sim 10\%$ of the Cosmic Infrared Background (CIB) contributors. The sample spans the range $\log(L_{\rm IR}/L_{\odot}) \sim 10-12$ and $z \sim 0-1$. From these model fits, and standard relations, we derive a host of underlying physical properties including: stellar mass, opacity, dust mass, dust temperature. These allow for direct comparisons with other samples of optical- or IR-selected star-forming galaxies, allowing us to explore in detail the nature of our sample.

We conclude by addressing the implications of our study to other IR-selected samples. In particular, we discuss the possible nature of the remaining $\sim 90\%$ of the CIB contributors.

CONTENTS

LIST OF TABLES

LIST OF FIGURES

Acknowledgements

Thanks to all my callaborators on various aspects of this thesis Douglas Scott, Mark Lacy and the FIRBACK team. Thanks to N. Lu and the SWIRE team for the use of their data. Many thanks especially to Douglas Scott for a careful reading of the text and many comments. Many thanks to the makers of CSI, my cat, and whoever invented wine for keeping me sane during the writing of this thesis. Lastly, many thanks to my mother who gets to hear more about astronomy than she ever cared to.

CHAPTER 1

INTRODUCTION

1.1 Astronomical context

One of the major directions in current astronomical research involves understanding how galaxies, the building blocks of the Universe, formed and evolved (for a review see [130]). Present-day galaxies fall into two broad categories, which we will call blue and red. Blue galaxies are less massive, have smaller surface brightness, and are actively forming stars (particularly strongly in some dwarfs), while red galaxies are more massive, have more concentrated light profiles, have older stars, usually little or no current star-formation and typically host AGN [85]. The mass scale dividing the two categories is $\sim 3\times 10^{10}\,\mathrm{M}_{\odot}$, which might be governed by the efficiency of feedback mechanisms (i.e. galactic supernovae-driven winds) [31]. Related to the above, there are two broad morphological classes: spheroids (i.e. ellipticals) and disks (with combinations thereof). Irregular morphologies are typical of the least massive dwarf galaxies, or are the extremely rare major mergers of comparably sized spirals caught in the act of merging. While the large elliptical galaxies, which contain the bulk of the present-day stellar mass, have fairly homogeneous populations, spirals show a range in age, and metal abundance [112]. Overall, nearby galaxies are fairly quiescent, which led to the initial assumption that this was always so, and that galaxies simply collapsed from primordial gas clouds and have been quietly converting their gas into stars ever since [49]. Was this really the case, and if not how and when were all these stars formed, and what processes govern the diversity in physical properties of

the local galaxy populations? The study of galaxy formation and evolution has been largely

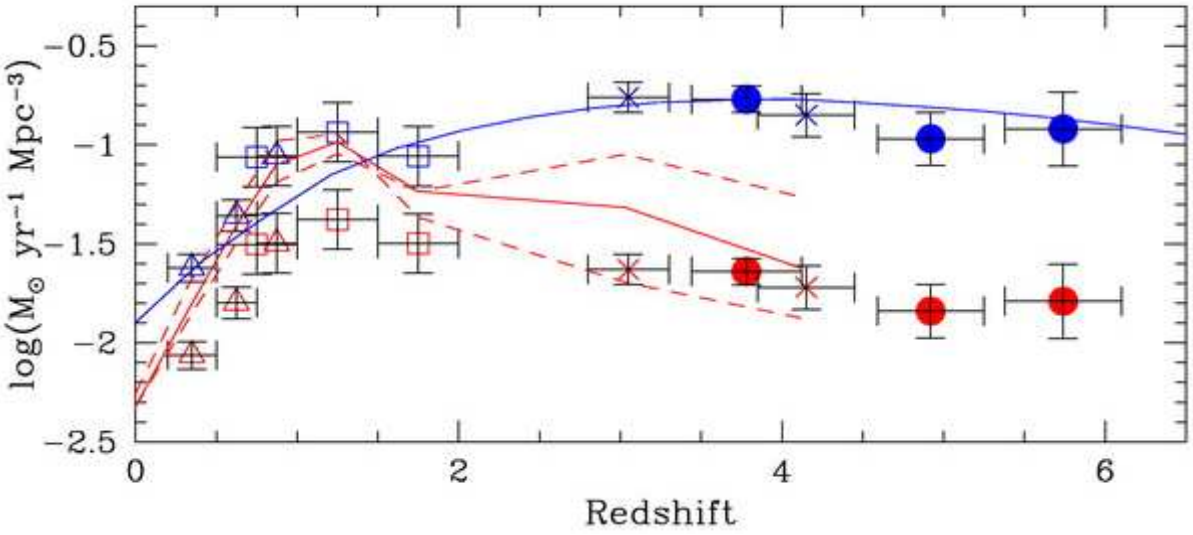

Fig. 1.1: A recent compilation of the star-formation rate density evolution [58]. The open symbols are averages of different estimates, while the filled symbols are the Giavalisco et al. [58] estimates from the GOODS survey. The blue symbols are the same as the red ones, but corrected for incompleteness. The blue line is the prediction of a semi-analytic model of galaxy evolution [161], while the red line and uncertainties are the estimates of Pei et al. [128] based on a study of Lyman Alpha forest abundances.

driven by the availability of high quality optical data; however, a complete understanding requires a multiwavelength approach, with the infra-red playing a particularly important role. Ultraluminous Infrared Galaxies (ULIGs; defined as having $L_{\rm IR} > 10^{12} L_{\odot}$), discovered by *IRAS* in the 1980s, first showed the existence of massive, extremely dusty galaxies hiding prodigious star formation activity (on the order of $100\,{\rm M}_{\odot}$/yr compared with the present-day Milky Way $\sim 1\,{\rm M}_{\odot}$/yr) [152], and were later shown to be associated with major mergers with the most luminous of them harbouring AGN [174]. Meanwhile, technological advances allowed surveys

to reach cosmologically significant redshifts for the first time. These indicated a dramatic rise in the Star Formation Rate (SFR) density of the Universe between today and redshift 1 [108] (see Fig. *1.1*). The Cosmic Infrared Background (CIB) discovered with the DIRBE and FIRAS instruments on *COBE* in 1996 [138] required, in particular, a dramatic rise in the importance of dusty/starforming sources at $z > 0$. Soon afterward, in 1997/98, there followed the discovery, with SCUBA on the JCMT, of sub-mm galaxies [79], whose redshifts were inferred to be $z \sim 2$ and consequently their luminosities have to be ULIG-class. At roughly the same time a relationship was established between the masses of black holes and their host bulges [114]. This apparent connection between the feeding of an AGN and the surrounding starformation is further strengthened by the discovery that the hosts of more luminous AGN have younger stellar populations than fainter AGN [86]. All these discoveries led to the realization that the Universe of the past contained a different mix of galaxies than today, contrary to the monolithic formation scenario.

An alternative, the hierarchical galaxy formation picture implied by the cold dark matter paradigm [171, 11], has been developed since the 1980s as a successful model for the build-up of galaxies. As part of that picture, it has long been suggested that the massive present-day ellipticals formed by the merger of two spirals [172], and therefore a picture began to emerge whereby sub-mm galaxies are these merger-induced vigorous starformers – the future massive ellipticals and their active nuclei. However, this Universe-of-the-giants was not reinforced when the question of the CIB contributors was addressed by the FIRBACK survey [37]. If such extreme galaxies had contributed to the bulk of the CIB at its peak, the FIRBACK survey would have resolved it. Instead only ∼10% was resolved, mostly in local quiescent galaxies (see Section 4.1). A model in which the more modest Luminous Infrared Galaxies (LIGs;

defined as having $L_{IR} > 10^{11}\,L_{\odot}$) at $z \sim 0.5-1.5$ are responsible for the remaining $\sim 90\%$ is consistent with these findings (for a review see [101]). LIGs are not scaled-down ULIGs, since they are not associated with major mergers (although may be triggered by minor mergers), but are more likely a result of the greater gas density in the past, which naturally leads to greater star-formation activity regulated by feedback mechanisms such as observed locally in gas-rich dwarf galaxies [60, 31]. Spiral galaxies are thus expected to be, on average, gradually winding-down their star-formation, for example the Milky Way has potentially had LIG-like SFRs at $z \sim 1$ (based on the ages of the thin disk and bulge stars [61]). In fact the most strongly evolving population since $z \sim 1$ is that of the luminous blue compact galaxies (LBCGs) [94], which apparently dominate the SFR density of the Universe at intermediate redshifts and probably represent a significant fraction of the present-day spiral galaxy bulges in formation (implying late disk growth) [66]. Their star-formation is believed to be fed via infall from close companions, resulting in the abundance spread observed in present day bulges. Although not directly observed, their infrared luminosities are believed to be $\sim 10^{11}\,L_{\odot}$ [66] and thus might be the sought after population. A recent closer comparison between $z \sim 0$ and $z \sim 1$ galaxies suggests that the increase in the SFR density at the later epoch is most likely due to a modest increase in the average SFR of regular spirals (e.g. LIGs) rather than major mergers [7]. This is consistent with the above scenario for the LBCGs, implying that the bulk of the spiral galaxies disk stars are formed at $z < 1$. At higher redshifts, the relative contribution of modest starbursters (e.g. Lyman Break Galaxies, or LBGs) and extreme ones (e.g. SCUBA galaxies) is still unclear. Theoretical models [161] support the idea that minor mergers contributed to the bulk of the SF in the Universe at least in up to $z \sim 2$. But we might not be in a position yet to answer this question, as there are suggestions that we still have not observed the

bulk of the stars at $z \sim 1-2$ [118]. Apparently, contrary to the classical hierarchical structure formation paradigm the existence of highly evolved galaxies at very early epochs has been observed including massive, dusty quasars at $z \sim 6$ [144]. Two separate problems exist here, one of which is that this amount of dust (implying high metallicity and AGB dust shells which are older than the Universe at the time) should not exist so early (but see [45]). Secondly, if quasars form as part of the formation of the most massive galaxies then these particular halos appear to have collapsed quickly and largely monotonically as there is no time for the gradual build-up by merging (although it is possible given recent results suggesting that the $M_\bullet/M_{\rm halo}$ might have been much higher at the time [178, 163]). In fact, recently, it has become evident that the Universal SFR is experiencing 'downsizing' or the bulk of the star-formation activity (which is Universally decreasing) is also gradually shifting from more massive to less massive galaxies [70, 84]. The emerging picture is one where the densest regions after the CMB collapsed first (see for e.g. [163]) where the higher density of sources led to much higher (especially major) merger rates early on and thus the bulk of the stars at the time were formed in brief, violent episodes. This results in the early quasar epoch, the fairly homogeneous (predominantly old) populations of present-day ellipticals, their relative lack of an ISM, and the density-morphology relation. By contrast, less dense regions collapse late and appear to form their stars in a less extreme, largely self-regulated manner, thus the above downsizing is not due to the least massive galaxies changing at all,[1] but rather in the more massive ones exhausting their star-formation fuel supply too quickly and thus aging quietly since the initial violent star-formation event [84].

The synthesis of all of these ideas and pieces of observational data leads to the conclusion

[1]Except for the caveat that in the smallest haloes star-formation cannot start at all until the ambient UV background has dropped sufficiently [140] and after a brief burst of SF, strong galactic winds can expell the entire ISM halting future star-formation [31].

that although we understand much of the process of galaxy formation and evolution, the picture is far from complete. The resolution of many of the remaining issues requires multi-wavelength observations in the infrared and their careful interpretation, which is the subject of this thesis.

1.2 Understanding the infrared SEDs of galaxies

The Spectral Energy Distribution (SED) denotes the power (per unit wavelength or frequency) emitted by a galaxy. It is the sum of all possible contributors: both emitters such as stars and active galactic nuclei (AGN) and distributors (i.e. dust). We gain insight into the galaxy's properties both by studying the overall shape of the SED (determining the heating source and dust properties), its amplitude at various bands (determining the masses of various components), and its integrated emission (i.e. total power output). Apart from learning more about the particular galaxies under study, knowing the SED shapes of different types of galaxies, the extent to which these can vary and the proportions of each type is a crucial discriminant of galaxy evolution models. These usually start with a well understood local luminosity function and apply some prescription(s) for its evolution with redshift using some assumed SED(s) in order to predict the moments of the dN/dS distribution, which are the source counts, background intensity and fluctuations (see e.g. [99]). The various prescriptions are tested by comparing these predictions with observations from blank-sky surveys at various wavelengths. In this procedure, there is an inherent *degeneracy between the SED shapes and the LF evolution.* A final reason for understanding SEDs is that knowledge of the SED is of crucial importance when we select sources from images with often dramatically different spatial resolution, and assign the resulting sources to their appropriate epoch (i.e. determine photometric redshifts). The above considerations motivate us to seek both a greater understanding of galaxy SEDs and better

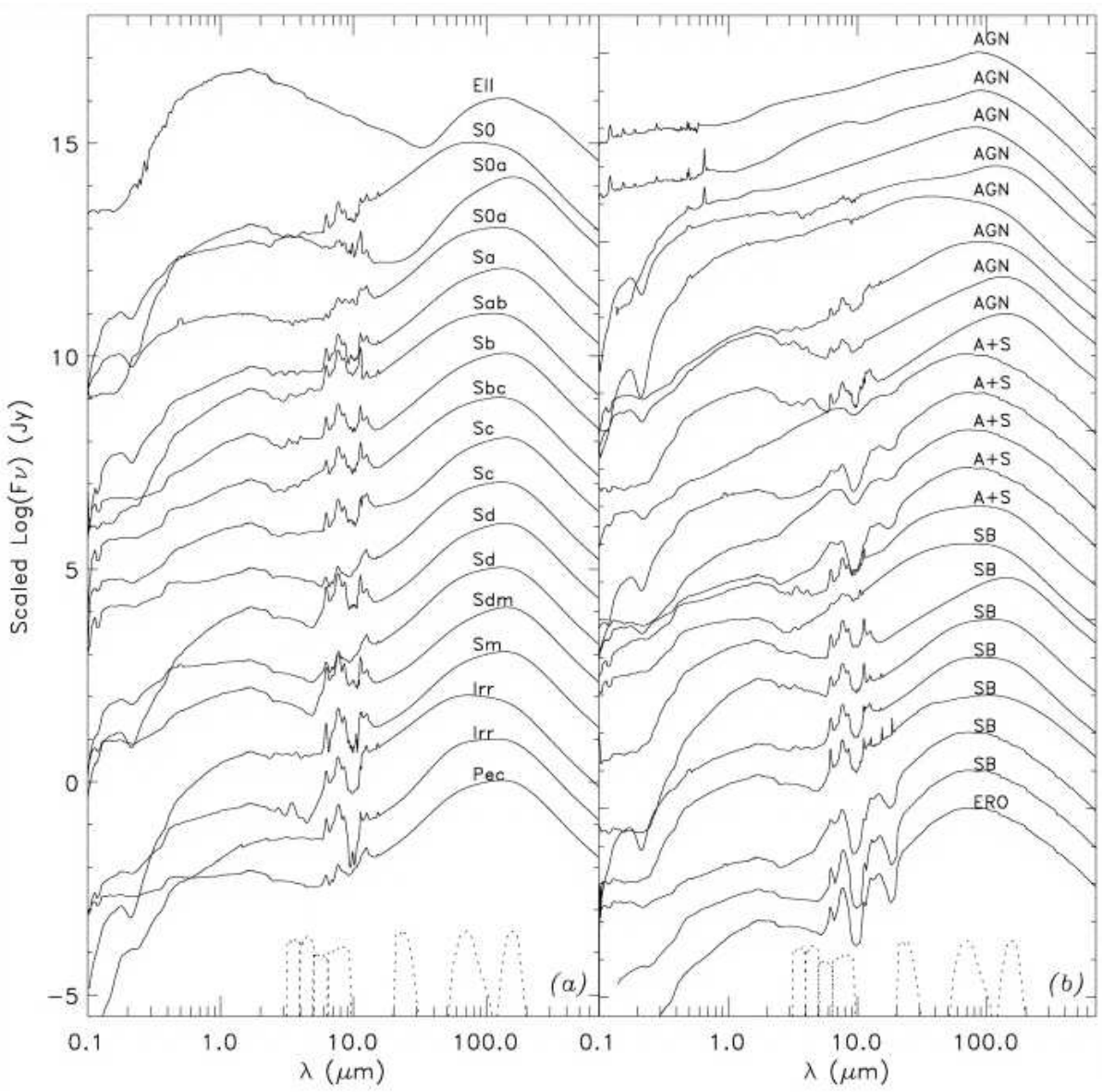

Fig. 1.2: The SWIRE galaxy template library compiled from observations and models [110], where quiescent galaxies are on the left and more active ones are on the right. The dashed curves at the bottom are the *Spitzer* IRAC and MIPS filters (see Chapter 2).

ways to model and fit these SEDs so that we can quantify the range allowed by the available data, and consequently arrive at meaningful uncertainties to the various physical parameters inferred.

Below we begin by drawing a sketch of the processes behind dust formation, and how it is linked to the lifecycles of the stars. We follow with an outline of the principle features of the 1–1000 μm infrared spectra of galaxies, followed by an overview of our modelling/fitting philosophy in comparison with other approaches.

1.2.1 Star-formation and the ISM

For the purposes of this thesis, it is important to have a basic understanding of the interplay between star-formation and the Interstellar Medium (ISM). A simplified picture of the ISM involves a cold, neutral, diffuse medium permeating the galaxy. Embedded in this are giant molecular clouds (GMCs). Star-formation is thought to occur in dense cores inside these, although the exact process is still poorly understood. The young, UV-bright stars ionize the medium around them into the so called HII regions (the intense UV radiation therein also destroys the unshielded dust grains). The interface between these regions and the surrounding GMCs are the photo dissociation regions (PDRs), where smaller grains are close enough to be excited by but not destroyed by the UV photons. These grains experience stochastic heating whereby a single photon hit can excite the grain, which then re-radiates the energy into the infrared in discrete vibrational modes. Whatever photons escape these stages can be absorbed by the bigger grains further out. The most massive stars end their life as supernovae, and many new grains form in their winds while the shocks imparted to the surrounding GMCs can stir them into the next cycle of star-formation. The less massive stars in time diffuse out of the

clouds and, in the later stages of their evolution, become unstable and begin to lose their mass. The vast majority of ISM particles form in their ejecta based on the composition of the outer layers of these stars (i.e. carbon- or oxygen-rich). Even after the young/massive stars have died out, these older stars contribute to a less-energetic, but ominpresent interstellar radiation field (ISRF), which also contributes to heating the dust grains. The relative contribution of UV and optical photons to heating the dust averaged over the entire galaxy is unclear (we return to this point in Chapter 4). For further discussion on the lifecycle of dust see [47].

1.2.2 Spectral features

Fig. *1.1* shows a state-of-the-art compilation of galaxy SED templates constructed from a combination of observations and models, where the basic features and their variation between galaxy types is evident.

The 1–3 μm near-IR is dominated by the 1.6 μm peak of old stellar populations in virtually all galaxies except AGN-dominated sources and heavily extincted ULIGs. This peak arises due to the characteristic temperatures of the atmospheres of red giants which dominate the emission. The ubiquitous break at 2.3 μm arises from CO absorption in the outer layers of these cool stars.

The 3–60 μm mid-IR spectral band lies at the interface between the regimes where one observes stellar light directly and where one sees that light reprocessed by dust and gas. The main contributors to galactic emission at mid-IR wavelengths are light from old stellar populations [12], Polycyclic Aromatic Hydrocarbon (PAH) emission features [137, 78], and power law continuum emission, which is, in particular, the dominant component in the mid-IR spectra of AGN-dominated sources [24]. This last contribution is likely due to stochastically-heated

very small grains [33]. The PAH emission is thought to arise in photo-dissociation regions as discussed above. These sources of emission can be extincted by dust, and further attenuated by discrete absorption features, in particular those from water ice (at $\sim 6\,\mu$m), and Si (at $\sim 10\,\mu$m). We show a typical extinction curve in Fig. *1.2.2*. Other possible contributors include: Asymptotic Giant Branch (AGB) stars' dust shells; a near sublimation temperature ($\sim 1000\,$K) blackbody component [111]; molecular cooling lines; and nebular lines. The outer boundary of what we call 'mid-IR' is rather fuzzy and depends on the source: warm sources are more dominated by their mid-IR emission than cooler sources where the mid-IR is suppressed overall with respect to the far-IR.

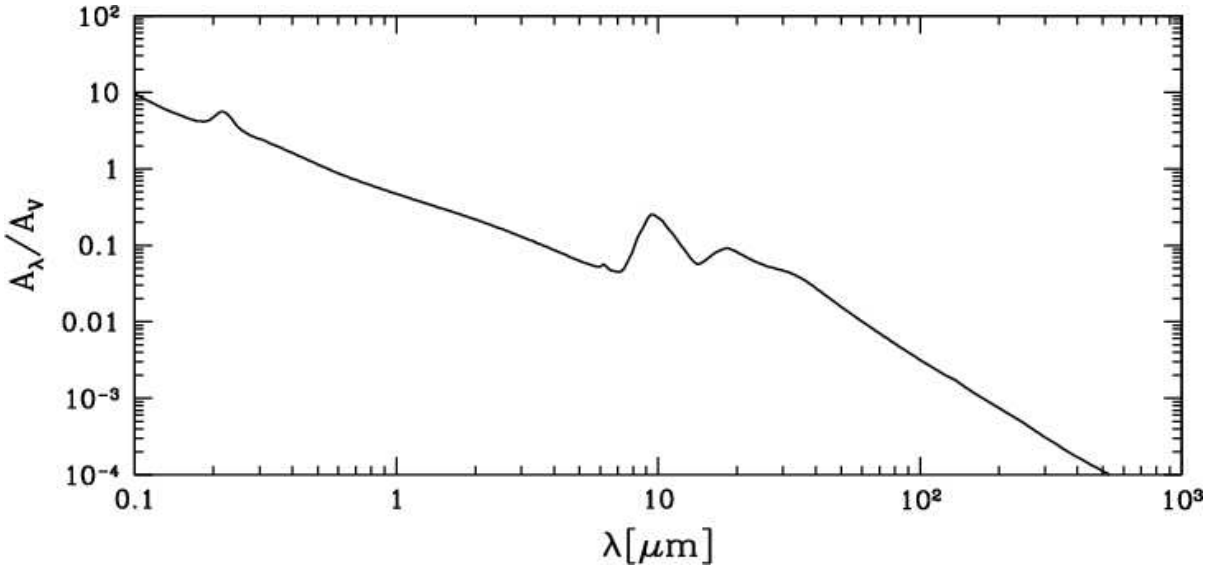

Fig. 1.3: A model extinction curve based on a Milky Way type ISM [41]. This is the curve we use throughout this thesis. The y-axis shows the extinction in magnitudes per wavelength (A_λ) relative to that in the $\mathcal{V}$ band.

The $\sim 60-1000\,\mu$m far-IR/sub-mm band is the regime of thermal dust emission (except for some extreme AGN sources where it can be largely synchrotron emission). Dust of varying sizes

and optical properties is distributed both diffusely in the ISM, and in clumps within GMCs. Thus a continuum of equilibrium temperatures and emissivities contribute to this emission. The prominent far-IR peak (see Fig. *1.1*) shifts to shorter wavelenghts for more active sources and longer wavelengths for more quiescent ones. The characteristic temperature is therefore related to the overall power emitted by the dust (and absorbed from young UV-bright stars). Barring highly-clumped dust, this emission is proportional to the overall dust content since the big grains dominate the mass budget. The shape of the Rayleigh-Jean tail leads to a so called negative k-correction[2], which is highly favourable for sub-mm observability of dusty, high-z sources.

Traditionally, studying the entire $1-1000\,\mu$m range at once has been difficult, since mid-IR ($<60\,\mu$m) observations could not reach much beyond the local Universe, while sub-mm observations also only exist for very local, IR-bright, galaxies [44], or else SCUBA-selected sources which peak at $z\sim2-3$ [21]. The latter typically have only one or two detections outside the single SCUBA ($850\,\mu$m) one, which makes their interpretation particularly dependent on the SED model assumed [9]. Due to these past observational limitations, we still do not know (beyond some generalized trends) the full range of galaxy SED shapes, how exactly they are related to the underlying physical conditions in the galaxy, and therefore how they may vary across cosmic time as the galaxies evolve. With the advent of the *Spitzer* Space Telescope (see Chapter 2) [176] we can for the first time observe the mid-IR properties of large numbers of sources over a cosmologically significant range in z [110]. *Spitzer* covers the range 3–$160\,\mu$m,

[2]A k-correction is accounting for the fact that the emission from a galaxy observed through a given filter was in fact emitted at a shorter wavelength, where $\lambda_{\rm rest}=\lambda_{\rm obs}/(1+z)$. A negative k-correction occurs when $\lambda_{\rm rest}$ climbs into parts of the SED with greater intrinsic emission than $\lambda_{\rm obs}$, counteracting the usual $1/r^2$ dimming, such that distant galaxies appear of the same or even higher brightness as local ones.

although because of the difference in data quality, in practice only the 3–24 μm data are very cosmologically useful. The obvious next step toward characterizing the full infrared SEDs of galaxies is therefore to link *Spitzer* observations with longer wavelength samples, especially including sub-mm observations. The quality and quantity of the available sub-mm data are the limiting factor here.

1.2.3 Modelling approaches

There are three basic methods for modelling galaxy SEDs: use of observational templates, use of simplified galaxy models mimicking the physical processes in galaxies, or empirical relations matching the shape of the SED (see also [135] and references therein).

The first is often the method of choice if the question asked is whether some source(s) appears more like this or that well known local galaxy. It is therefore very useful in roughly but quickly assessing the nature of the source as in: 'the galaxy appears to have an M82-like (i.e. starburst) spectrum rather than a Mrk231-like spectrum (i.e. AGN)'. The major shortcoming of this approach is that this is about the extend to which this approach takes us. We often derive physical parameters for a galaxy from empirical relations with the whole or parts of their SEDs. Since the agreement with these templates is usually not perfect, using them increases the uncertainty in these derived parameters. Moreover, especially as we go to higher redshifts, this approach makes us less able to assess any but the grossest SED differences with respect to these local 'analogues'. The availability of observations in different parts of the spectrum is strongly dependent on the availability of instruments – there are obvious differences in aperture and resolution as well. To overcome some of these problems, panchromatic SED libraries can be constructed by combining observed and theoretical spectra (see Fig. *1.1*; [110]).

The second method to a large extend addresses the origin of a galaxy's SED. By constructing simplified galaxy models containing both the primary energy sources (stars and AGN) and embedding them in some reasonable ISM mixture, which absorbs some of this power and re-emits it in the infrared according to the grain properties. In this way the basic features of galaxies SEDs can be reproduced. Such models are very useful in theoretical work such as when trying to predict the observable properties of galaxies from cosmological simulations (e.g. [158, 5]), but especially to try to understand more robustly what relative geometric distributions of the dust and stars, and physical properties of the grains for example are most consistent with the observations (e.g. [134, 39]). This approach has the attractiveness of mimicking the actual processes in galaxies. It is important to remember however, that since a true physical model of these processes does not in fact exist all such models are merely approximations with many hidden or nor tunable parameters. The range of SED shapes observed in reality (see e.g. Fig. *1.1*) still far exceeds their predictions highlighting the much greater complexity found in nature. Until we fully understand how a galaxy truly works, complete reliance on such models (despite their obvious uses) is therefore not advisable.

Lastly, empirical SED-fitting involves defining some functional form which is believed to reasonably well describe the SED shapes of the sources of interest. Then an optimization can be performed in order to obtain the best-fit parameter values for a given galaxy (for e.g. see [44, 29, 9]). This method allows us to compare different samples of galaxies as in the first method; however, it also allows for a much closer fit to actual SED shape as it has much greater flexibility without the local bias. This procedure, unlike the second one, tells us nothing directly of the underlying properties of the galaxy – we must rely on empirical relations to derive those. However, in allowing us to extract the most information out of the available data, this approach

is quite an attractive tool in confronting observations with theories on the processes behind the SED generation.

Frequently, the three methods overlap since, often the second method provides template libraries used in the first [80, 182], the third often is a collection of shapes for the whole or part of the SED either from the observational templates or theoretically-derived ones [102]. The second method includes models which vary greatly in complexity, but nearly always use some simplifying assumptions, or embedded empirical relations for some parameters [158]. The third approach on the other hand tries to use physically-motivated parameterizations (e.g. [29]).

In this thesis we choose the third method, which as stated above, is the best for determining the SED shape(s) allowed by the data.

1.3 Thesis outline

Motivated by the above ideas, this thesis describes several different aspects of the IR SEDs of star-forming galaxies and their applications.

First we look for ways to describe the mid-IR spectra of a wide-range of galaxy types (from elliptical to AGN) with a minimum number of free parameters. The resulting model is used to simulate the *Spitzer* mid-IR colour-colour diagrams, including variations with redshift (Chapter 3).

The above modelling approach is extended to the far-IR/sub-mm regime and applied to a sample of 22 170 μm-selected galaxies (Chapter 4). The SED fits allow for their physical properties to be extracted and compared with those of known local populations. These fits also allow us to characterize the appropriate SED shapes more robustly and compare with existing models.

In Chapter 5, these results are discussed in light of current surveys, especially using *Spitzer*. Finallly, we use the full infrared SEDs and return to the idea of using the colour-colour diagrams directly for constraining evolutionary models. This allows for some further speculations on the nature of *Spitzer* selected galaxies and their possible relation to the galaxies contributing to the bulk of the CIB.

A summary of this thesis, and future work stemming from it are left for Chapter 6.

Lastly, we include two appendices, where Appendix A describes the Markov Chain Monte Carlo (MCMC) technique which we use here, and Appendix B contains some results and discussion on infrared-based photometric redshifts.

CHAPTER 2

OBSERVING IN THE INFRARED

In this thesis, we define the infrared regime as the $\sim 1-1000\,\mu$m wavelength range[1]. Observations in this range are complicated by the fact that, apart from the desired astronomical source, nearly everything inbetween, including the instrument, the earth, the Solar System and the Milky Way, emits in the infrared. In this chapter we briefly outline the various astronomical foregrounds that need to be kept in mind. We follow this with a description of the instruments used in this thesis, how they address the above foregrounds and how they compare with each other.

We conclude with an outline of some of the major past, present and future surveys which are the backbone of extragalactic infrared astronomy.

2.1 Foregrounds

Note that the effects described here are usually misleadingly called 'backgrounds', which convention we also occasionally use. For a review of the night sky emission see [104].

[1]We also will frequently refer to the common sub-divisions of this, which are: near-IR ($\sim 1-3\,\mu$m); mid-IR ($\sim 3-30\,\mu$m); far-IR ($\sim 30-200\,\mu$m); and sub-mm ($\sim 200-1000\,\mu$m). The boundaries of these ranges tend to vary in the literature.

2.1.1 From the Earth

The earth as a warm body emits in the infrared. This emission, as well as incoming emission from astronomical sources, is attenuated by atmospheric absorption – primarily due to water vapour, which then re-emits this radiation further into the infrared. In Fig. *2.1.1* the effects of this absorption are shown as a function of altitude. Any ground-based observations are therefore fully dominated by sky noise. In fact in the far-IR such observations are not possible at all. For mid-IR and sub-mm ground-based observations, filters are typically placed inbetween water vapour absorption bands, which define atmospheric 'windows'.

Outside the Earth's atmosphere, the Earth still causes problems for infrared observing, since radiation from its surface and atmosphere (both reflected solar and its own thermal emission) heats up the ambient space around making cooling the instruments harder, as well as restricting large fractions of the sky for observing due to the Earth's glow. This is overcome via highly elliptical Earth orbits (e.g. *ISO*), or by moving far from the Earth altogether (e.g. *Spitzer*s earth-trailing heliocentric orbit or the upcoming JWST at the Earth-Sun L2 position).

2.1.2 From the Solar System

The emission of the Solar System is commonly called the Zodiacal light since it is obviously concentrated at the zodiacal plane. In comes from interplanetary dust and various small bodies via two principle processes: scattered light from the Sun whose emission peaks in the visible, but whose Rayleigh-Jeans tail extends to the near-IR; and re-emission into the infrared of absorbed solar light. A minimum is created at $\sim 3\,\mu$m, which is therefore a well known favourable location for a near-IR filter (it is the classic L-band). For observations outside the Earth's atmosphere, it is the dominant background for mid-IR observations (and beyond depending on location).

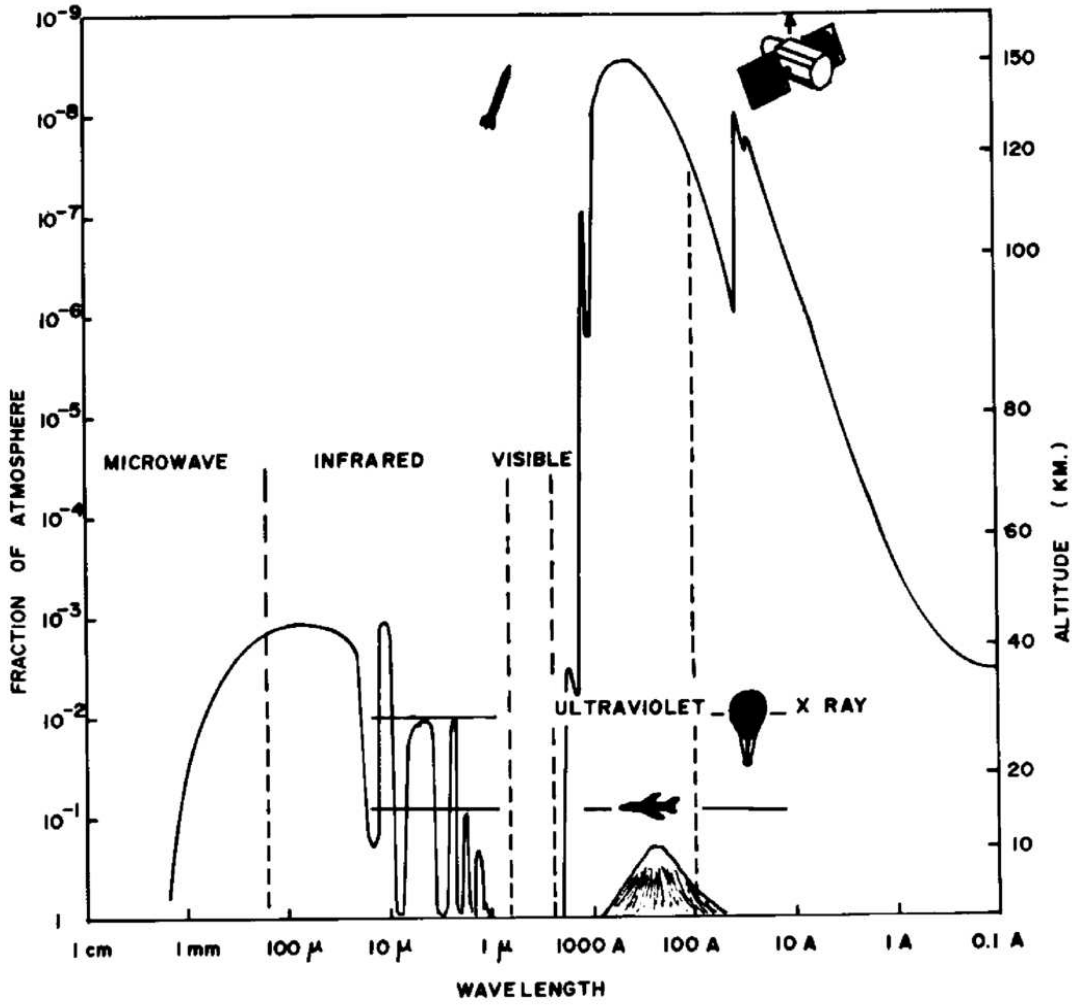

Fig. 2.1: A sketch of the atmospheric transmission with wavelength and altitude. The curve corresponds to half the incident radiation being transmitted. Note that in the definition we adopt here, the infrared regime extends to 1 mm. This figure was reproduced from: *http* : *//spacescience.nrl.navy.mil/introspaceastron.html*.

2.1.3 From the Milky Way

The Milky Way emission is in principle similar to that of the Solar System and consists of direct and dust-reprocessed stellar light. This emission is most prominent along the plane of the Milky Way, but can extend significantly beyond it due to high latitude clouds and small satellites (obviously there it is always there to some extend since we are inside the Galaxy). Fig. *2.1.3* shows this emission derived form the *IRAS* all-sky map where the Zodiacal light has been subtracted. The locations of extragalactic fields for infrared surveys tend to be chosen as regions of low Galactic emission ($\lesssim 1$ MJy/ster), as shown in Fig. *2.1.3*.

Note that, in terms of absolute power, these foregrounds are all stronger than the signal sought after. The dominant noise source of any infrared observing is always external to the instrument (which is typically cooled): for ground-based observing it is due to atmospheric emission, while for space-based observation it is the background emission (Solar System and Milky Way). However, in the far-IR regime the typically poor resolution of the instruments means that the dominant noise is due to confusion (i.e. in resolving multiple faint extragalactic source in the beam). Overcoming these backgrounds is particular problematic when looking for a diffuse signal, such as when determining the CIB spectrum [69]– see Fig. *2.2*. In this case, advantage is taken of the difference in distribution on the sky between the background and foreground contributors, such as looking for isotropic signals rather than those preferrentially distributed in the Solar System or Milky Way planes. The actual subtraction of the undesired foreground (such as in Fig. *2.1.3*), however is model-dependent [69]. Fig. *2.2* shows a summary of these sources of emission and their relative strengths and spectral shape.

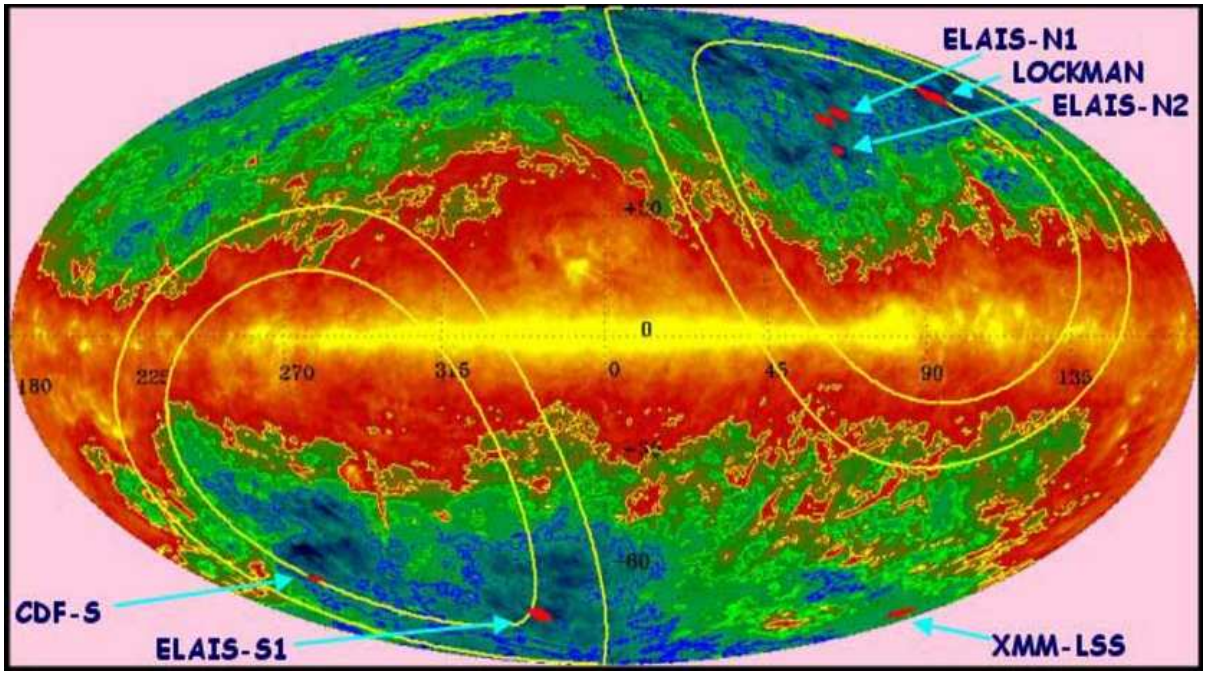

Fig. 2.2: This is the *IRAS* 100 μm sky in galactic coordinates (equal area projection). The contours in blue, green, and yellow show $1, 2,$ and $4\,\mathrm{MJy\,ster^{-1}}$ levels of the Galactic foreground, respectively. Several popular extragalactic fields are shown (those targetted by the SWIRE survey). The yellow ellipses show 30°, and 40° ecliptic latitudes. This figure is reproduced from the SWIRE website: *http* : *//swire.ipac.caltech.edu/swire/astronomers/strategies.html*.

2.2 Infrared Telescopes

This thesis is carried out primarily using archival data covering the full $\sim$1–1000 μm wavelength range. The specific samples used are outlined in detail in their appropriate chapter. Here we briefly describe the infrared facilities which provide the principal data for this thesis. The first three are presented in chronologically in order to allow for a brief historical overview of infrared instrumentation as well.

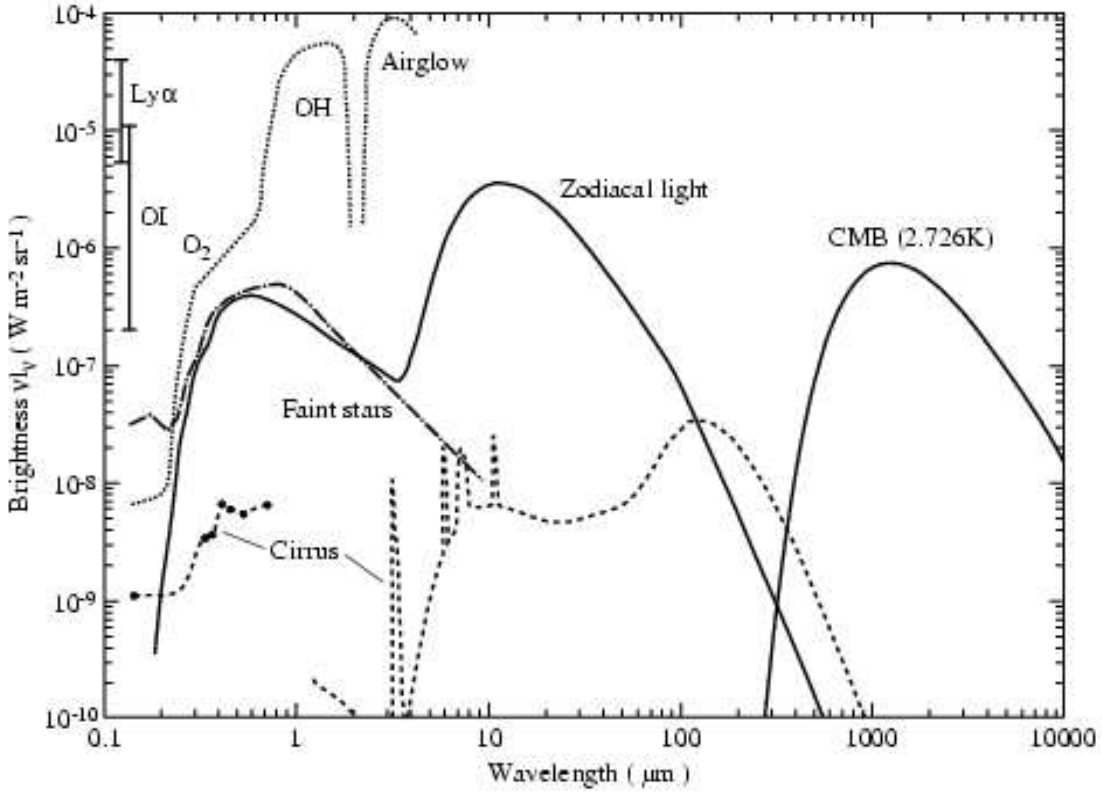

Fig. 2.3: The night sky brightness outside the lower atmosphere decomposed into its primary contributors as discussed in the text (see [104] for further details and full references).

2.2.1 The Infrared Astronomical Satellite

The Infrared Astronomical Satellite (*IRAS*) was the first major infrared mission [119]. It was an orbital mission designed for a single survey that would map the entire infrared sky. *IRAS* was a 60 cm Ritchey-Chrétien telescope with a 0.5 deg FOV. It surveyed the sky with a 65-detector array operating at $2-5$ K. It observed in four bands: $12\,\mu$m, $25\,\mu$m, $60\,\mu$m, and $100\,\mu$m. It operated for 10 months in 1983 and detected $\sim$20,000 galaxies most of which had not been detected previously at any wavelength [152]. Its all-sky map is still the standard for estimating the diffuse background from the Milky Way's ISM (see [153] and references therein).

2.2.2 The Infrared Space Observatory

The Infrared Space Observatory *ISO* was a 60 cm Ritchey-Chrétien observatory consisting of four science instruments operating between 2.5 μm and 240 μm [90]. The *ISO* mission ran between 1995 and 1998 and was designed primarily for targetted observations including individual local sources and mapping of up to few deg^2 fields. Its point-source sensitivity was about 1000 times that of *IRAS*. Cooling was achieved with 2000 litres of superfluid helium at 1.8 K, which eventually ran out.

2.2.2.1 Instruments

ISO had four science instruments: the *ISO* camera (ISOCAM; [18]), the *ISO* photo-polarimeter (ISOPHOT or PHT; [105]), the short wavelength spectrometer (SWS), and the long wavelength spectrometer (LWS). Here we use only ISOCAM and ISOPHOT data.

ISOCAM: This instrument observed between 2.5 and 17 μm and consisted of two arrays: SW and LW. SW was a 32×32 InSb array with 11 filters between 3 and 4 μm. LW was a 32×32 gallium-doped silicon array. It had ten filters, the most popular of which were: LW2 (6.7 μm) and LW3 (15.0 μm). The ISOCAM 15 μm data we use here were taken with the latter.

ISOPHOT: This instrument was designed to operate over a wide range of wavelengths (2.5 – 240 μm). It consisted of 3 parts: PHT-P, PHT-C, and PHT-S. PHT-P was a multi-band photometer using a variety of detectors covering $\sim 3 - 130$ μm, with a total of about 10 filters. PHT-C was specifically designed for far-IR observations and consisted of two arrays: 3×3 Ga:Ge for $60 - 100$ μm imaging and a 2×2 stressed Ge array for $120 - 200$ μm imaging (the latter was used in particular for the FIRBACK survey, which we discuss in detail in Chapter 4). PHT-S consisted of 2 grating spectrophotometers (covering $2.5 - 4.9$ μm and $5.8 - 11.6$ μm, with

$\lambda/\Delta\lambda = 100-300$) with a $24'' \times 24''$ aperture (this instrument was used in obtaining the low-resolution spectra used in Chapter 3). For further details on the telescope and instruments, see the *ISO* handbook (*http://www.iso.vilspa.esa.es/users/handbook/*).

2.2.3 The *Spitzer* Space Telescope

The *Spitzer* Space Telescope is an 85 cm Ritchey-Chrétien infrared observatory in an earth-trailing orbit [176]. This orbit enables one to remove the Earth as a heat source, while the solar panels effectively shield it from solar heating, such that cryogens are only used up to absorb heat dissipated by the instrument operations, which leads to temperatures in the range 1.5 K to 5.5 K depending on the power dissipated by the specific instrument. This means that only 360 litres of coolant are needed for a projected lifetime of $3-5$ yrs (compared with *ISO*'s about 2000 litres over 3 years). *Spitzer* was launched in August 2003, and has been performing science operations since December 2003. Most of its first year of observations was devoted to large 'legacy' programs (*http://ssc.spitzer.caltech.edu/legacy/*).

2.2.3.1 Instruments

Spitzer has three primary science instruments: the Infrared Array Camera (IRAC) [51], the Infrared Spectrograph (IRS) [77], and the Multiband Imaging Photometer for *Spitzer* (MIPS) [142]. Here we use only IRAC and MIPS data.

IRAC: This instrument has filters centered at 3.6 μm, 4.5 μm, 5.8 μm, and 8.0 μm. It consists of two adjacent $5.2' \times 5.2'$ fields-of-view (FOV) each of which is imaged simultaneously in two channels (3.6/5.8 or 4.5/8.0) by using dichroic beam-splitters. While observing, IRAC alternatively centres the target on each pair of arrays. Thus, for each channel, equal time is spent on blank sky as on target. The pixel size of all four arrays is $\sim 1.2''$, while the mean FWHM of the

beam in the four channels are 1.66″, 1.72″, 1.82″ and 1.98″. The 3.6 μm filter is located at the zodiacal emission minimum in order to facilitate the detection of faint extragalactic sources. In addition, by $z \sim 2$, it directly samples the peak of the stellar emission, making it an excellent tool for measuring the evolution of stellar mass (see Chapter 4 for a discussion on stellar mass derivation). The 8 μm filter is optimized for directly measuring the PAH emission of relatively nearby sources (up to $z \sim 0.5$). Fig. *1.1* shows the IRAC filters compared with typical galaxy SEDs.

MIPS: This instrument observes in three bands – 24 μm, 70 μm, and 160 μm. Unlike IRAC, however, it only observes in one band at a time. The 24 μm array has a $5' \times 5'$ FOV, and 2.6″ pixel size (6″ FWHM beam). The 70 μm array was been designed with a $5' \times 5'$ FOV. Unfortunately, soon after launch it was discovered that half of the 70 μm array is unusable, resulting in a $2.5' \times 5'$ FOV. To compensate, either sensitivity or mapping speed need to be compromised. The data used here were taken with reduced sensitivity, which, combined with the severe image artifacts of the 70 μm array, resulted in a low detectability of our sources in this band (see Chapter 5). The pixel size at 70 μm is 10″ while the FWHM is 18″. The 160 μm array has $0.8' \times 5'$ FOV, 17″ pixel scale, and 40″ FWHM beam. See Fig. *1.1* for the location of the MIPS filters in relation to the SEDs of galaxies.

2.2.4 The James Clerk Maxwell Telescope

The James Clerk Maxwell Telescope (JCMT; *http://www.jach.hawaii.edu/JCMT/*) is a 15 m dish on Mauna Kea, Hawaii, (altitute ∼4000 m). It is well above most of the obscuring water vapour (scale height ∼ 2000 m), which is the primary source of atmospheric opacity in the sub-

mm. This leaves windows of transmission at certain sub-mm wavelengths (including roughly at 350 μm, 450 μm, 750 μm, and with the best trasmission – 850 μm) making ground-based sub-mm astronomy possible. It has been in operation since the mid-1980s. The tripartite agreement that governs it (UK, Netherlands, and Canada) ends in 2009, but it is expected to be extended in light of the new suite of instruments to come over the next couple of years, particularly HARP-B and SCUBA2.

2.2.4.1 Instruments

The instruments on the JCMT today include capabilities for both continuum observing and spectroscopy. The current suite of instruments includes: the Sub-mm Common User Bolometer Array (SCUBA)[75] including a polarimeter, and four heterodyne receivers. We only use SCUBA data in this thesis, which we describe in more detail.

SCUBA: Currently still the foremost sub-millimetre camera, SCUBA has filters designed for the above mentioned atmospheric transmission windows at around 350 μm, 450 μm, 750 μm, and 850 μm. The instrument consists of a 37-bolometer long-wavelength (typically 850 μm) array, and a 91-bolometer short-wavelength (typically 450 μm) array, which operate simultaneously by means of a dichroic beam-splitter. The detectors are cooled to below 100 mK to maximize sensitivity (without such cooling, thermal emission from the instrument itself would overwhelm the signal). The SCUBA long-wave beam FWHM is $\sim 15''$ whereas the short-wave beam is $\sim 8''$. Despite the altitute, the atmospheric signal is not only still the dominant source of noise, but is in fact much stronger than any astronomical signal of interest [2]. This atmospheric emission is removed by chopping with the secondary mirror at a frequency of 7.8 Hz. This is faster than most sky variability, and thus correlated sky noise is removed.

In addition, nodding is performed every $10-20$ seconds to take out more slowly varying sky gradients, as well as a huge telescope emission signal. This involves starting from the ON position (usually with the central bolometer on the source), placing the source onto the OFF position, and then reversing to the other side so that the final sequence is ON–OFF–OFF–ON. Each nod pair is combined by subtracting the signals at the two positions, giving a triple-beam (–0.5,+1.0,–0.5) pattern on the sky. Since this nodding is rather slow, the process still leaves us with a small, but non-zero mean in the non-source bolometers, as well as with some left over correlated sky noise. This is removed in the data reduction stage by moving an array average at each integration [83].

Overall, the photometric data used in this thesis includes 13 filters primarily from the instruments described above. Their profiles (either accurate or approximated by square functions of $\delta\lambda/\lambda = 1/3$) as a function of wavelength are shown in Fig. *2.2.4*.1. Note that we cover the range of interest fairly uniformly with these.

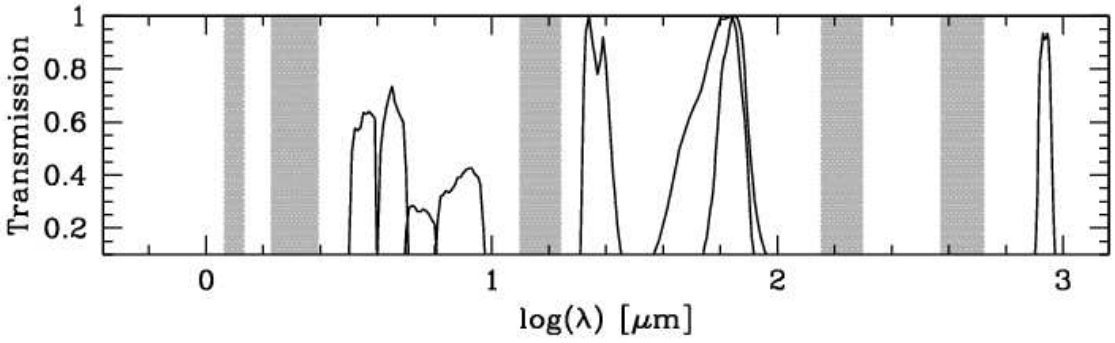

Fig. 2.4: The filter set used in this thesis. Note that we use $d\lambda/\lambda = 0.16$ for the $\mathcal{J}$-filter, $d\lambda/\lambda = 0.23$ for the $\mathcal{K}$-filter and $d\lambda/\lambda = 1/3$ for all other generic square filters.

2.3 Surveys

In Chapter 1, we discussed the main SED features of galaxies. As each part of the SED is sensitive to somewhat different physical properties of the sources, and moreover redshift effects move these in and out of our filters. A multi-wavelength approach is therefore crucial to study the properties of our sources, as well as to constrain galaxy evolution models (as discussed in Chapter 4 and Chapter 5). In Fig. *2.1.3* we shows that the selection of fields for deep extragalactic surveys is driven by the need for low background emission. Moreover, the need for multi-wavelength coverage means that current and upcoming surveys are likely to overlap with earlier ones, such that the handful of favourite fields presently have (or are planned to have) >10 photometric points in the infrared alone, usually suplemented with several optical bands, plus radio and X-ray. There are two basic designs features for such survey (and depending on the coverage there is some overlap among the multi-wavelength data). These are: going for the greatest sky coverage possible (wide); and going for the greatest sensitivity possible (deep). The wide surveys are typically those with 1 or more square degree fields. They have the advantage of detecting large numbers of different types of galaxy up to moderate redshifts, providing good statistics for exploring their properties, while also being sensitive to much rarer populations (including very luminous ones at high-z). Their large solid angles are also necessary if one is interested in clustering properties, or large-scale structure in general. Lastly, it is somewhat easier to assemble multi-wavelength data for such surveys, since large but relatively shallow optical, near-IR and radio maps cover much of the sky already (X-rays are more problematic however). Deep surveys are typically less than 1 square degree (or much smaller). They are necessary to study the properties of high-z sources which are very faint but are seen in comparable numbers to the more local populations of the wide surveys (i.e. we are roughly

sampling the same volumes). Multi-wavelength coverage is harder here since, for example, the best possible sensitivity of some instrument may never detect more than a tiny fraction of the sources detected by another instrument at its best sensitivity. Thus even if nominally the multi-wavelength data exist they are not usually sensitive to the same populations. For example the *Hubble* deep survey of the original HDF field detected hundreds of galaxies [177], while SCUBAs deepest current image of the same found only a couple [79]. Ideally one would like to have both area and sensitivity, but this is not feasible with the current technology and therefore one must compromise.

To put this work in context with other studies in extragalactic infrared astronomy, we need to compare our data with other past, current, or future surveys. In Fig. *2.3*, we plot a representative selection of such surveys. The symbol sizes are a guide to the areal coverage of the survey, ranging from deep, to medium and wide. Note that the worsening sensitivity with increasing wavelength is primarily due to the predominance of confusion noise. In Chapter 4, we will be discussing in greater detail the FIRBACK survey [37] which is marked here as the *ISO* 170 μm point. There, we will use archival data from the SWIRE survey [110], which is the widest-area of the *Spitzer* legacy surveys and is marked here with the larger magenta points. The small magenta points are for the *Spitzer* portion of the GOODS survey [35]. Note that BLAST [34], *Herschel* [67], *Planck* [168], and *ASTRO-F* [117] are all future missions and therefore for them these are only sensitivity estimates for surveys which are being planned.

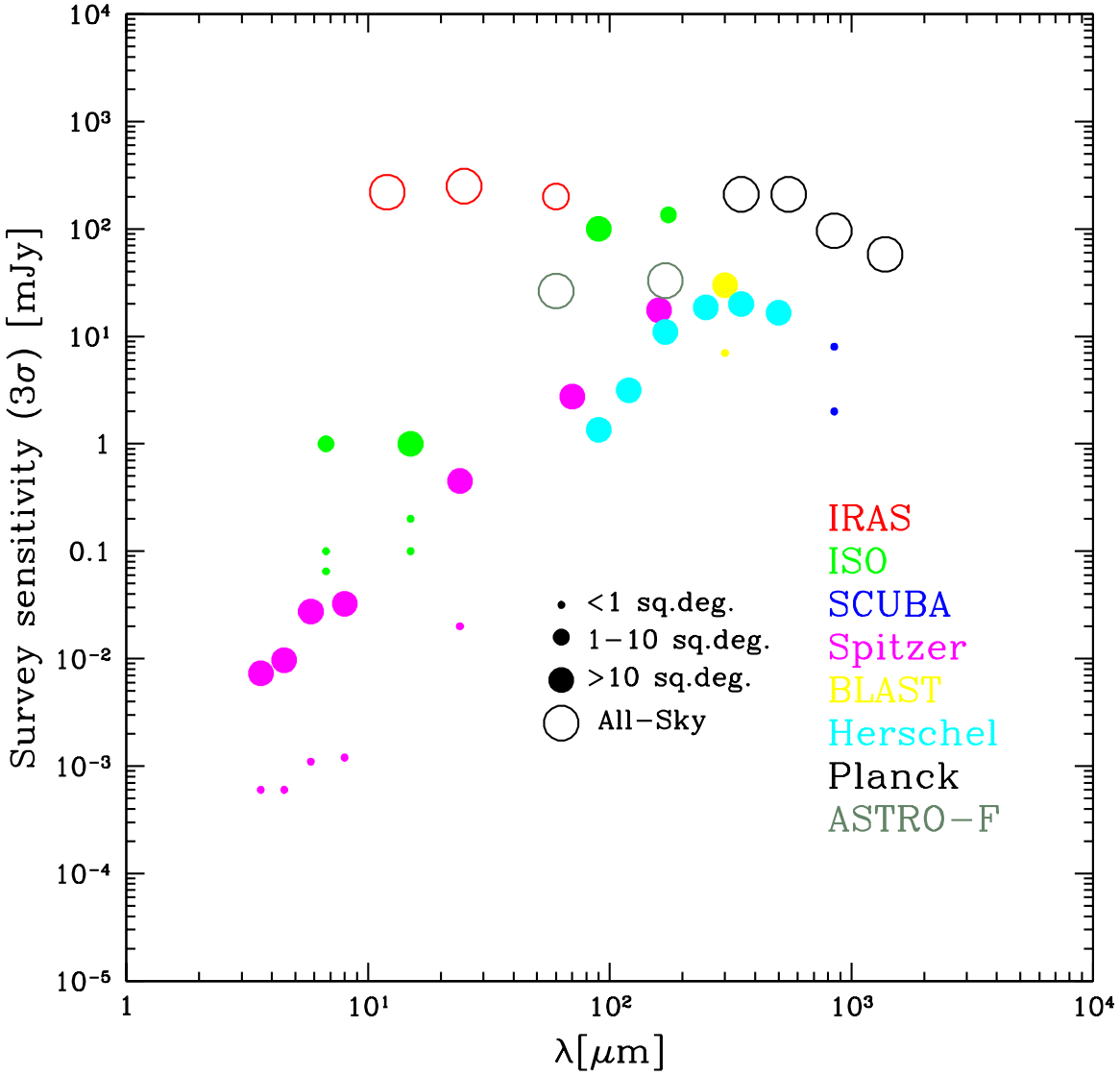

Fig. 2.5: A comparison of the sensitivities achieved by various past and future infrared surveys. Most of the data for this plot is from Chris Pearson's compilation (*http://astro.ic.ac.uk/ cpp/missions/*; see also [124]). The size of the symbols is indicative of the area of the survey divided into wide, medium, and deep as shown. Note that for BLAST, *Herschel*, *Planck*, and *ASTRO-F* the data shown are from simulations of future surveys.

CHAPTER 3

SIMULATING THE *SPITZER* MID-IR COLOUR-COLOUR DIAGRAMS

In Chapter 1, we outlined the main features of the mid-IR spectra of galaxies, including stellar, non-thermal dust, and molecular emission and absorption. At first glance, a large number of parameters is necessary to fit this; however, the data are not typically available to constrain fully such a model. Here we address the more realistic question: given this complex spectrum, how much can *Spitzer* broadband photometry alone tell us about the nature of the sources, especially if the redshift is also unknown? And how can one interpret the IRAC colour-colour diagram (specifically $S_{5.8}/S_{3.6}$ vs. $S_{8.0}/S_{4.5}$), as well as related diagrams including the MIPS 24 μm band?

Our first goal is to search for a common empirical description of the 1–12 μm spectral energy distributions (SEDs) of galaxies, focusing only on what drives the basic shape rather than the detailed structure. Our second goal is to generalize this description, via Monte Carlo simulations, to predict the loci of different types of source as a function of redshift ($z \sim 0-2$) in the IRAC and IRAC+MIPS colour-colour diagrams.

3.1 The sample

In order to study how a wide range of galaxy types map onto *Spitzer* photometry bands, we need to use a local sample for which the mid-IR SEDs are determined with sufficiently high

spectral resolution and signal-to-noise ratio (SNR).

We use a sample of 60 local galaxies, including ellipticals, normal spirals, ultraluminous infrared galaxies (ULIGs), starbursts, Seyfert galaxies, and HII galaxies (see Table *3.1*). This sample is in no sense complete or free of selection bias (the most obvious of which is toward more active galaxies), our approach being merely to cover as wide a range of spectra as possible. The limiting factor was the availability of 2–12 μm spectroscopy, especially for classes of galaxy whose volume density in the local Universe is low. We use spectra taken with the PHT-S spectrophotometer on *ISO* (see Chapter 2), which has a $24''\times24''$ aperture. For comparison, *IRAS* has FWHM beam from about $30''$ at 12 μm to about $120''$ at 100 μm. The bulk of the spectra were previously published as part of a study of mid-IR spectra of normal galaxies [111], or AGN [24]. We only include in our sample sources detected in all 4 *IRAS* bands, which naturally restricts us to bright, and/or local galaxies ($\langle z\rangle$=0.009). The typical overall SNR is $\sim$200[1], however, some of our sources have significantly higher SNRs which is likely to bias the fitting procedure and certainly makes it difficult to interpret the best χ^2 achieved. To avoid this bias, we have reweighted the spectra with weights corresponding to a signal-to-noise of 200. The above spectra were extended into the near-IR (NIR) by extracting the flux from 2MASS images using an aperture equivalent to the PHT-S one in a manner similar to previous authors [111] approaches[2].

In 10–20% of the sample the last $\sim$0.4 μm of each half of the PHT-S spectra suffer from what appear to be calibration problems, thus for simplicity we ignore these sections in the subsequent

[1]As estimated by $\sum(x_i/\sigma_i^2)/\sqrt{\sum(1/\sigma_i^2)}$.

[2]The main difference being that we adopted the 2MASS flux calibration [25] without additional offsets. Where available, the images used were taken from the 2MASS Large Galaxy Atlas [82], and the rest from the 2MASS Extended Source Catalog.

analysis. All spectra have been k-corrected to redshift zero.

3.2 Model

As stated in the introduction, the major components governing the shape of the 1–12 μm SEDs of galaxies are: direct light from old stellar populations; a smooth continuum probably due to very small grains; and PAH emission features. Fig. *3.2* illustrates this idea. Our model effectively treats all other possible components as noise to the above three, which we now discuss in turn.

Stars: We assume a 10 Gyr old, Salpeter IMF, single stellar population (SSP) which is justifiable since we only consider the SED redward of 1 μm where it is dominated by K and M giants (see also Fig. **??**). At the redshift range we consider, we are likely dominated by evolved systems, and therefore assuming solar metallicity is reasonable. Lower-metallicities would lead to a less pronounced 1.6 μm bump and 2 μm break (for a discussion of how these appear to IRAC as a function of redshift see Simpson & Eisenhardt 1999). We consider the effect of including the dust shell emission of AGB stars in section *3.5.1*. We use the PEGASE2.0 code [52] to generate a spectral template with the above specifications.

Continuum: The continuum is given by a flux density $f_\nu \propto \nu^{-\alpha}$. Note that, a power-law is often used to describe the *entire* MIR spectrum, which is clearly a very poor approximation in most cases. For the majority of galaxies, it is likely that the origin of this component is the non-thermal emission of very small grains [33], although the Wien tail of a $\gtrsim 100$ K thermal component is also a possible contributor. In some extreme AGN-dominated sources, this continuum component can also be due to synchrotron emission, although dust tori are a more likely source of MIR emission in typical AGN [131].

Table 3.1: Basic data for our sample

Name	RA[J2000]	Dec[J2000]	Class[a]	z^b	$\log(S_{60}/S_{100})$
Arp220	15:34:57.28	23:30:11.3	LINER, HII, Sy2	0.01813	–0.03
CenA	13:25:27.50	–43:01:10.9	S0, Sy2	0.00183	–0.35
ESO317-G23	10:24:42.50	–39:18:21.1	SBa	0.00965	–0.28
IC860	13:15:03.53	24:37:07.9	Sa, HII	0.01116	–0.00
IC883	13:20:35.34	34:08:22.0	Im, HII, LINER	0.02335	–0.21
IC1459	22:57:10.46	–36:27:44.5	E3, LINER	0.00564	–0.36
IC4329a	13:49:19.15	–30:18:34.2	SA0+, Sy1.2	0.01605	0.09
IC4595	16:20:44.26	–70:08:35.2	Sc	0.01137	–0.42
M51	13:29:52.66	47:11:42.6	SAbc, HII, Sy2.5	0.00154	–0.63
M81	09:55:33.23	69:03:55.0	SAab, LINER, Sy1.8	0.00013	–0.67
M83	13:37:00.46	–29:51:55.7	SABc, HII, Sbrst	0.00172	–0.33
M87	12:30:49.51	12:23:28.6	E, NLRG Sy	0.00436	–0.02
Mrk231	12:56:14:18	56:52:25.3	SAc, Sy1	0.04217	0.02
Mrk331	23:51:26.24	20:35:08.2	S?, HII, Sy2	0.01848	–0.06
Mrk359	01:27:32.2	19:10:39.5	SB0a, Sy1.5	0.01739	–0.19
Mrk520	22:00:41.43	10:33:07.5	Sb, Sy1.9	0.02661	–0.21
Mrk817	14:36:22.08	58:47:39.0	SBc, Sy1.5	0.03145	–0.03
NGC0701	01:51:03.71	–09:42:10.2	SBc, Sbrst	0.00610	–0.34
NGC0863	02:14:33.54	–00:46:00.4	SAa, Sy1.2	0.02638	–0.48
NGC1022	02:38:32.47	–06:40:39.0	SBa, HII, Sbrst	0.00485	–0.13
NGC1056	02:42:48.34	28:34:26.8	Sa, HII, Sy	0.00515	–0.25
NGC1068	02:42:40.83	–00:00:47.0	SAb, Sy1, Sy2	0.00379	–0.10
NGC1097	02:46:19.06	–30:16:28.0	SBb, Sy1	0.00425	–0.28
NGC1125	02:51:39.51	–16:39:08.4	SAB, Sy2	0.03175	–0.07
NGC1222	03:08:56.81	–02:57:17.6	S0, HII	0.00818	–0.06
NGC1326	03:23:56.40	–36:27:49.6	SB0/a, LINER	0.00454	–0.25
NGC1377	03:36:39.01	–20:54:06.2	S0, HII	0.00598	0.10
NGC1385	03:37:28.22	–24:30:04.0	SBcd	0.00498	–0.33
NGC1546	04:14:36.60	–56:03:38.9	SA0+?	0.00426	–0.58
NGC1569	04:28:11.14	64:50:52.3	IBm, Sbrst, Sy1	0.00024	–0.02
NGC3227	10:23:30.60	19:51:55.2	SAB, Sy1.5	0.00386	–0.35
NGC3705	11:30:05.82	09:16:36.3	SABab, LINER, HII	0.00340	–0.46
NGC3783	11:39:01.78	–37:44:19.6	SBa, Sy1	0.00973	–0.18

Table 3.1: Basic data for our sample *continued*

Name	RA[J2000]	Dec[J2000]	Class[a]	z	$\log(S_{60}/S_{100})$
NGC3949	11:53:41.42	47:51:31.7	SAbc, HII	0.00267	–0.38
NGC4027	11:59:30.59	–19:15:48.1	SBdm	0.00557	–0.39
NGC4051	12:03:09.58	44:31:52.9	SABbc, Sy1.5	0.00234	–0.53
NGC4102	12:06:23.37	52:42:41.2	SABb?, HII, LINER	0.00282	–0.17
NGC4194	12:14:10.10	54:31:41.9	IBm, BCG, HII	0.00836	–0.08
NGC4253	12:18:26.43	29:48:46.0	SBa, Sy1.5	0.01293	–0.06
NGC4365	12:24:28.87	07:19:04.6	E3	0.00415	–1.17
NGC4374	12:25:03.09	12:53:10.5	E1, LERG, LINER	0.00354	–0.37
NGC4418	12:26:54.65	–00:52:40.5	SABa, Sy2	0.00727	0.09
NGC4490	12:30:36.88	41:38:23.4	SBd	0.00188	–0.25
NGC4507	12:35:36.67	–39:54:33.2	SABab, Sy2	0.01180	–0.10
NGC4569	12:36:49.78	13:09:46.2	SABab, LINER, Sy	0.00215	–0.50
NGC4593	12:39:39.35	–05:20:38.8	SBb, Sy1	0.00900	–0.29
NGC4691	12:48:13.47	–03:19:59.1	SB0/a, HII	0.00137	–0.15
NGC5253	13:39:55.75	–31:38:30.8	Im, HII, Sbrst	0.00135	–0.011
NGC5433	14:02:36.03	32:30:37.5	Sdm	0.01452	–0.25
NGC5548	14:17:59.48	25:08:12.1	SA0/a, Sy1.5	0.01717	–0.18
NGC5866	15:06:29.41	55:45:47.2	S0, HII/LINER	0.00224	–0.57
NGC5915	15:21:33.16	–13:05:32.5	SBab	0.00758	–0.17
NGC5962	15:36:31.70	16:36:31.8	SAc, HII	0.00653	–0.42
NGC6000	15:49:49.28	–29:23:13.1	SBbc, HII	0.00732	–0.17
NGC6753	19:11:23.29	–57:02:55.4	SAb	0.01042	–0.46
NGC7218	22:10:11.71	–16:39:35.7	SBc	0.00554	–0.34
NGC7418	22:56:35.90	–37:01:45.7	SABcd	0.00482	–0.54
NGC7469	23:03:15.58	08:52:25.9	SABa, Sy1.2	0.01632	–0.13
NGC7592	23:18:22.10	–04:24:59.8	LINER, Sy2	0.02444	–0.12

[a] The NASA Extragalactic Database (NED) morphological and spectroscopic classes.

[b] Spectroscopic redshifts from NED. Typical uncertainties are 0.00002.

PAH features: The PAH bands are modelled here as a set of Lorentz profiles[3] [13] at 3.3, 6.3, 7.7, 8.6 and 11.3 μm[4]. We assume that typically the gap between the 8.6 and 11.3 μm PAH features accounts fully for the 10 μm gap, without the need to invoke Si absorption as well [73]. For the most active galaxies, the usual 7.7 μm and 8.6 μm features could be replaced by a broad peak at $\sim$8 μm, which, as other such variations, is treated as 'noise' to the model. It has been suggested, that this broad feature may be merely continuum bracketed by water ice and Si absorption features [162]. However, the positions, shapes, and relative strengths of the PAH features can vary in different (particularly extreme) environments and obscuration levels. Thus the PAH-dominated nature of this $\sim$8 μm feature cannot be ruled out [126]. For simplicity, we assume all such features are due to PAH emission (although likely both effects play a role). In general we simply assume a single template for our study; detailed modeling of the PAH features is beyond the scope of this work, the template being merely a fiducial which does not lead to obvious 'features' in the residuals of the fits (i.e. it is some average of the PAH emission features for our sample).

The overall model can be expressed as: $F_\nu = a_1 \times F_1(\mathrm{stars}) + \mathrm{a}_2 \times \mathrm{F}_2(\mathrm{PAH}) + 10^{\mathrm{a}_3} \times \nu^{-\mathrm{a}_4}$, where the a's designate the free parameters, and the F's are spectral templates. The last two parameters are merely the y-intercept and slope of a line in $\log \nu$ vs. $\log F_\nu$ space.

[3] i.e. $f_\nu \propto \{\pi\sigma(1 + ((\nu - \nu_0)/\sigma)^2)\}^{-1}$

[4] Note that here we do not include some prominent features at longer wavelengths since the *ISO* spectra we use to constrain this model only extend to 11.6 μm. In Chapter 4, the PAH template used includes several more strong PAH features at 12 μm – 20 μm.

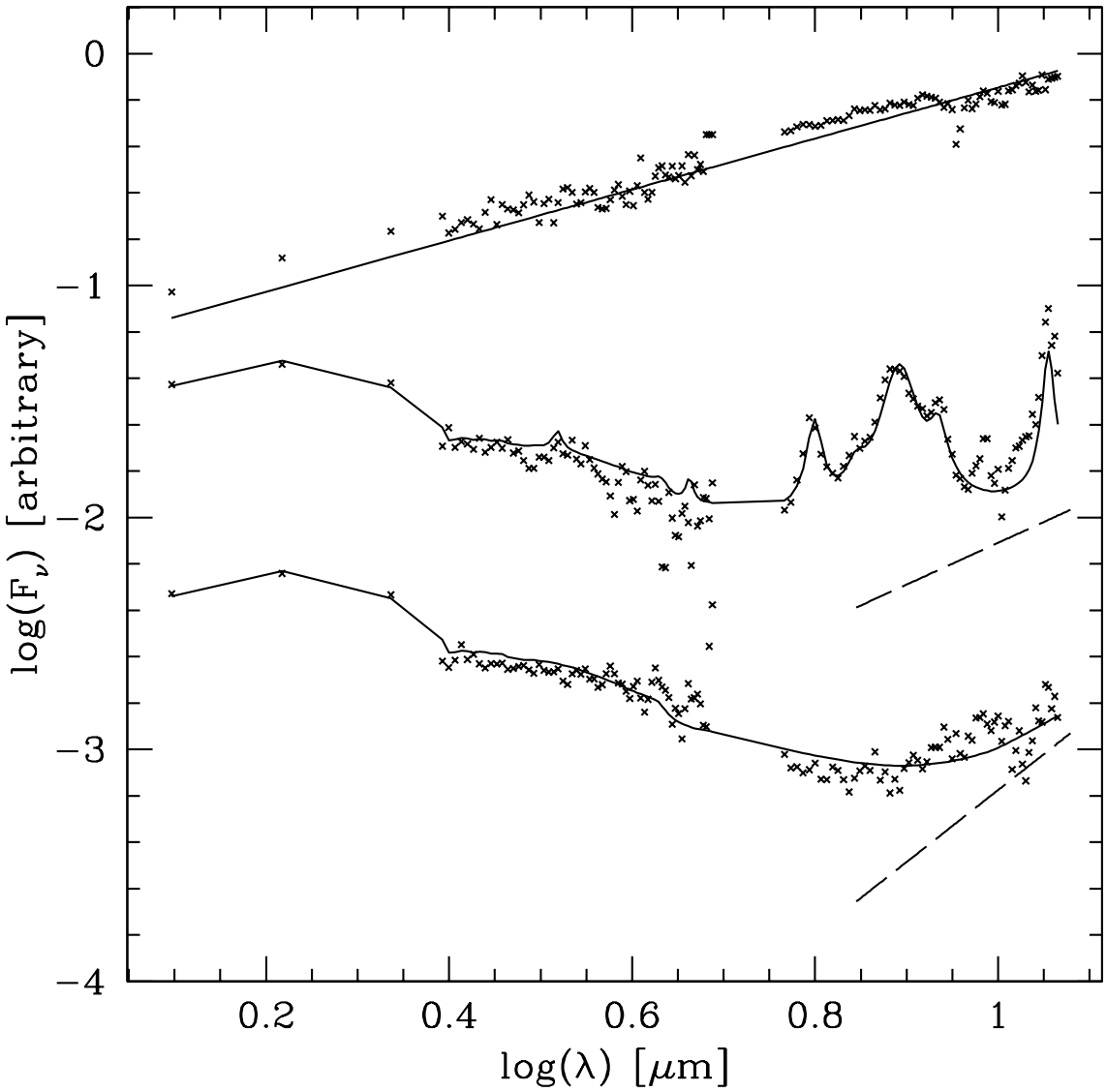

Fig. 3.1: Here we illustrate the idea behind our model, where the 'activity level' of the galaxies increases toward the top. First is NGC4374 overlaid with the 10 Gyrs old stellar population template plus a cool continuum ($\alpha \sim 3$). Next, M51 overlaid with the same as the above, only warmer continuum ($\alpha \sim 2$), and our PAH emission template. At the top is IC4329a which is essentially just a pure power law ($\alpha \sim 1$). Note that substructure in the spectra remains; however, the components which we model govern the bulk of the MIR colour variations.

3.3 Method

We use a Markov Chain Monte Carlo (MCMC) approach both to find the best-fit set of parameters for our data-set and to sample the posterior parameter distributions. MCMC is described in more detail in Appendix A. Here we outlines the steps relevant for this particular chapter, which differ slightly from the procedure used in the rest of this thesis. For a proposal distribution width of 1% of the total parameter range, a chain 'temperature' T=100 results in $>50\%$ initial acceptance rate, which constitutes good mixing. We use simulated annealing, i.e. gradually decrease T, to allow us to find the high-density regions more efficiently[5]. We run the Monte Carlo for 2000 iterations at each temperature, which meanwhile is decreased as $T_{i+1} = 0.9\,T_i$ for 20 steps[6]. There is no universal recipe for deciding when convergence (the 'burn-in') is achieved. However, by using a few test cases we find that although it is usually achieved fairly quickly it depends strongly on the initial conditions. We conservatively cut out the first three temperature steps (i.e. 6000 iterations), which guarantees us convergence in all cases. We then thin the chain by a factor of 30 to decrease the internal correlations which result from the above procedure [106]. The result of the MCMC analysis is a chain of parameters (for each of our 60 galaxy SEDs) which properly sample the distribution of best-fit model parameters.

[5]This approach is justified provided that the temperature is changed slowly enough in the late stages that it has negligible effect on the final likelihoods.

[6]These choices are not unique or optimal. We have merely chosen a set of MCMC parameters which work well for this particular case.

3.4 Results

3.4.1 **Individual fits**

Fig. *3.4.1* shows the spectra and fits for a sub-sample of our galaxies, along with the cross-correlation between the stellar and PAH amplitude parameters. Clearly the model provides a reasonable fit to the general shape of the SEDs, although, as expected, residual spectral substructure remains, largely due to variations in the PAH features. This is also seen in the mean of the reduced χ^2s obtained which is ~ 4.

For our purposes, we need to estimate how much noise to include in the *Spitzer* broadband fluxes in order to account for spectral substructure not included in the model, without including the uncertainties associated with the PHT-S spectra themselves. In Fig. 3.3, we show the histograms of the difference in IRAC fluxes obtained by convolving the residuals with the IRAC filter profiles as $\Delta F = \int \Delta S_\nu T_\nu d\nu / \int T_\nu d\nu$, where T_ν is the transmission curve for the given filter, and ΔS_ν is the residual spectrum. These distributions peak near zero, showing that our model accounts fairly well for the relevant spectral gradients. We estimate the scatter expected from the uncertainties in the data by taking their average under the filter profile (analogously to the flux estimates) and dividing by $\sqrt{N}$ (i.e. the error-in-mean). We compare this scatter with the one from the fits and find that the excess is accounted for by $\sigma_{3.6} = 10\,\mathrm{mJy}$, $\sigma_{4.5} = 8\,\mathrm{mJy}$, $\sigma_{5.8} = 18\,\mathrm{mJy}$, and $\sigma_{8.0} = 9\,\mathrm{mJy}$. We include these additional sources of uncertainty in the colour-colour plot simulations (section *3.5*).

3.4.2 **Correlations**

The Markov chains constructed above allow us to study how the parameters relate to each other. This is shown in Fig. *3.4.1* where, as expected, the general trend is for strong stellar

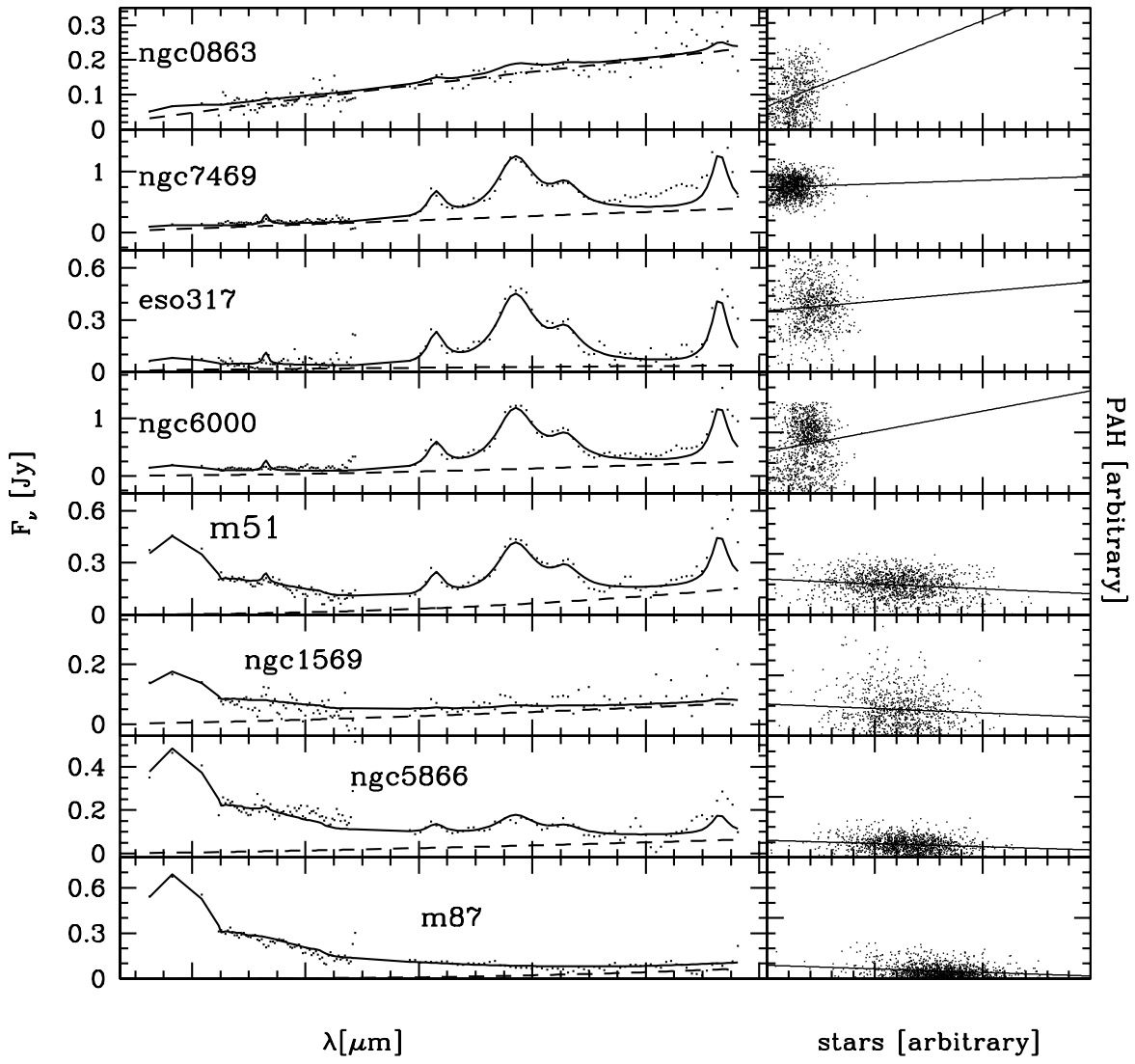

Fig. 3.2: A sub-sample of our galaxies used to illustrate the continuum in relative strength of PAH vs. stellar contributions. The solid line shows the best-fit model, while the dashed line shows the power-law component separately. The second column shows the accepted MCMC trials for the stars (x-axis) and PAH (y-axis) amplitude parameters (each is divided by $\Sigma\nu F_\nu$ for ease of comparison) for each galaxy, with the same scale used for all.

light emitters to be relatively weak PAH emitters, i.e. the error ellipses range from being elongated along the PAH-axis to being elongated along the stellar-axis, with the intermediate cases showing a negative correlation. The continuum component suffers from a degeneracy with the PAH emission strength especially for sources where both are significant. Fig. *3.4.2* shows the marginalized Markov Chain distributions of the continuum slope, α, for a representative sub-sample of six galaxies. In addition, the total distributions of the PAH-dominated, stellar-dominated, and continuum-dominated sources are shown, where the highest peak is respectively $\alpha \sim 1.8$, $\alpha \sim 1.6$, and $\alpha \sim 1.2$ for the three types. The last is roughly consistent with the $\alpha = 0.84 \pm 0.24$ obtained by Clavel et al. (2000) for Seyfert 1 galaxies. For the best-fit models for each of our sample galaxies, we look at how this parameterization relates to the *IRAS* colours. Fig. *3.5.1*a shows that the strength of the PAH emission is positively correlated with the S_{60}/S_{100} colour, as expected since the latter is a measure of the ISRF which excites the PAH molecules. The exceptions here are the star symbols, which represent starformation-dominated active galaxies such as Arp220, and the black circles, which are continuum-dominated AGN. The rest of the AGN sources here obey the general trend, due to PAH emission associated with starburst activity. This distinction is even clearer in Fig. *3.5.1*c, where the black circles are clearly strong continuum emitters (although not the only ones), while the star symbols are weaker than average continuum emitters (NGC4418 is off-scale here). In Fig. *3.5.1*d we show the well known *IRAS* colour-colour plot, where one should notice that as expected the 'stars' occupy the area typically explained by very active galaxies whose PAH carriers are being destroyed by the extreme ISRF, while the AGN sources obey the general trend. This shows that these colours are insufficient in themselves to distinguish AGN-dominated galaxies, as the lack of PAH emission is compensated by warmer dust resulting in similar S_{12}/S_{25} colours (IRAC

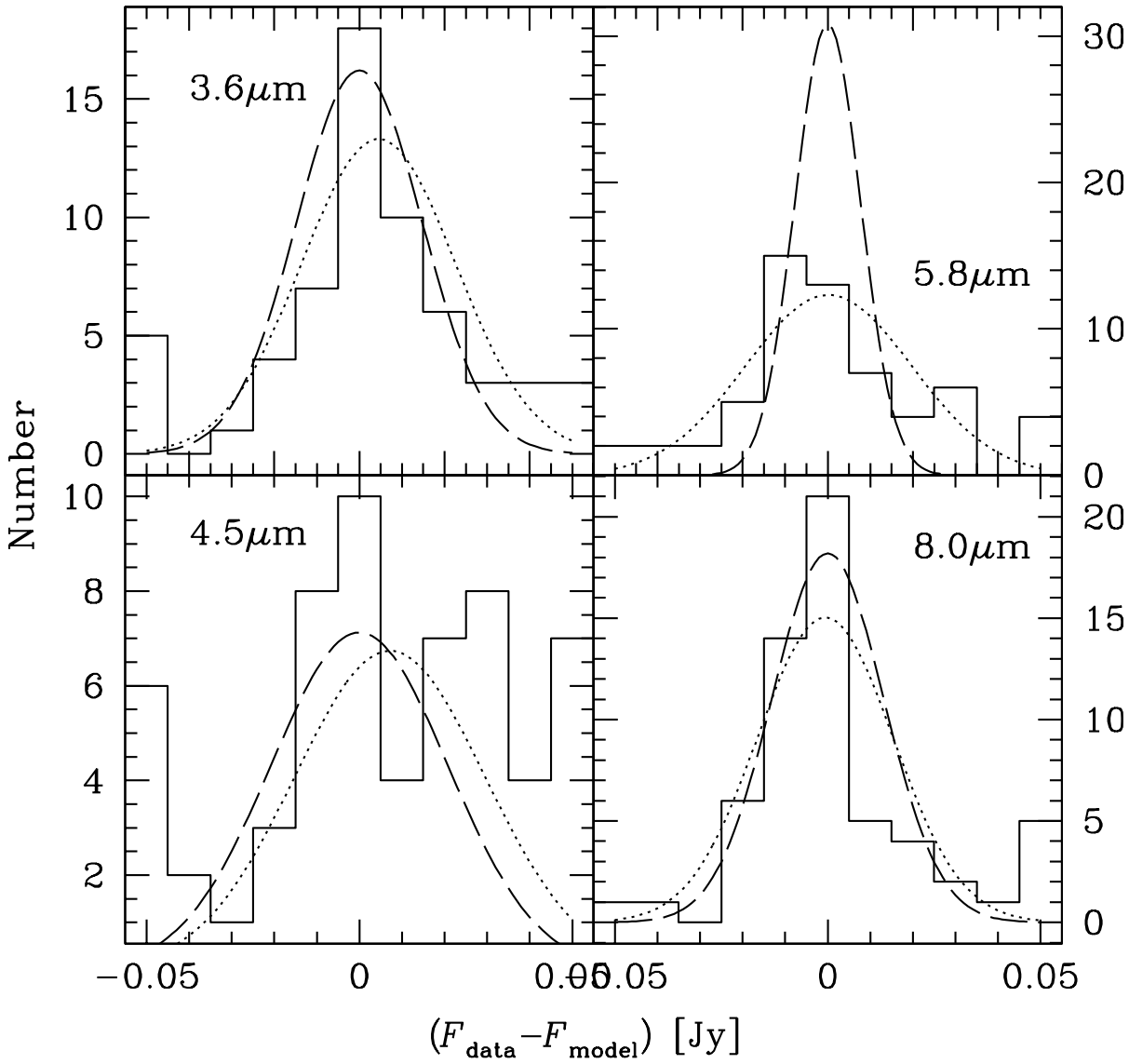

Fig. 3.3: Histograms of the IRAC fluxes obtained from the residuals. Here the dashed line indicates the scatter expected from the uncertainties in the data, while the dotted line is the Gaussian corresponding to the mean and σ of the histograms. The positive excess noticeable in the 4.5 μm plot can be due to the contribution of various strong lines which emit there (e.g. Br α, CO) although some residual poor calibration could also be the cause, as suggested by the presence of a negative excess as well. The quality of the data does not allow us to distinguish these explanations. The excess scatter in the four bands is: $\sigma_{3.6} \simeq 10$ mJy, $\sigma_{4.5} \simeq 8$ mJy, $\sigma_{5.8} \simeq 18$ mJy, and $\sigma_{8.0} \simeq 9$ mJy.

colours are far more efficient here, as discussed in section *3.6.1*). Excepting the six galaxies discussed above, the ratio of the PAH to stellar emission appears to be anti-correlated with the *IRAS* S_{12}/S_{25} colour (Fig. *3.5.1*c). This cannot be explained through PAH emission, since that would affect the $12\,\mu$m filter (which includes the $11.3\,\mu$m and $12.6\,\mu$m features), and thus, if this was the primary driver the correlation would be positive. It rather suggests that warm ($\sim 100\,$K) dust, which primarily affects the $25\,\mu$m channel, goes along with an increase in the PAH-to-stellar ratio. This makes sense since both PAH emission and warm dust are expected to trace relatively recent star formation [54], due to their preferentially being excited by energetic UV/optical photons, while the stellar component here is composed of older, redder stars.

3.5 IRAC colour-colour simulation

Since we have 60 independent spectra, then the overall probability of the data given the model is $P(\theta|\mathbf{D}, M) = \Pi_{i=1}^{60} P(\theta|\mathbf{D}_i, M)$, and we simply link the individual chains obtained above to form a master chain[7]. Our simulation uniformly draws 10,000 times from this chain, and is thus subject to the same selection effects as our original sample. Each set of parameters thus obtained defines an SED through the 4 parameter model, where we use $\lambda/\delta\lambda \sim 200$. To obtain the IRAC flux densities from these, we convolve the above with the IRAC filter profiles. To these flux densities we add Gaussian noise, of width equal to the rms for the residuals found in section *3.4.1*, in order to account for the missing substructure. Note that this scatter should be regarded as an upper limit, as the Markov chain already accounts for some of it and therefore

[7]This effectively assumes that our sample of 60 galaxies uniformly samples the full population of galaxies. However, it would be easy to change this assumption by varying the weights given to each of the galaxies in our sample.

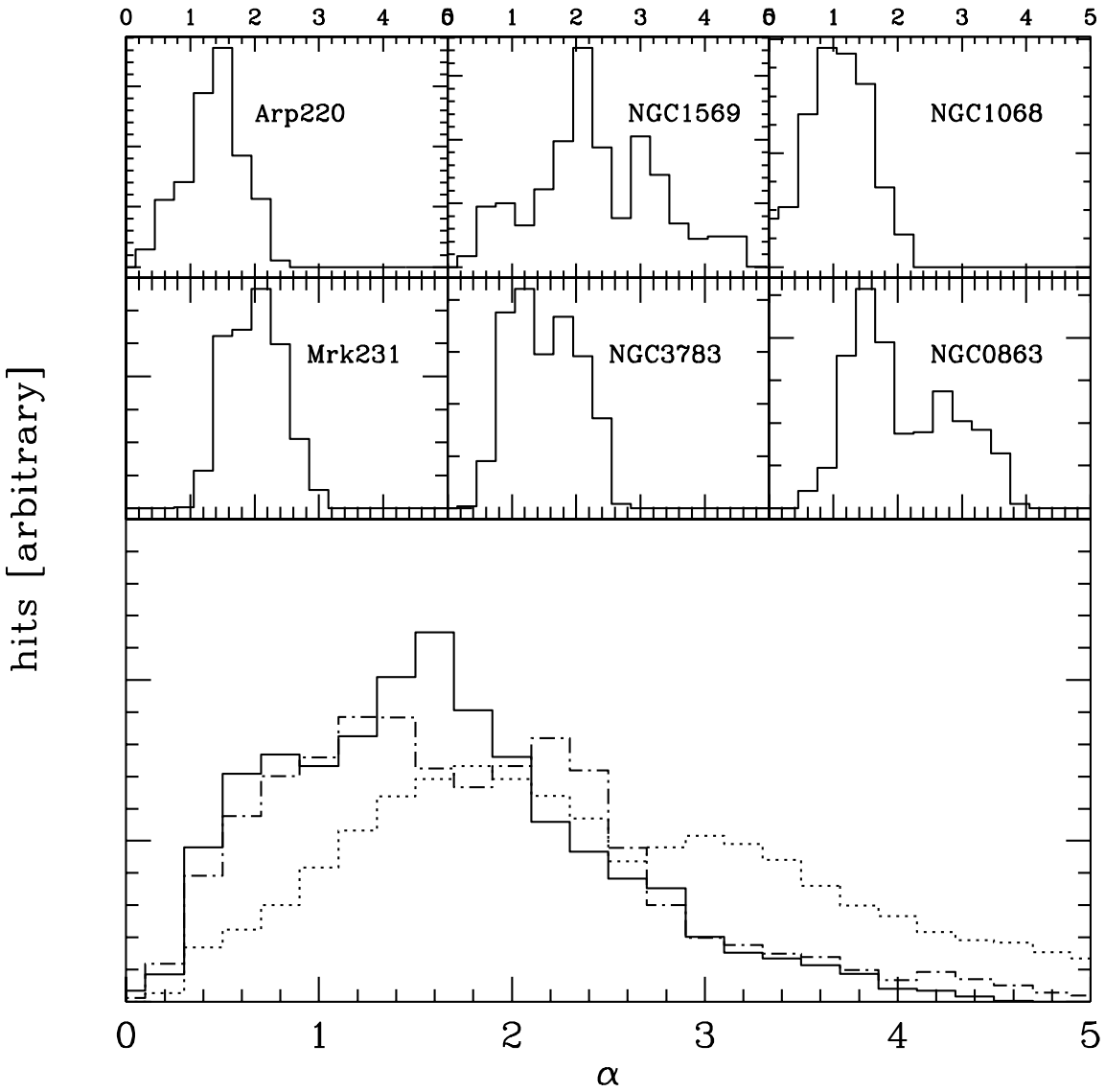

Fig. 3.4: The marginalized distributions of the continuum slope α. The top six panels show these for a representative sub-sample, while the bottom panel shows the total distribution for the three spectral types, where the solid line is the stellar-dominated sub-sample, the dotted line represents the PAH-dominated galaxies, and the dot-dashed line is the continuum-dominated distribution.

some fraction of the noise is effectively added twice. The resulting IRAC colour-colour diagram is shown in Fig. *3.5.2*. Here we distinguish stellar-dominated (*red*), PAH-dominated (*green*), and continuum-dominated (*blue*) sources.

The most prominent feature of this colour-colour plot is the PAH-to-stars sequence. Since (as discussed previously) this ratio is an indicator of the starformation activity of a galaxy, this is likely to prove a valuable diagnostic in the study of local sources such as resolved galaxies in the nearby Universe or even galactic starforming regions. Its exact shape is sensitive to the PAH feature profile and thus can itself be used as a diagnostic, for example to test if this sequence is significantly different in low metallicity environments than high metallicity ones. Such studies are feasible, because the photometric uncertainty of *Spitzer* observations is typically far smaller than the scatter considered here.

The second aspect of Fig. *3.5.2* is that continuum-dominated sources (AGN) themselves occupy a distinct region with redder $S_{5.8}/S_{3.6}$ colours for a corresponding $S_{8.0}/S_{4.5}$ colour than the previous described sequence. It is curious to note that practically every combination of our three components is found in nature although the vaguely triangular shape which one can imagine drawing on this plot is not occupied with equal density (possibly due to the selection bias of our particular sample). Continuum-dominated sources most commonly have little or no stellar emission. However, sources that are both strong PAH and strong continuum emitters are common.

3.5.1 Effect of AGB dust shells

Assessing the level of contribution of AGB dust shells to galaxy spectra is difficult because the effect has the same sense (in terms of the IRAC colours) as interstellar dust. To show this we

overplot solar metallicity[8] 100 Myr–10 Gyr SSP spectra of Piovan et al. [133] onto our $z = 0$ colour-colour plot (Fig. *3.5.2*). AGBs have a significant effect on the spectra only for relatively young stellar populations. Such populations presumably also emit strongly in their ISM dust (as assumed in our model), which starts to dominate the spectra at $\lambda > 4$ μm. Moreover, in spatially integrated galaxy spectra, the contribution of the young (e.g. starburst) population can be overpowered in the observed integrated spectra by an older surrounding population. In Fig. *3.5.3* we show the actual stellar population SEDs, including AGB dust shell emission and some of the available *ISO* spectra for comparison. We notice that, as expected, the difference is most easily assessed in the $\sim 3-5$ μm regime. AGB-dominated SEDs overpredict the power emitted at those wavelengths compared with the near-IR emission. This suggests that the mean age of the stars in the sampled aperture is greater than ~ 0.5 Gyr. In addition, some of our power-law component may be contributed to by AGB emission in the > 5 μm spectra (see for example the 300 Myr-old SSP spectra in Fig. *3.5.3*). For the study of integrated galaxy spectra this effect is not significant; however, it should be kept in mind both in looking at finer physical scales inside galaxies, where younger average ages may be observed, and also due to the possible foreground from Galactic AGB stars.

3.5.2 The use of 24 μm data at $z > 1$

Due to the lack of available data, we do not formally extend our model past 12 μm. However, because we want to consider the effects of redshift, we need to discuss the use of the 24 μm filter once our 1–12 μm spectra are redshifted into it at $z \gtrsim 1$. The *IRAS* 12 μm and 25 μm fluxes for our sample are used to define the colour space occupied by $z \sim 0 - 1$ sources, assuming there

[8] Metallicity has a much smaller effect than age here, since we are merely sensitive to the relative fraction of the SSP of stars in their AGB phase.

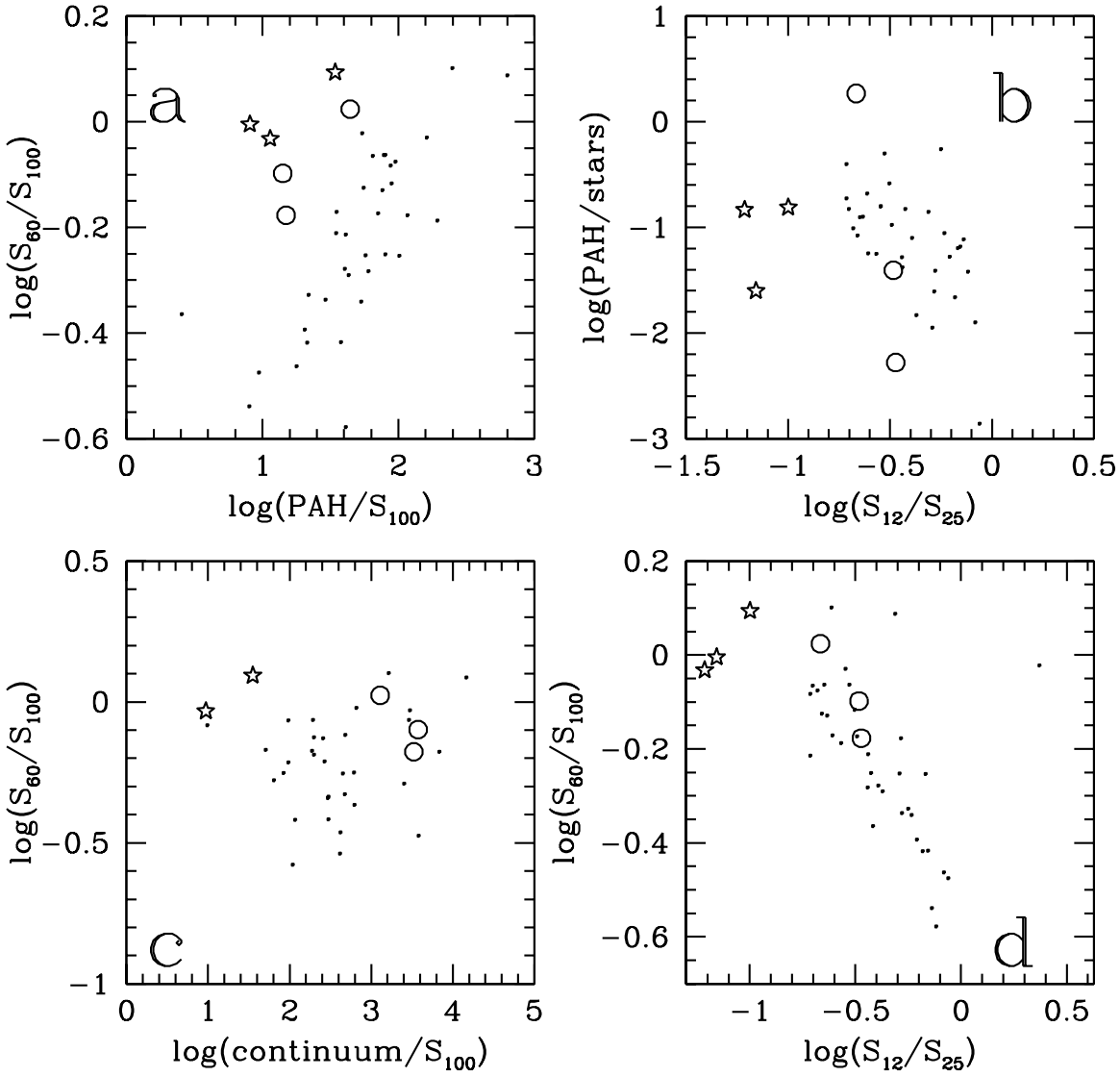

Fig. 3.5: PAH/continuum/stars mean the best-fit components integrated over the 3–12 μm range. To minimize aperture bias, only $z > 0.004$ galaxies are used. Star symbols mark three SF-dominated active galaxies, while circles show three AGN-dominated active galaxies.

are no significant spectral dips between the two (although the PAH influence on the 12 μm filter makes this slightly uncertain).

3.5.3 The effect of redshift

We show in Fig. *3.6.2* the $z = 0-2$ redshift evolution for models representative of the three basic types discussed in this work, as well as the spread from our models. In Fig. *3.5.4*, we show a different projection, where the redshift dependence of the colours considered here is explicitly shown for the three types. We can understand the general trends of movement in the colour-colour diagrams through considering the main PAH features moving through the IRAC bands.

For PAH-dominated sources, the $S_{5.8}/S_{3.6}$ colour shifts blueward between $z \sim 0-0.1$, due to the 6.2 μm feature leaving the 5.8 μm filter. By $z \sim 0.2$ the 3.3 μm feature leaves the 3.6 μm filter and thus the colour shifts slightly redward again, until the stellar 1.6 μm bump begins to enter the 3.6 μm filter past $z \sim 0.7$. The colour shifts redward strongly when the 5.8 μm filter begins to sample the stellar peak as well. On the other hand, the $S_{8.0}/S_{4.5}$ colour starts off red due to the powerful 7.7 μm PAH feature complex, and gradually turns bluer. This is due to the influence of the 3.3 μm feature on the 4.5 μm filter ($z \sim 0.2 - 0.5$), coupled with the 6.2 μm feature replacing the 7.7 μm one. Past $z \sim 0.5$ the strongest PAH features leave the 8 μm filter altogether, and at this point star-forming galaxies enter the general vicinity of $z \sim 0$ stellar-dominated sources, which is also where contamination from foreground stars (especially dust-enshrouded ones) is most severe. Thus, these two colours alone are insufficient to distinguish the high-z starforming galaxies.

Stellar-dominated sources occupy the same general vicinity until $z \sim 0.6$ when the 1.6 μm

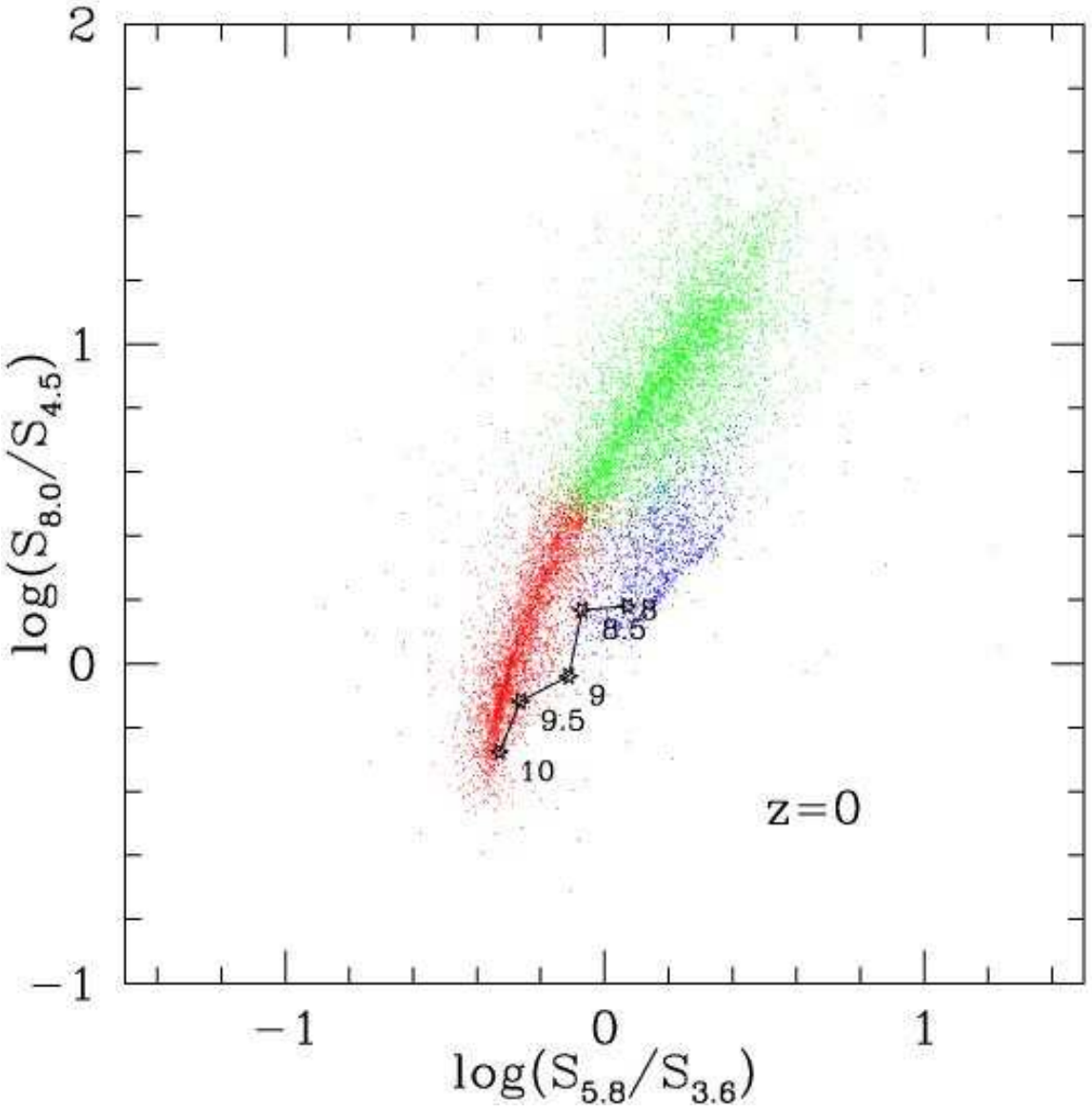

Fig. 3.6: Here we show the Monte Carlo generated IRAC colour-colour diagram, where red indicates starlight-dominated, green is PAH-dominated, and blue designates continuum-dominated. The tracks show the effect of AGB dust shells on the IRAC colours for a range of stellar population ages (given in log[Myr]).

bump enters the 3.6 μm filter, while further redshifting (especially past $z \sim 2$) causes a red $S_{5.8}/S_{3.6}$ colour due to their red optical continua. This leads to a sequence similar to the 'AGN-sequence' however offset in its $S_{8.0}/S_{4.5}$ colour.

Continuum-dominated sources, being relatively featureless, also do not leave the general vicinity they occupy locally, instead they just shift along the 'continuum-sequence' due to slight changes in slope. Only largely unobscured AGN will ever display 'blue' IRAC colours when the rest-frame optical wavelengths begin to be sampled at $z > 2$.

3.5.4 Colour selection

In summary of the previous sections, the three colours ($S_{5.8}/S_{3.6}$, $S_{8.0}/S_{4.5}$, and $S_{24.0}/S_{8.0}$) allow us to separate the three basic types of mid-IR spectra as a function of redshift over the range $z \sim 0-2$. Any combination of two of these colours leads to degeneracies between galaxy type and redshift, and thus these can only be used in combination with some additional constraint. The natural redshift bins one can consider arise from the redshifting of the PAH features and the 1.6 μm stellar peak[9], and these are: $z \sim 0-0.1$; $z \sim 0.1-0.5$; $z \sim 0.5-1.5$; $z \sim 1.5-2.0$. The evolution of these colours with redshift is illustrated in Fig. *3.5.4*.

3.6 Discussion

3.6.1 Comparison with early *Spitzer* results

The First Look Survey (FLS), conducted with the IRAC and MIPS instruments on the *Spitzer* Space Telescope, is a publicly available, shallow, 4 deg^2 survey[10]. The IRAC 4-band catalogue

[9] See also Le Floc'h et al. [103] for a discussion of photometric redshift estimation from the 1.6 μm peak redshifted into IRAC bands combined with MIPS 24 μm and optical photometry.

[10] http://ssc.spitzer.caltech.edu/fls/

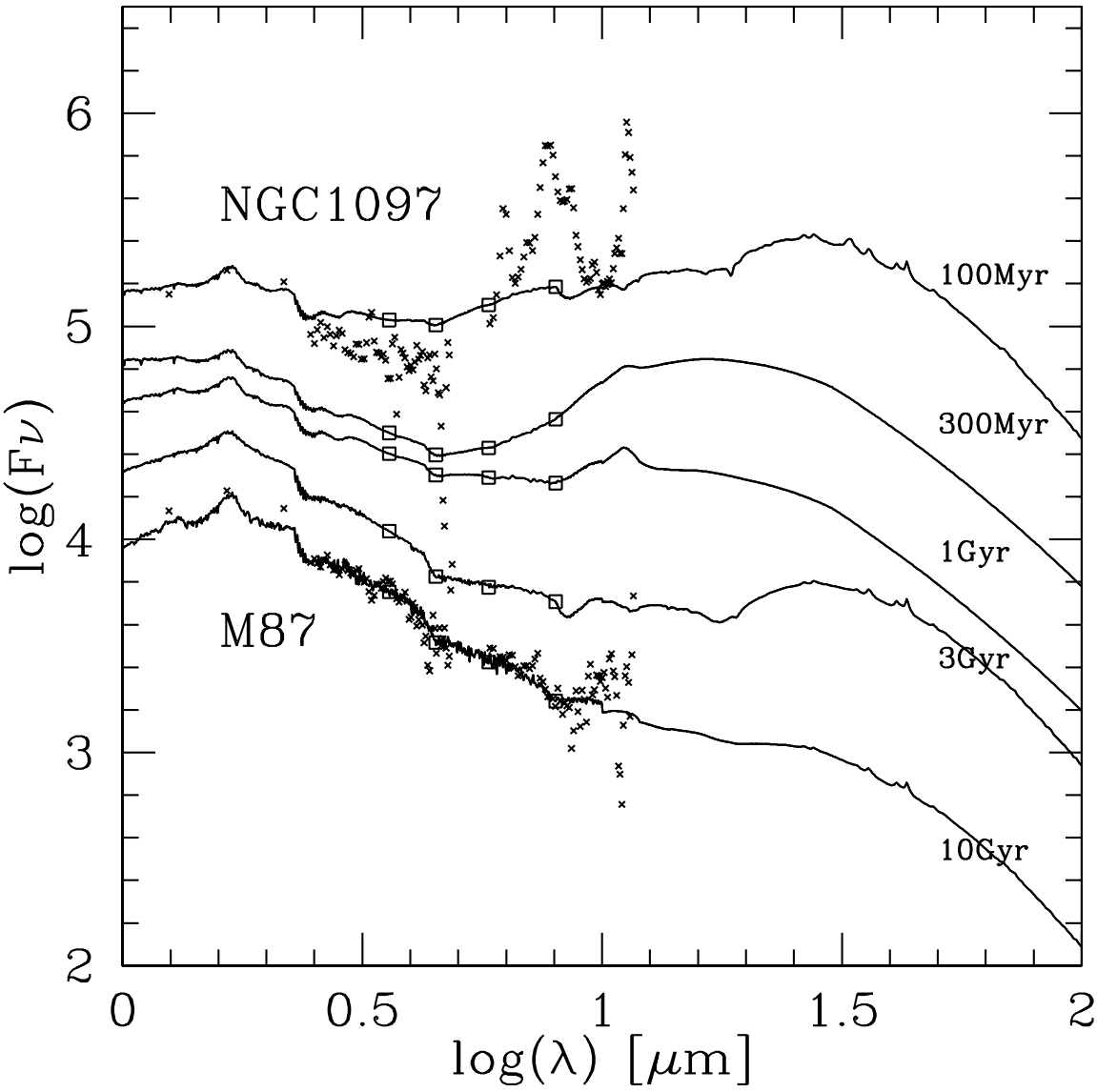

Fig. 3.7: Simple stellar population spectra [133] corresponding to the age track in Fig. *3.5.2* overlaid with representative galaxy spectra. See section *3.5.1* for discussion.

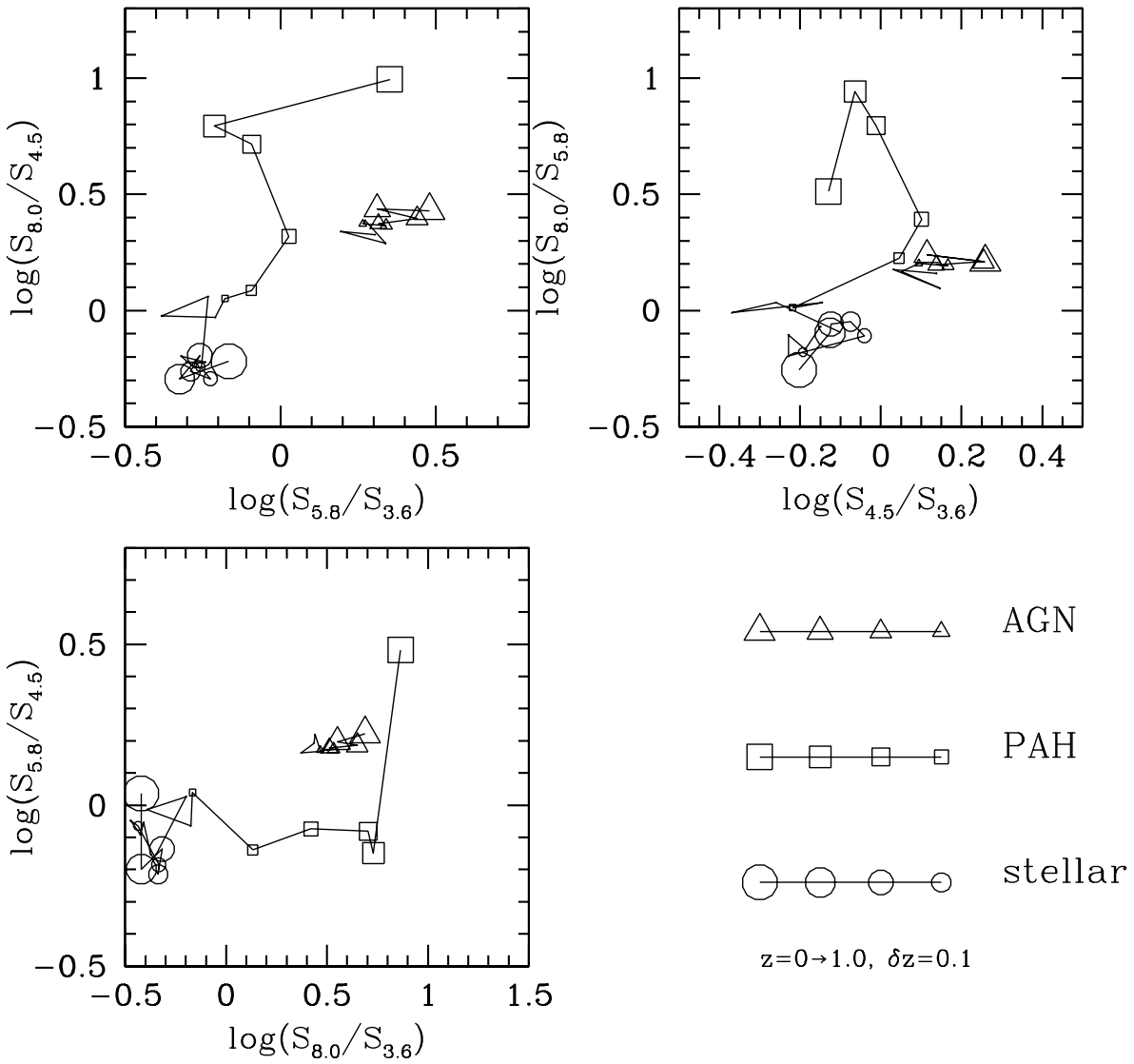

Fig. 3.8: The $z = 0 - 1$ redshift evolution of various colour projections of three model spectra representative of the three major types of mid-IR spectra: continuum-dominated; PAH-dominated; and stellar-dominated.

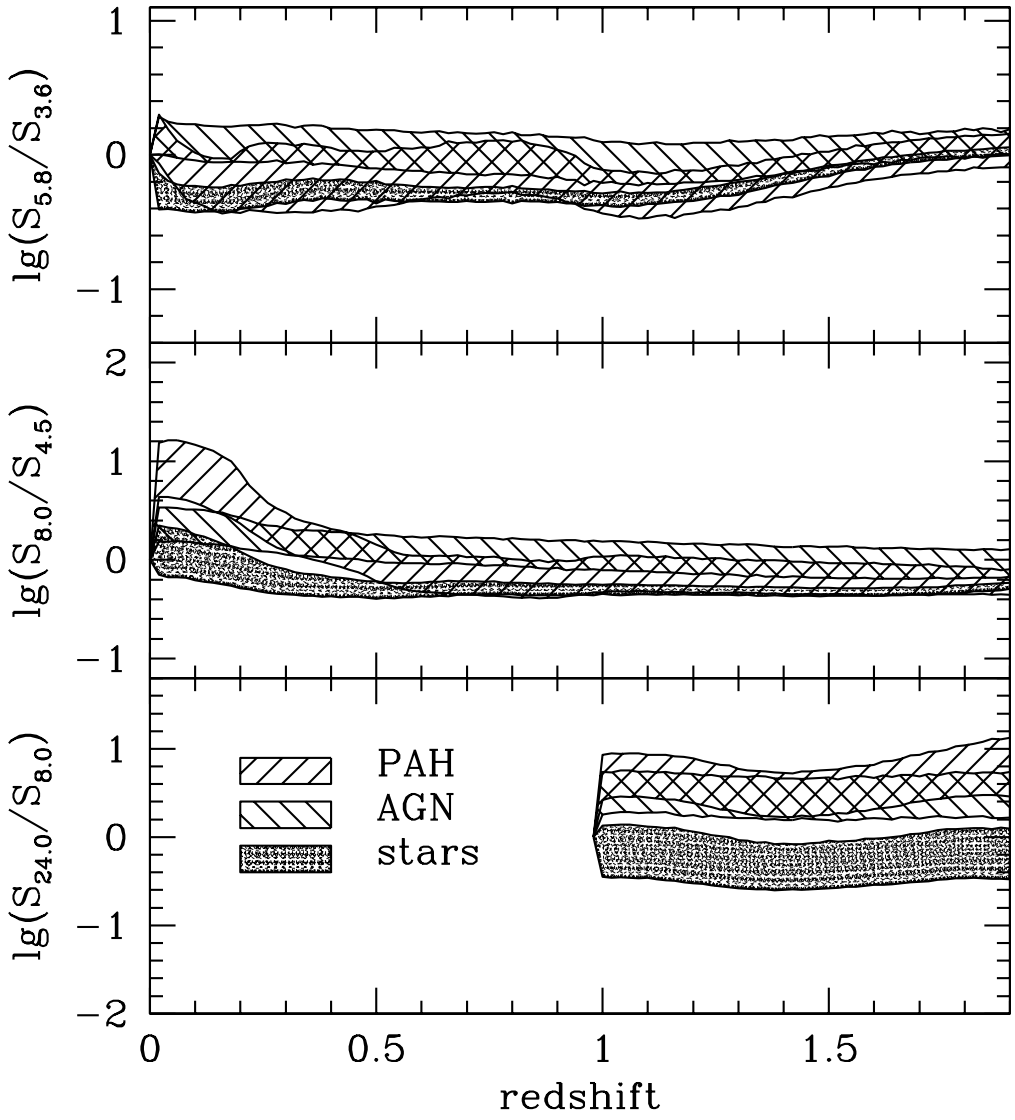

Fig. 3.9: The colour evolution of stellar-dominated, continuum-dominated, and PAH-dominated sources as a function of redshift. Note in particular the influence of the 7.7 μm PAH feature at $z \lesssim 0.5$, and the 1.6 μm peak at $z \gtrsim 1.3$. The scatter represents $\pm 2\,\sigma$. See section *3.5.3* for further details.

[97] has flux density limits ($5\,\sigma$ in a $5''$ aperture) of $\sigma_{3.6} \approx 7\,\mu$Jy, $\sigma_{4.5} \approx 8\,\mu$Jy, $\sigma_{5.8} \approx 60\,\mu$Jy, and $\sigma_{8.0} \approx 50\,\mu$Jy. We use this catalogue to explore qualitatively how our model compares with data. Fig. *3.6.2* shows the FLS data along with a simulation of it from our model. To create the latter we use the master chain discussed previously. Since stars have not be removed from the FLS catalog, we add a Gaussian distribution centered at (–0.4, –0.6) with σ=0.2 to simulate the stellar contribution. Lastly, the $N(z)$ used is comb-like covering $z = 0.1 - 1.0$. Although, not perfect in detail, this nonetheless shows that the essential elements of the observed FLS colour-colour plot are well reproduced by our model.

We now test our predictions on the use of the MIPS $24\,\mu$m filter for distinguishing various types of $z > 1$ sources. Ivison et al. [80] present the *Spitzer* colours of nine MAMBO sources. The $1200\,\mu$m MAMBO filter, by virtue of its negative k-correction (climbing the Rayleigh-Jeans tail of the thermal dust emission peak), selects higher redshift sources. Ivison et al. already indicate how the *Spitzer* colours can be used to separate out AGN from star-formation(PAH)-dominated sources. In Fig. *3.6.2* we show their data overlaid with our simulations. We note that the use of this plot for even rough redshift estimates is complicated by the large variations arising as the PAH $7.7\,\mu$m feature complex enters and leaves the $24\,\mu$m filter. In addition, highly obscured starforming sources would appear AGN-like in this diagram.

3.6.2 Selection of obscured AGN

Our model suggests, that the two 'bunny ears' in the FLS colour-colour plot separate the $z \sim 0 - 1$ continuum-dominated sources (right ear) from the $z \sim 0.1 - 0.3$ PAH-dominated sources (left ear). Thus our simulations have helped in establishing a new approach to selecting AGN in a dust-obscuration independent way. The idea is that since in the mid-IR the effect

of dust is much less severe than in the optical, if we can select AGN in the infrared alone we will have a dust-independent sample of AGN (up to the Compton-thick regime). Above we have shown that the distinctive power-law spectra of AGN provide us with an easy colour-selection for AGN at least up to $z \sim 1$. By comparing optically-selected (SDSS) quasars with infrared-selected ones (via the above technique) within the same luminosity range, it has become apparent that at least 50% of AGN are missed due to dust obscuration [96]. Similar conclusions are reached by other groups based also on mid-IR or X-ray colours [164, 173]. The sample of obscured AGN selected by us in the above fashion was subsequently confirmed as AGN via spectroscopic follow-up [95].

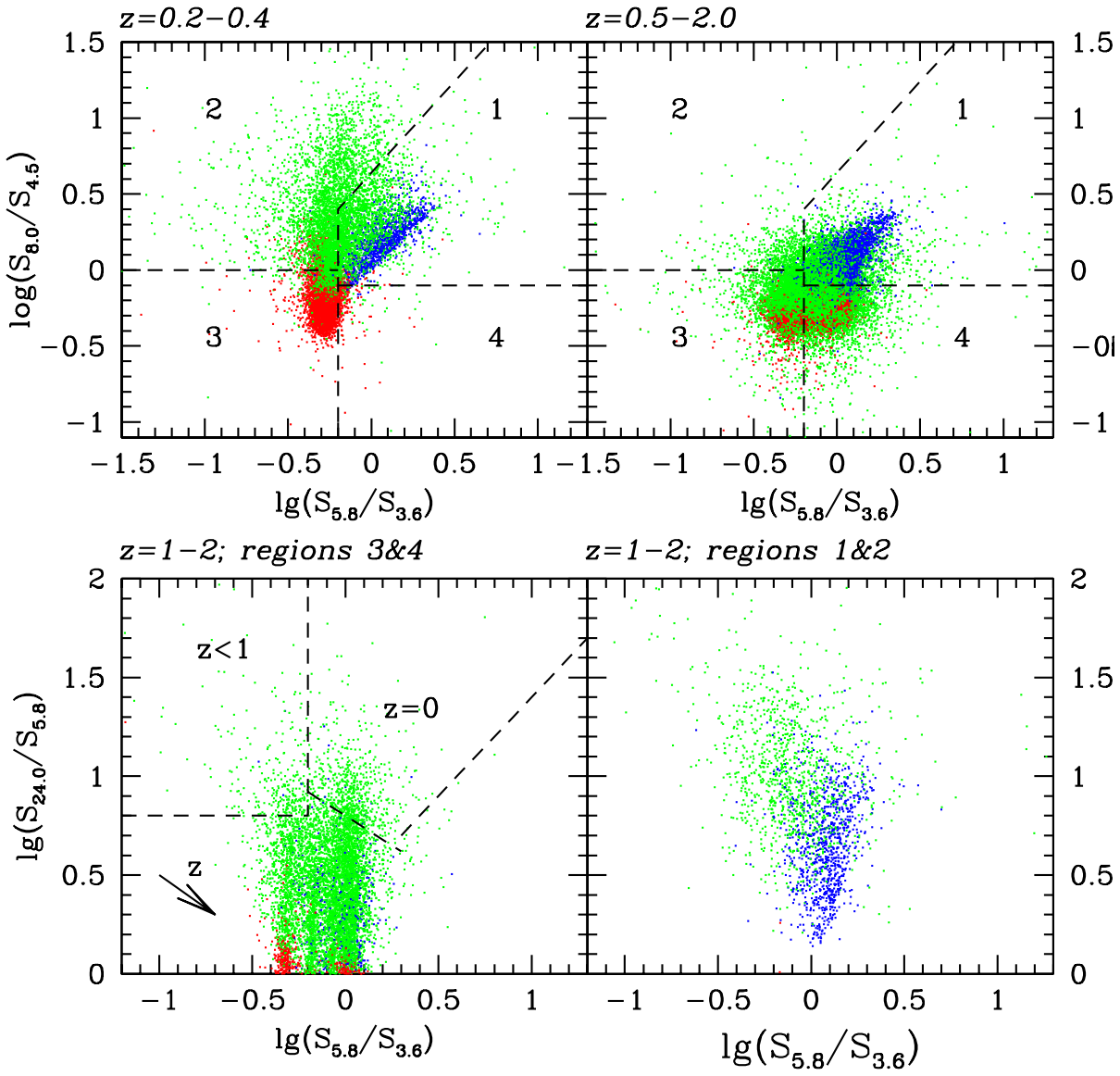

Fig. 3.10: The $z=0-2$ colour evolution based on our simulations. The colour scheme is as in Fig. *3.5.2*. The top panels are divided into regions which preferentially select continuum-dominated sources at $z\sim0-2$ (region 1), PAH-dominated sources at $z\sim0.05-0.3$ (region 2), stellar- and PAH-dominated sources at $z\sim0.3-1.6$ (region 3), and same at $z\gtrsim1.6$ (region 4). The bottom panels show simulations in the range $z=1-2$ only. The $z=0$ region shows the spread of colours for our sample, while the $z<1$ region is our best guess based on the assumption that the $\log(S_{24}/S_{5.8})$ will not drop below this range before the 24 μm filter begins to sample the 10 μm dip at $z\sim1.5$. Stellar-dominated systems here are off-scale (see Fig. *3.5.4*). See

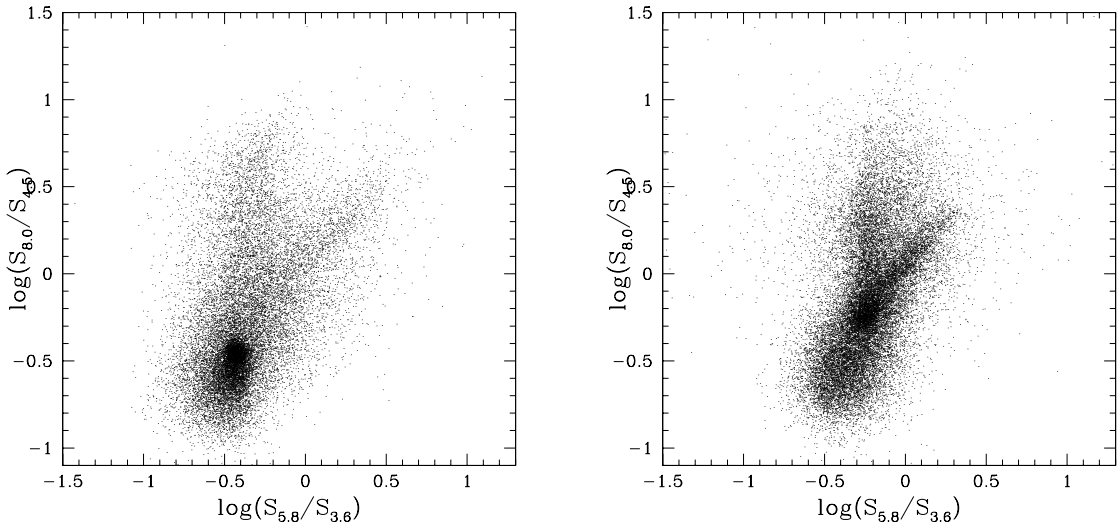

Fig. 3.11: *Left:* The FLS IRAC colour-colour plot. *Right:* A simulation from our model with a flat $N(z)$ distribution $z = 0.1 - 1.0$ a 8 mJy noise (consistent with the FLS flux errors). This plot also includes a Gaussian distribution around (–0.4,–0.6) with σ=0.2 to represent stars in the field, since these are not removed from the FLS data in the other panel. The highest density region is due to $z \sim 0.5 - 1$ sources.

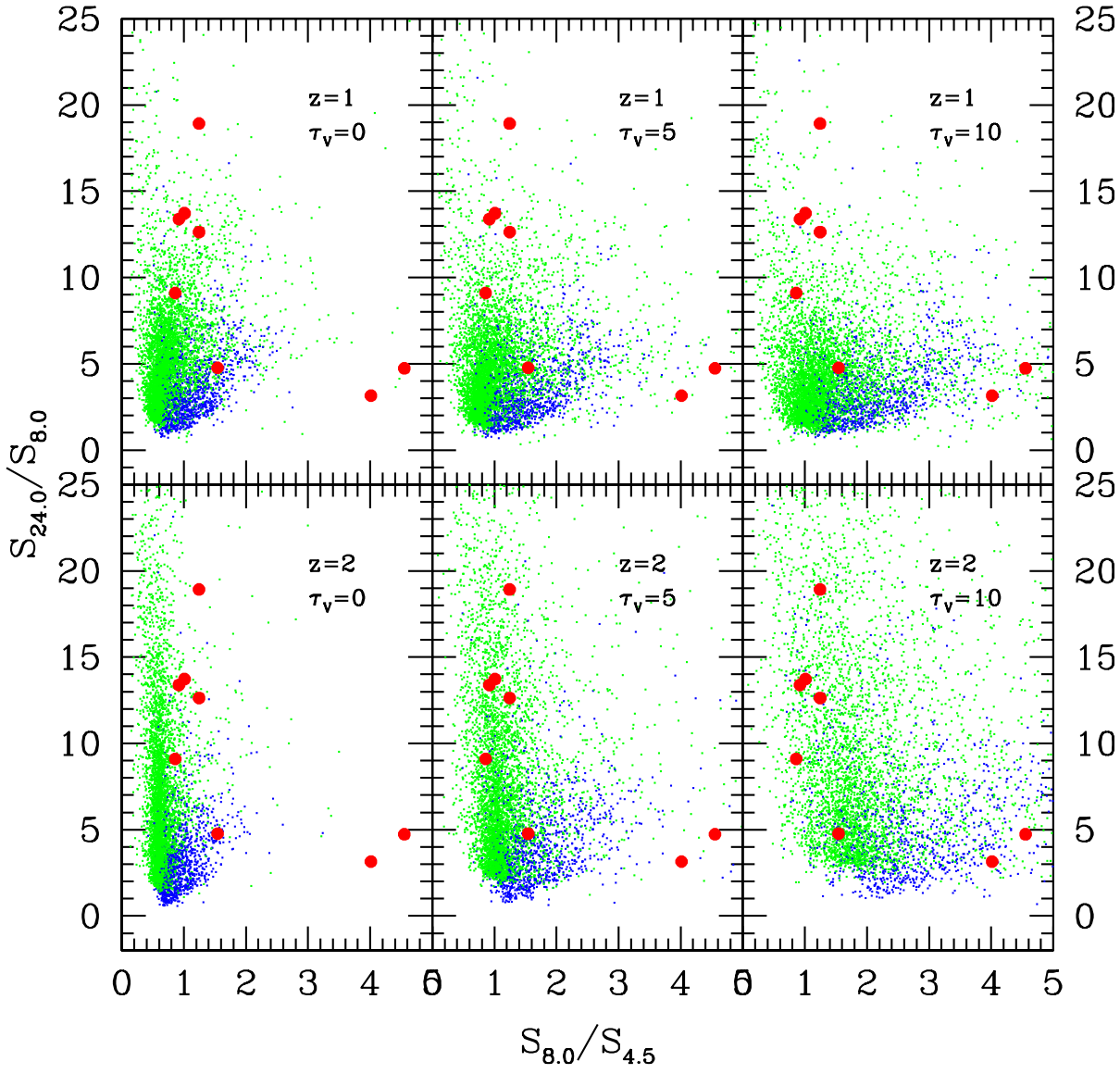

Fig. 3.12: The effects of extinction. Here, as usual, green indicates PAH-dominated sources and blue is continuum-dominated sources. The red filled circles are the MAMBO sources from Ivison et al. [80].

CHAPTER 4

THE INFRARED SEDs OF FIRBACK GALAXIES

In Chapter 1, we discussed the importance of knowing the shape of the infrared SED of galaxies and how it varies across galaxy populations. Typically, however, only a few broadband photometric points are available for galaxy evolution surveys. When modelling such populations, these few points need to be extrapolated via SED templates. But how accurate are these? To what extend are they influenced by the earlier generations of infrared instruments? What is the range of their applicability to the newer facilities such as *Spitzer*? Wide-field multiwavelength infrared surveys are being planned for the near future – is our understanding of the SEDs sufficient for optimal use of the upcoming data?

In this chapter, we extend the model presented in Chapter 3 to include the far-IR/sub-mm regime. We apply it to a particularly intriguing sample of galaxies a better understanding of whose nature is crucial for our understanding of the CIB. We specifically focus on the use of the Markov Chain Monte Carlo approach for fitting the available broadband photometric data, and obtaining meaningful uncertainties for the physical parameters of interest. This rare view of the entire infrared SED in a coherent, non-*IRAS* selected sample allows us to explore various degeneracies and potential pitfalls when extrapolating from only a few photometric points.

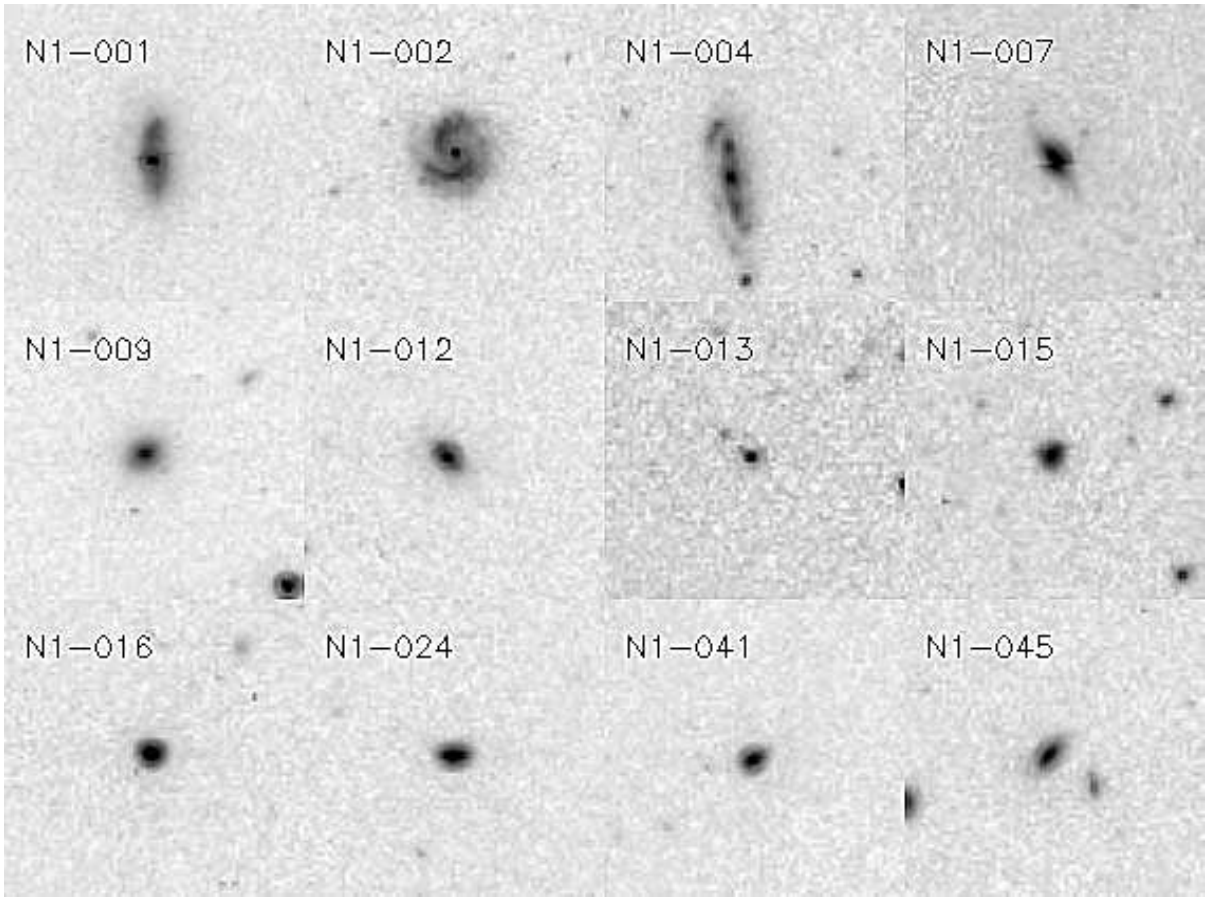

Fig. 4.1: IRAC 3.6 μm images for bright galaxies in our sample. Note the prevalence of disky morphologies with bright nuclei (N1-004 is a spectroscopically confirmed weak AGN) in our sample. Boxes are approximately 1.4 arcmin wide. For comparison, *ISO*'s 170 μm beam is $\sim$ 90 arcsec.

4.1 Data

4.1.1 **Sample selection**

The galaxies we discuss here are part of the Far-IR BACKground (FIRBACK) survey catalogue [37]. FIRBACK was a blank-sky survey with *ISO*'s ISOPHOT instrument at 170 μm. It was designed to resolve the CIB near its peak [98]. It includes three fields (FN1, FN2, and Marano South) totaling $\sim$4 sq.deg. FN1 and FN2 are inside the European Large Area *ISO* Survey (ELAIS;[120, 148]) N1 and N2 fields respectively (we often use ELAIS-N1, N1, and FN1 interchangeably). The $\sim$200 sources in the total ($> 3\,\sigma \equiv 135$ mJy) catalogue only succeeded in resolving $\sim$10% of the CIB contributors [37]. This was contrary to earlier expectations, due to the previously underappreciated role of cold dust in normal galaxies. Follow-up observations indicated that the FIRBACK sources (where counterparts could be identified) are consistent with mostly local, moderately starforming galaxies, although including some more luminous starbursts at $z \sim 0.5-1$. [155, 150, 123, 32].

The galaxies we focus on come from a sub-sample of the ELAIS-N1 FIRBACK sources which were selected on a basis of a radio identification and were later followed-up with SCUBA [155, 150]. The full sample of 30 targets was first presented in [150] where details of the sample selection as well as the near-IR (K) and sub-mm observations and data reduction are given. Here we additionally use *Spitzer* archival observations of the ELAIS-N1 field obtained as part of the SWIRE survey [110]. We use the *Spitzer* data to address the question of counterpart selection for the *ISO* sources, which brings our sample down to 22 sources (see Section *4.1.3*). SCUBA's smaller beam size allows us to find unambiguous counterparts for nearly all our radio/SCUBA sources (except N1-032, N1-034 and N1-059, which are therefore not part of the

final sample of 22 sources.

4.1.2 Treatment of *Spitzer* data

The basic data reduction and calibration is already performed on the individual frames obtained from the *Spitzer* archive. We use the Starlink software package CCDPACK to rescale, align and coadd the observations into common mosaic images for each of the 4 IRAC bands and the MIPS 24 μm band. Furthermore, the Starlink PHOTOM and GAIA packages are used to perform aperture photometry on the sources. To ensure that the sky-annuli chosen fairly represent the sky/background we monitor the sky values obtained for all of these and modify the annular region for any galaxy whose sky value is more than $3\,\sigma$ above the average sky. The flux errors are computed from the sky variance. The key question in this procedure is the appropriate aperture to use. In Fig. 4.2, we show the effect of varying the aperture for the 24 μm photometry, where the pixel scale is $2.5''$ and the aperture centre is the radio source position. Circular apertures are used in all cases, except N1-001, which is the only obviously elliptical source in the 24 μm image (several other sources are elongated as well in the higher-resolution IRAC images). In most cases, within the uncertainties, the flux values converge with increasing aperture size as expected, but often increase again for the largest apertures due to the effects of secondary sources in the field (we return to this point in the next section). We find that the 9 pixel apertures appear to offer the best compromise between including the total source flux and beginning to include additional sources.

Since we started on this project, the SWIRE team has released their own catalogues of the field [166]. These allow us to double check our IRAC and MIPS 24 μm photometry, as well as add a 70 μm point where available. In Fig. 4.2, we compare our results for the 24 μm

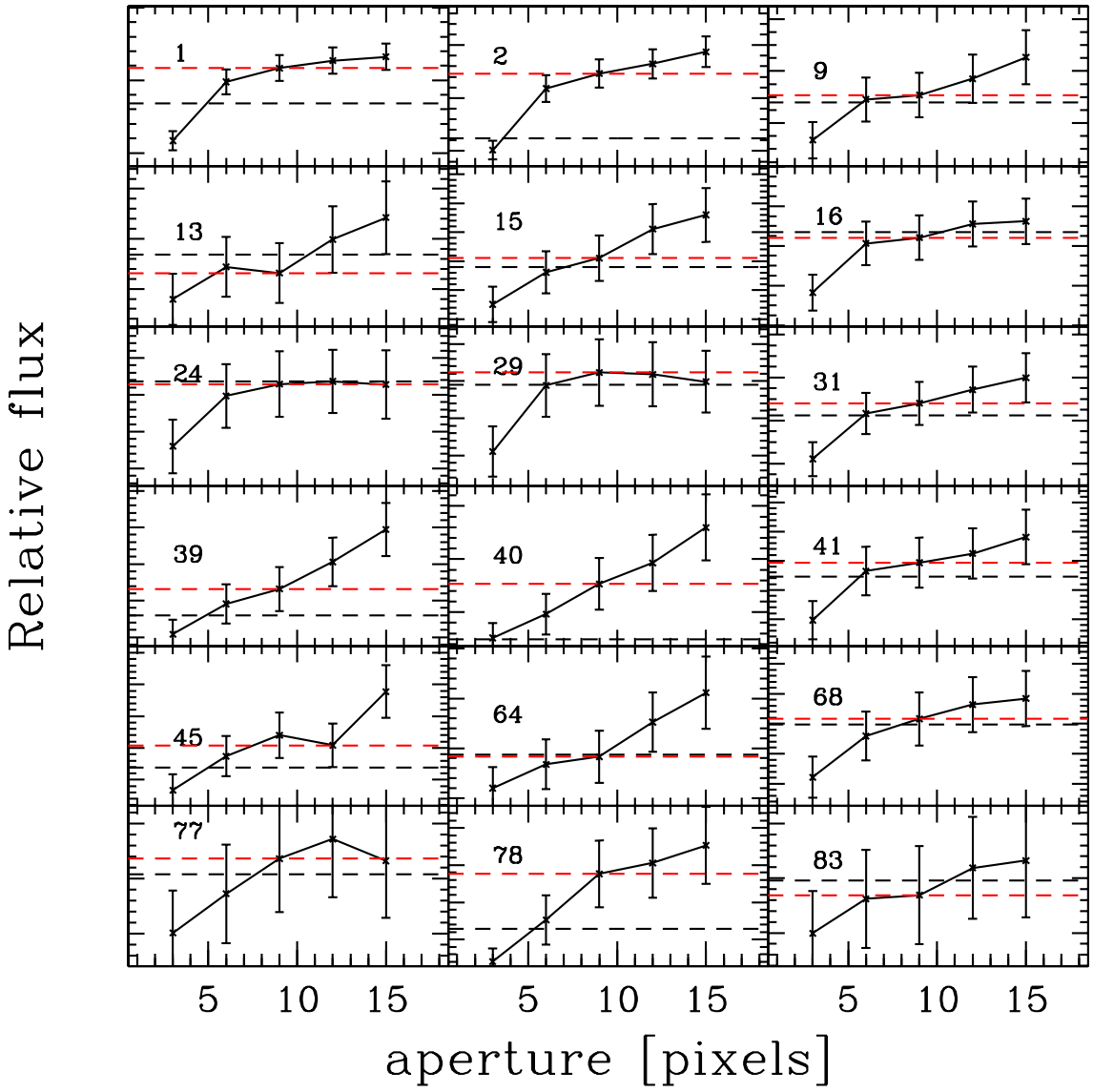

Fig. 4.2: The effect of increasing aperture on the 24 μm flux obtained. The red dashed line shows the final flux used. For comparison the black dashed line shows the value from the SWIRE catalogue. The errorbars are 1 σ uncertainties obtained from the sky variance.

fluxes with the corresponding fluxes in the SWIRE catalogue (from PSF photometry) and find generally good agreement (scatter within the $1\,\sigma$ uncertainties). The greatest deviations come from N1-001 and N1-002 (which are the most extended in the sample), and N1-040, which is a faint high-z ULIG where the SWIRE source is offset from our radio source, and N1-078 which is also a high-z source with two mid-IR sources within a SCUBA beam. For N1-004, N1-007, and N1-012 there are no $24\,\mu$m or $70\,\mu$m fluxes due to missing data. In addition to the SWIRE $70\,\mu$m catalogue, we extract fluxes for three faint sources: N1-040, N1-064, and N1-077. In all cases, the aperture resulting in the maximum flux was used in order to ensure all emission is accounted for. The only remaining source is N1-078 which is near the edge of the image and thus a confident flux estimate cannot be obtained. This is the only source where the mid-IR is not well constrained. For all of N1-004, N1-007, and N1-012 we have ISOCAM $15\,\mu$m and *IRAS* $60\,\mu$m fluxes compensating for the missing MIPS data. For the few cases which have both a $60\,\mu$m [32] and $70\,\mu$m detection (N1-001, N1-002, and N1-016), we find that the $60\,\mu$m fluxes are somewhat higher than the $70\,\mu$m ones contrary to any reasonable SED (given the S_{70}/S_{170} colours); but the difference is within the 20% calibration uncertainty assigned to the $70\,\mu$m flux. The SWIRE catalogue $70\,\mu$m flux for N1-001 (198 mJy) was most discrepant originally; however, it is an extended source and we find that a flux of 233 mJy is more accurate. This is the most severe difference we expect due to aperture effects for this sample. We do not explicitly use the few available $160\,\mu$m points, but note that within the uncertainties they are consistent with the *ISO* $170\,\mu$m points.

Near-IR J-band data for about 2/3 of our sample are available from the band-merged ELAIS catalogue [148], while the K-band data come from our previous work [150]. To convert to flux densities, we used zero points of 1600 Jy and 670 Jy for the J- and K-bands respectively. The

Spitzer fluxes are presented in Table 4.1 along with the rest of the multiwavelength data used here. A few of the sources have some (or all of) U, G, R, ISOCAM 15 μm, IRAS 60 μm and 100 μm fluxes [32]. In our present study, these are used primarily for consistency checks.

4.1.3 The role of multiple sources

In the previous section, it became apparent that the difference in resolution (from a few arcsec for IRAC to 15″ for SCUBA to 90″ for *ISO*) in the multiwavelength data we are assembling here makes the question of assigning the correct counterpart non-trivial. Here we would like to use the SWIRE ELAIS-N1 catalogue to address this issue for the FIRBACK catalogue as a whole and for our sample in particular. The problem is illustrated in Fig. 4.3. There, a subsection of the SWIRE ELAIS-N1 24 μm image is overlaid with the FIRBACK sources marked by 90″ white circles representing the *ISO* beam. The radio/SCUBA sources are marked by 15″ black circles standing for the SCUBA beam. The difficulty in identifying the correct *ISO* counterpart is obvious. We perform a simple test of this effect by taking every 24 μm source within a 45 arcsec radius of the *ISO* position. We then add all these fluxes and compare with the single brightest source within the centroid. The results are presented in Fig. *4.1.2* where we see that indeed nearly half of all sources *regardless of whether the full or* 4σ *catalogue is used* are not well described by assigning a single counterpart. This is a useful qualitative test, although it is unlikely to be correct in detail, because of complications such as foreground AGB stars, or combinations such as a bright local galaxy near a somewhat higher-z ULIG (where the latter might still contribute the bulk of the 170 μm flux). Nevertheless, it is evident, that nearly a half of the 170 μm-selected sources have 2 or 3 nearly equivalent mid-IR counterparts. Considering the position of the counterparts within the beam does not appear to affect this

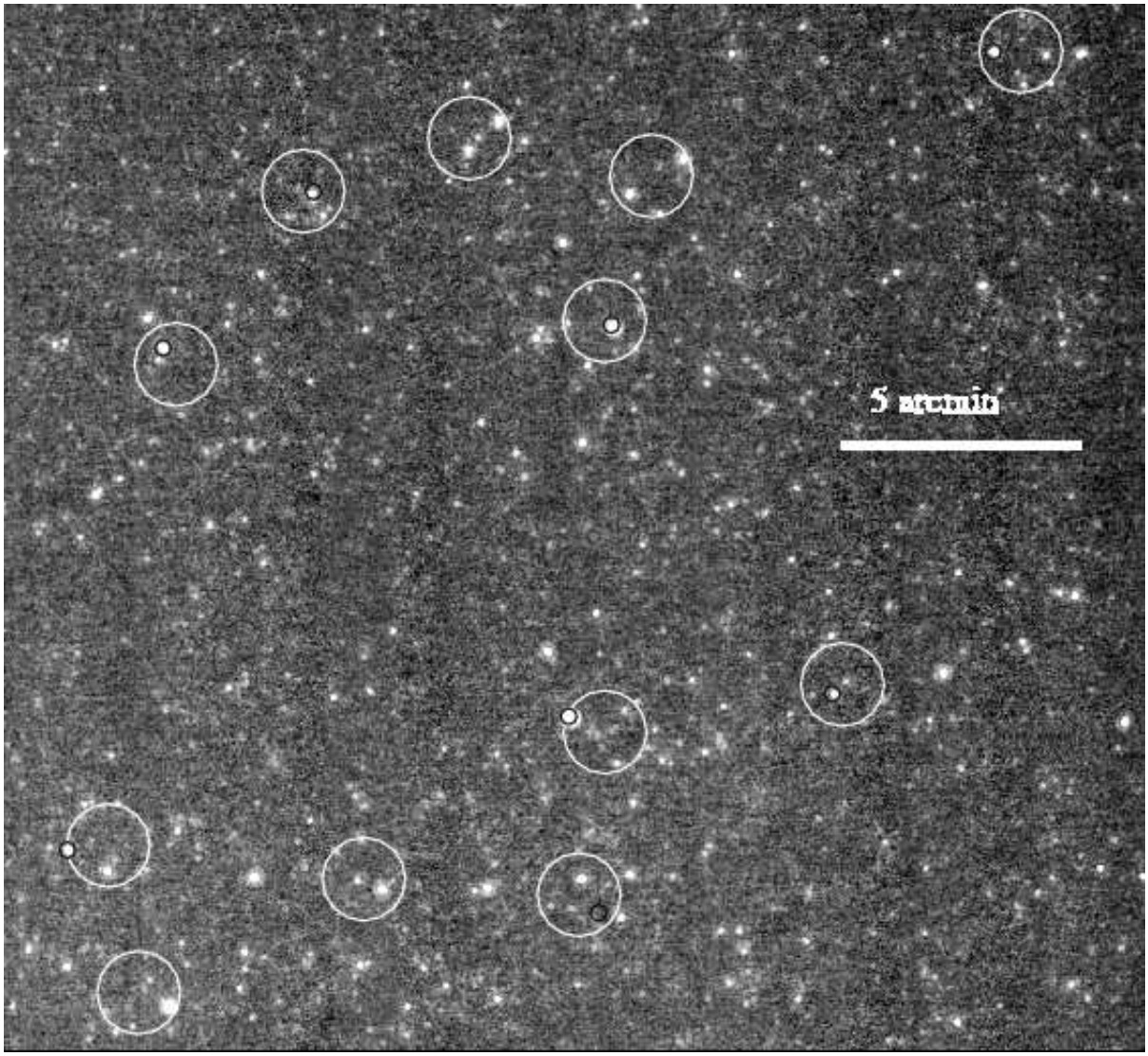

Fig. 4.3: A subset of the SWIRE ELAIS-N1 24 μm image. Here the large white circles are the *ISO* 170 μm sources with their 90″ beam, while the small black circles are the radio/sub-mm sources with the SCUBA 850 μm 15″ beam. Note the frequent incidence of multiple equal weight 24 μm sources within the *ISO* beams.

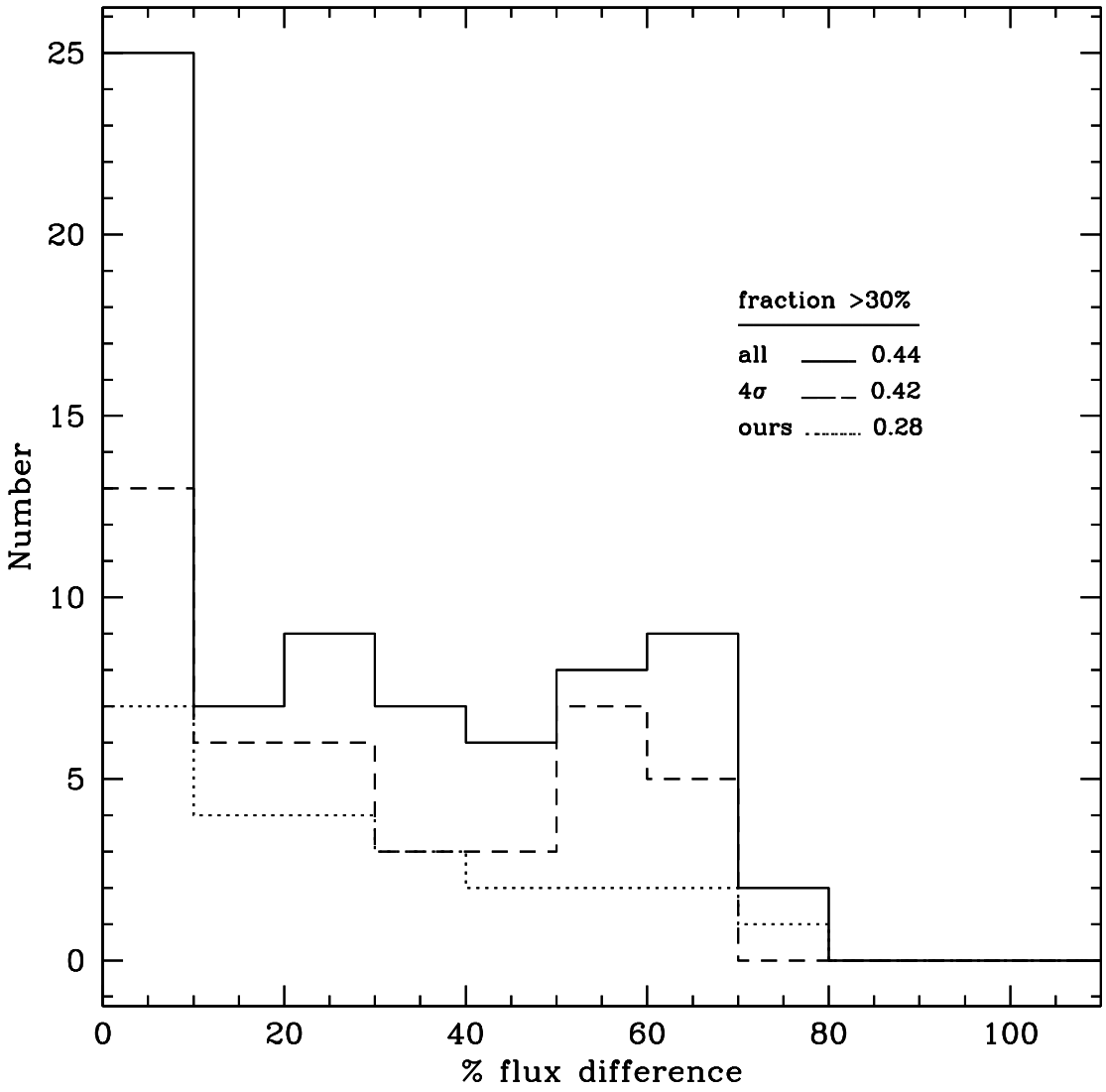

Fig. 4.4: Quantitative study of the potential effect of multiple sources within the *ISO* beam at 170 μm. These histograms show the distribution of flux differences at 24 μm between using just the brightest 24 μm source within the *ISO* beam versus using all sources within a 45 arcsec error circle. The solid line is for all FIRBACK sources, while the dashed line is for the sources in the $> 4\,\sigma$ catalogue. The dotted line is for our sub-sample of 30 radio-selected sources.

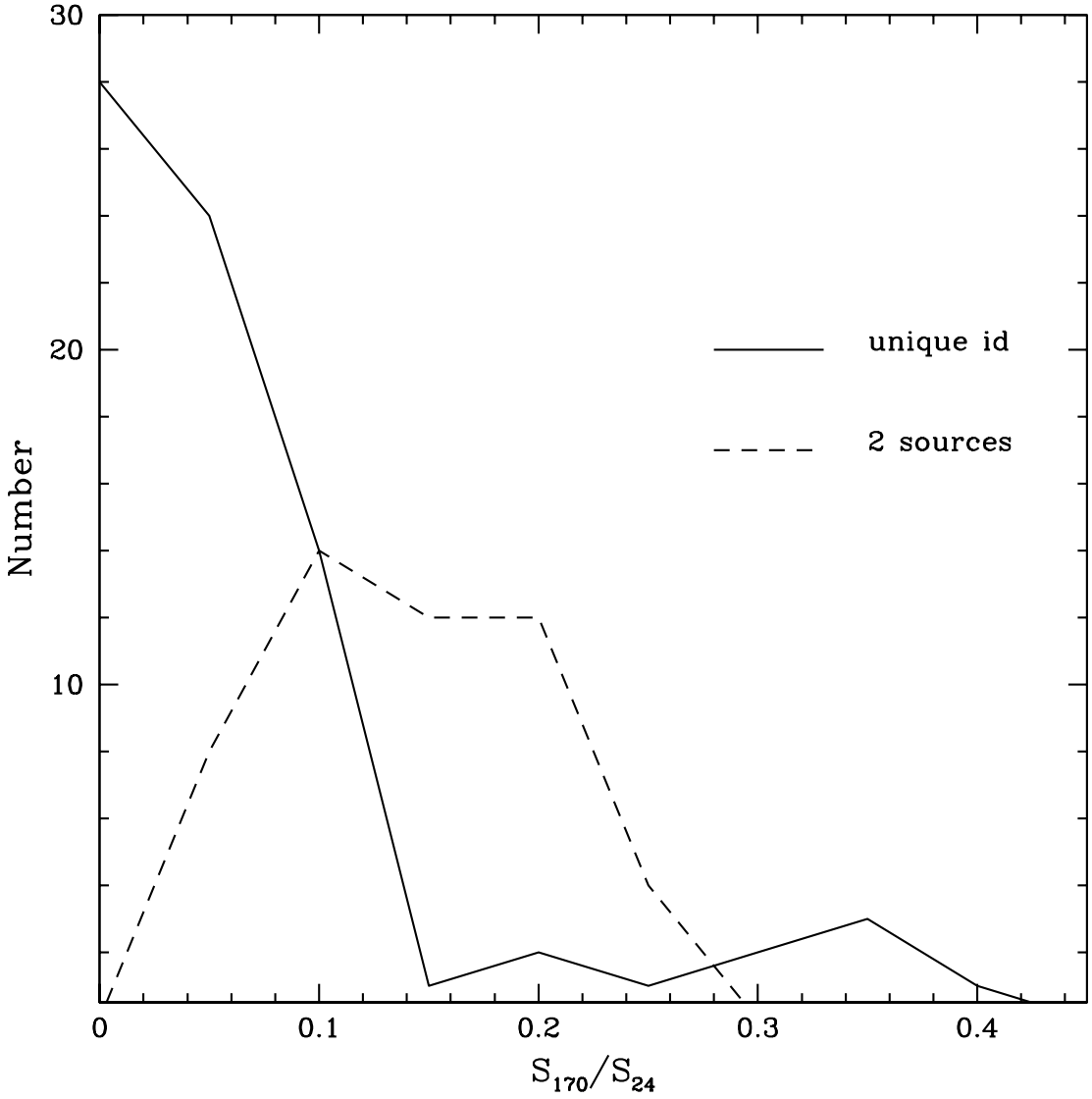

Fig. 4.5: Here we use the full ($3\,\sigma$) FIRBACK catalogue to compare the far-IR/mid-IR colours of the sources with unique identifications (solid line), and those with multiple identifications (dashed line). In the later case, the colours are computed by assuming two identical sources contributing to the $170\,\mu$m flux (i.e. colour $= S_{170}/\sum S_{24}$). Note that the later also implies that these sources are on average *fainter* in the mid-IR. The later are counted twice as two identical sources are assumed.

significantly. However, this fraction drops slightly for our radio-selected sample, although it is still significant. This general conclusion is in agreement with the results of Dennefeld et al. [32] who find 28/56 sources in the $4\,\sigma$ catalogue to have firm, unique identifications. Here we add that this fraction is unlikely to change significantly for the $3\,\sigma$ catalogue. We also find similar results for our FIRBACK sub-sample of 30 targets, with 28% having fainter $24\,\mu$m sources in the *ISO* beam contributing $>30\%$ of the flux of the brightest source (dotted line in Fig. *4.1.2*). Because of strong ambiguities, we remove 8 FIRBACK sources from our sub-sample. This leaves 22 sources for which the correct counterpart is reasonably secure (except N1-015 and N1-039, which are borderline), with other possible counterparts contributing a probable amount to the $170\,\mu$m flux which is of order the flux uncertainties or less. Since the beamsize at the other wavelengths is so much better than at $170\,\mu$m, the effects of multiple source contributors to the other fluxes are negligible. The effects of multiple contributors are already partially included in the $170\,\mu$m uncertainties which contain confusion noise [98].

As mentioned above, this test works for the sources of approximately the same redshift as it assumes a roughly homogeneous S_{170}/S_{24} colours. Although this is a relatively good assumption for the bulk of our sample, we know already that a sub-set of it is at somewhat higher redshifts ($z\sim 0.3-0.9$), whose S_{170}/S_{24} colours are expected to be higher (at least by a factor of 2). A few assumptions need to be made here. First, sources at $z>>1$ cannot be the principle contributor to the $170\,\mu$m flux as that would imply infrared luminosities $>>10^{13}\,\mathrm{L}_{\odot}$, of which, if present at all, we expect no more than 1 in the field therefore this scenario can be ignored in general. Thereafter there are four possibilities: a bright mid-IR source is present in the beam coincides with the radio source, a bright mid-IR source is present but does not coincide with the radio source, there are only very faint sources in the beam and one of them coincides with

the radio source, or the radio source does not have a mid-IR counterpart to the limits of the SWIRE survey. In the first two cases, it must be assumed that a dusty local source is very likely a significant contributor or at least cannot be excluded as such and therefore the test above applies. From our sample, this was the case with N1-008, N1-048, both of which also have two radio counterparts, N1-010, which was already noted by Dennefeld et al. [32] as the ISOCAM 15 μm source does not coincide with the radio source, N1-032 and N1-34, where the radio source has no mid-IR counterpart but there is a bright local galaxy in the beam. In addition, since the FIRBACK catalogue has been revised since the initial sample selection (in 1999) and better positions and flux estimates have emerged, two additional sources have been dropped: N1-056 as the radio source is no longer consistent with the *ISO* beam and 153 whose revised flux is now below the $3\,\sigma$ cut. For sources known or strongly believed to be at higher redshift the above test does not apply and therefore, we have taken the mid-IR source coinciding with the radio position to be the principal contributor regardless of its fraction of the total 24 μm flux (this includes N1-040, and N1-064). The sources confirmed at $z \sim 0.2-0.3$ (N1-015 and N1-039) or suspected so (N1-013, N1-077) are borderline (their mid-IR counterpart has $\sim 70\%$ of the total flux) but their non-zero redshifts mean that these identifications are fairly secure nontheless. After removing the 8 *ISO* sources which have the most ambiguous identifications at 24 μm, we are confident that the effects of multiple counterparts are not significant. We concentrate on this new sub-sample of 22 sources in the rest of this thesis. The *Spitzer* data for this sample along with the rest of the multiwavelength data used in this thesis is given in Table 4.1.

Note that the above source-by-source look at the effects of multiple sources compared with the rough 'fraction'-test lead to similar conclusions as to the percentage of our sample affected by multiple sources suggesting that this might be the case for the whole catalogue as well. In

the rest of this chapter, we will be discussing the detailed properties of the revised sample of 22 sources. However, given the large fraction of mltiple sources, can we generalize the conclusions for these sources to the FIRBACK survey as a whole?

It is difficult to answer this without a much more detailed modelling of the individual sources, but we can gain a rough idea by assuming that when multiple sources contribute (typically 2), we have exactly 2 identical sources such that the colour is now $S_{170}/S_{24,tot}$. Fig. *4.1.2* shows a comparison between the colour distribution of the uniquely identified sources, and those with multiple counterparts (under the above assumption)[1]. The distribution for the uniquely identified sources (such as our sample of 22) is reminiscent of the bimodal distribution in redshift/luminosity found for these galaxies from our *ISO*/SCUBA comparison [150]. The multiply identified sources then fill-in the gap. This can be interpreted as their being the sum of the two types rather than of two identical sources as assumed. However, they also appear to be on average fainter in the mid-IR which suggests that they are filling the gap with their physical properties instead. We will assume for now that our sample is indeed representative of the FIRBACK sample, and return to this bias in Section *4.4*.

[1]Note that a roughly equal number of FIRBACK sources has *no* 24 μm counterpart to the limit of the SWIRE survey and is likely, which may mean either >3 faint counterparts, or cirrus (for our sample these are: N1-034 and N1-056). This fraction drops for the $4\,\sigma$ catalogue.

Table 4.1: Multiwavelength data for our sample. All errors are $1\,\sigma$ estimates.

Source*	$S_{1.3}$ [a]	$S_{2.2}$ [b]	$S_{3.6}$ [c]	$S_{4.5}$ [c]	$S_{5.8}$ [c]	$S_{8.0}$ [c]	S_{24} [c]	S_{70} [c]	S_{170} [d]	S_{450} [b]	S_{850} [b]	$S_{1.4\mathrm{GHz}}$ [e]
	mJy	mJy	mJy	mJy	mJy	mJy	mJy	mJy	mJy	mJy	mJy	mJy
N1-001	6.28	7.31±0.54	2.97±0.32	1.98±0.26	4.67±0.4	12.25±0.66	21.7±1.8	233	597±72	–3.0±14.0	6.1±1.6	0.74±0.23
N1-002	4.58	5.55±0.41	5.35±0.43	3.79±0.37	9.6±0.59	23.97±0.92	12.3±1.2	112	544±69	14.4±12.4	4.4±1.1	0.64±0.04
N1-004	9.16	7.31±0.14	5.38±0.44	3.79±0.36	6.05±0.47	11.42±0.64	—	—	391±58	32.5±7.2	3.6±1.4	0.88±0.13
N1-007	4.40	3.5±0.26	3.65±0.36	2.41±0.29	4.09±0.38	11.87±0.65	—	—	338±54	23.4±8.1	4.4±1.6	1.04±0.12
N1-009	9.63	10.57±0.20	6.02±0.46	3.96±0.37	7.05±0.5	14.03±0.7	5.1±0.8	96	313±52	10.6±7.6	3.5±1.5	1.15±0.11
N1-012	1.75	1.84±0.30	1.15±0.20	0.75±0.16	0.81±0.17	4.24±0.39	—	—	302±51	9.2±10.0	1.5±1.6	0.31±0.07
N1-013	—	0.13±0.01	0.16±0.07	0.14±0.07	0.18±0.08	0.44±0.12	2.3±0.6	83	294±51	18.8±9.9	0.0±1.5	0.52±0.15
N1-015	0.36	0.80±0.06	0.57±0.14	0.53±0.14	0.37±0.11	2.05±0.27	4.1±0.7	49	294±51	–3.4±7.7	1.4±1.6	0.52±0.07
N1-016	2.71	3.5±0.26	1.78±0.25	1.41±0.22	1.61±0.24	7.6±0.52	8.4±1.0	160	289±50	34.8±16.7	1.5±1.2	1.55±0.13
N1-024	1.14	1.39±0.03	1.16±0.20	0.77±0.16	0.9±0.18	5.4±0.44	5.3±0.8	108	266±49	32.3±7.5	2.9±1.3	0.75±0.02
N1-029	1.10	1.27±0.09	1.24±0.21	0.88±0.18	0.75±0.16	4.25±0.39	5.2±0.8	72	229±46	20.0±14.2	0.5±1.7	0.69±0.05
N1-031	1.93	2.65±0.19	1.45±0.22	0.91±0.18	1.44±0.23	3.53±0.35	6.8±0.9	62	225±46	9.2±13.2	1.9±1.1	0.43±0.06
N1-039	—	0.32±0.05	0.28±0.10	0.25±0.09	0.19±0.08	0.8±0.17	2.3±0.4	44	205±44	10.9±86.8	–0.1±2.3	0.58±0.07
N1-040	—	0.01±0.01	0.08±0.05	0.07±0.05	0.06±0.05	0.05±0.04	1.5±0.3	26	205±44	29.2±20.5	5.4±1.1	0.33±0.03
N1-041	0.38	0.88±0.06	0.66±0.15	0.5±0.13	0.58±0.14	4.14±0.38	4.9±0.8	75	204±44	20.4±156.7	–0.1±2.5	0.76±0.06
N1-045	1.39	1.16±0.02	1.01±0.19	0.66±0.15	0.69±0.16	3.29±0.34	3.4±0.6	64	198±44	15.3±8.3	3.0±1.4	0.43±0.06
N1-064	—	0.03±0.01	0.15±0.07	0.11±0.06	0.12±0.07	0.09±0.06	1.8±0.5	14	166±42	35.2±13.9	5.1±1.2	0.23±0.04
N1-068	0.31	0.51±0.04	0.31±0.1	0.31±0.11	0.28±0.1	1.98±0.26	5.2±0.8	62	165±42	15.1±7.6	2.2±1.4	0.44±0.05
N1-077	0.31	0.42±0.07	0.37±0.11	0.29±0.1	0.23±0.09	1.4±0.22	1.7±0.4	42	159±41	5.9±7.3	1.1±1.3	0.40±0.10
N1-078	—	0.04±0.01	0.13±0.07	0.1±0.06	0.09±0.06	0.13±0.07	1.4±0.3	—	158±41	35.2±8.7	5.7±1.3	0.24±0.04
N1-083	—	0.46±0.08	0.31±0.1	0.25±0.09	0.18±0.08	0.68±0.16	1.3±0.4	43	150±41	16.2±16.0	0.7±1.2	0.55±0.03
N1-101	0.38	0.55±0.09	0.58±0.14	0.38±0.12	0.46±0.13	2.34±0.29	3.1±0.7	46	136±40	19.8±7.5	0.9±1.5	0.39±0.05

* The naming scheme follows Dole et al. (2001).

[a] J-band magnitudes from Rowan-Robinson et al. (2004). An uncertainty of 20% is assumed.

[b] UKIRT and SCUBA fluxes from Sajina et al. (2003).

[c] IRAC and MIPS fluxes from archival SWIRE observations, this work; S_{70} from the SWIRE catalogue, all assumed to have an uncertainty of 20%.

[d] ISOPHOT 170 μm data from Dole et al. (2001).

[e] VLA 21 cm fluxes from Ciliegi et al. (1999).

4.1.4 Spitzer colour-colour diagrams

Before we proceed with the analysis of this chapter, we would like to use this sample to compare the colour-colour simulations of Chapter 3 with the colours for our sample. Fig. 4.6 shows the colour-colour plots which are to be compared with the simulations in Fig. *3.6.2*. As expected, most of our sources fall in the $z<0.3$ part of the IRAC colour-colour diagram. The clump with $\log(S_{5.8}/S_{3.6})>0$ are N1-001, N1-002, N1-004, N1-007, N1-009, N1-013. Excepting N1-013 these are confirmed as the lowest redshift sources: all have $z \lesssim 0.06$. As discussed previously this colour moves toward the blue around $z \sim 0.05$ where the 5.8 μm filter leaves the PAH features. Thus for 5/6 sources above this is consistent (we return to N1-013 in Appendix B). The predicted high-z region of this colour space is occupied by N1-040, N1-064, N1-078, which are already known as higher-z sources from our previous study [150]. Their colours are slightly too red compared with the simulations, because, in our previous model, we do not take extinction into account and it becomes more significant with increasing redshift. As we shall show in Section *4.3*, all of these sources have significant optical depths, with N1-040 being the highest – consistent with its showing the highest $\log(S_{8.0}/S_{4.5})$ colour here. Apart from this correction, the agreement is remarkably good. When we turn to the IRAC-MIPS colour-colour plot the agreement is manifestly worse. In particular, our high-z sources now occupy a region which was expected to be $z \sim 0$ in Chapter 3, while the bulk of the sample is apparently in the $z>1$ region. Recall that in Chapter 3, we constrained our model at $\lambda<12\,\mu$m only. Thus the prediction for the behavior of these colours at $z<1$ is simply based on the assumption that the SED monotonically increases at $\lambda>12\,\mu$m which was our belief at the time based on standard templates. Fig. *3.5.2* however suggests that the SED decreases in the mid-IR. We discuss this in detail in Section *4.3*. In both plots we show our sample on top of the SWIRE ELAIS-N1 catalogue in order to ensure

that the above comparisons are generally valid and not simply due to some peculiarity of our sample. In particular, it appears that the decreased 24 μm emission in low-z galaxies is a feature of the SWIRE sample as a whole as well as our sample.

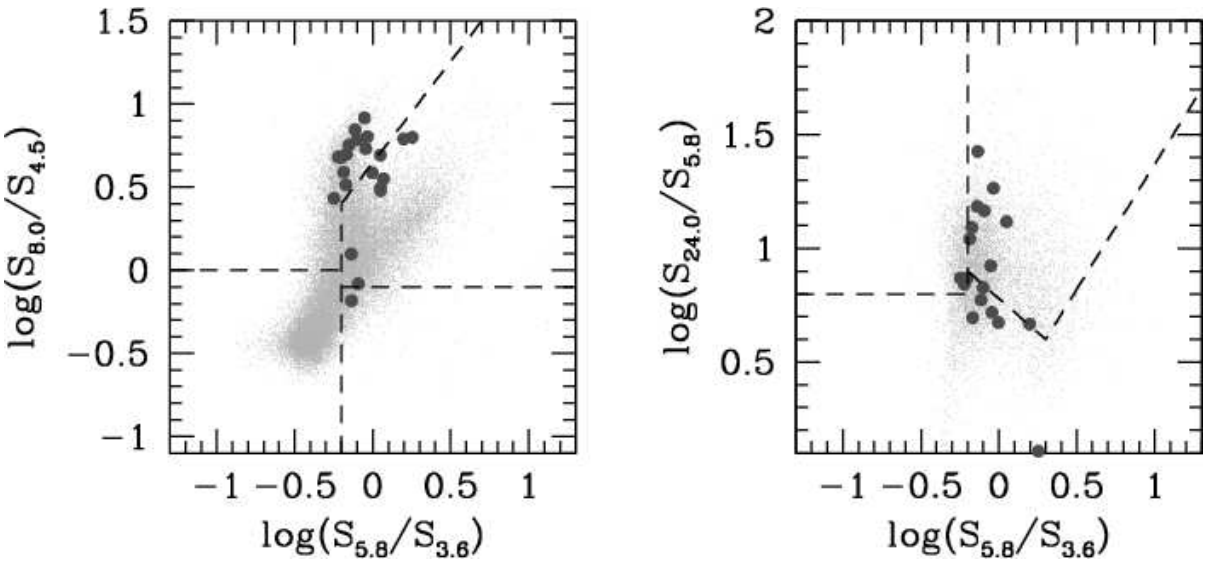

Fig. 4.6: The IRAC colour-colour plot for our sample (filled circles). For comparison we show the IRAC colours of the entire SWIRE ELAIS-N1 sample.

4.2 SED model

We adopt an approach to SED fitting, which is different from that adopted by most other studies. Our choice is driven by the desire to have a phenomenological model which fits known neearby galaxy SEDs robustly and yet has the flexibility (i.e. number of phenomenological parameters only slightly less than the number of data points we are trying to fit) which allows us to fit a wide range of SED types and in addition we want to be able to extract physical parameters with meaningful uncertainties. With these goals clearly in mind, our choice of detailed SED model is dependent on the quality and wavelength range of the data, while the

statistical approach we use is again the Markov Chain Monte Carlo method (see Appendix A).

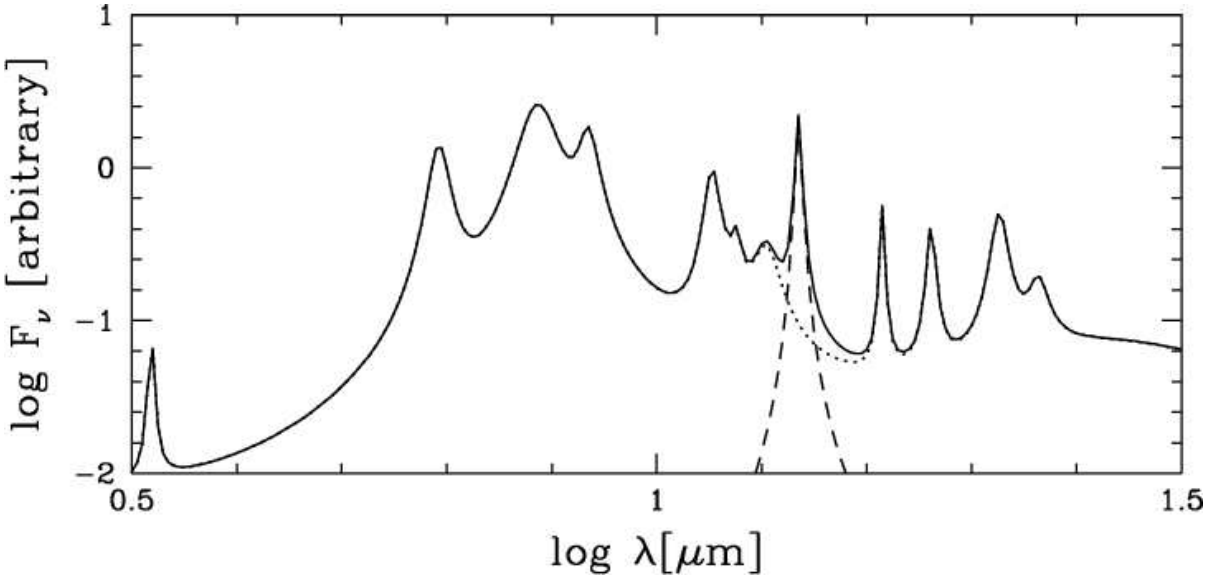

Fig. 4.7: The PAH template used. The dotted line is the theoretical template [41]. The dashed line is our addition of a 13.6 μm feature. The thick solid line is the total.

We model the SED as a sum of stellar emission, PAH emission, power-law emission, and thermal grey-body emission. This is similar to the mid-IR model used in the previous Chapter 3. A power-law, $f_\nu \propto \nu^{-\alpha}$, is a proxy for the warm, small grain emission (roughly $< 60\,\mu$m). This is cut-off as $\exp(-1700\,\mathrm{GHz}/\nu)$ in order not to interfere with the far-IR/sub-mm wavelength emission which is described by a thermal, $f_\nu \propto \nu^{3+\beta}[\exp(h\nu/kT) - 1]^{-1}$, component. Since we typically only have the 24 μm point to constrain this component, we fix α at 3.0, which smoothly connects this to the greybody component for normal galaxies and is consistent with the mid-IR slope of ULIGs. The stellar emission is accounted for by a 10 Gyr-old, solar metallicity, Salpeter IMF, single stellar population (SSP) spectral template generated with the PEGASE2.0 spectral synthesis code [52]. Using only an old stellar population template in

modelling the SED shape in the near-IR is a valid approximation as discussed in Chapter 3 and shown in Fig. **??**. The PAH template we use is a modified theoretical template (for neutral PAH molecules). Following, *Spitzer*'s recent discovery of a new PAH feature at 13.6 μm [ref], whose strength is comparable to the classical PAH features, we modify our template to account for it. Extinction, parameterized by $\tau_{\rm V}$, is applied using the $R_{\rm V} = 3.1$ Milky Way-type extinction curve [41]. This includes the 9.7 μm Si absorption feature, which thus becomes noticeable in this model at high opacities. We consider only a screen geometry, i.e. $I_\nu = I_0 \exp(-\tau_\nu)$. Fig. 4.8 shows the above phenomenological break-up of the SED. We solve for the best-fit model, and the associated uncertainties in the parameters via Markov Chain Monte Carlo (MCMC). Details of the fitting procedure and error analysis are given in Appendix A.

For $\sim 1/3$ of our sample spectroscopic redshifts are not available. Thus the necessity of photometric redshift estimates. We describe two different approaches to the problem and the best values obtained for these particular 6 galaxies in Appendix B. For simplicity, throughout the rest of this chapter we treat these redshifts as constant (as for the spectroscopic ones), and thus caution that the errors quoted on the various parameters for these sources are underestimated.

4.2.1 Optimal greybody fitting

A common approach, especially with a limited number of far-IR/sub-mm data points, is to fit a greybody function with characteristic temperature and emissivity. There are three main questions arising from the practice and interpretation of these fits:

1) what degeneracies are present in the usual formulation, and therefore what are the optimal parameters to fit?

2) given that this is only an approximation to the true shape of the SED, what effect does the

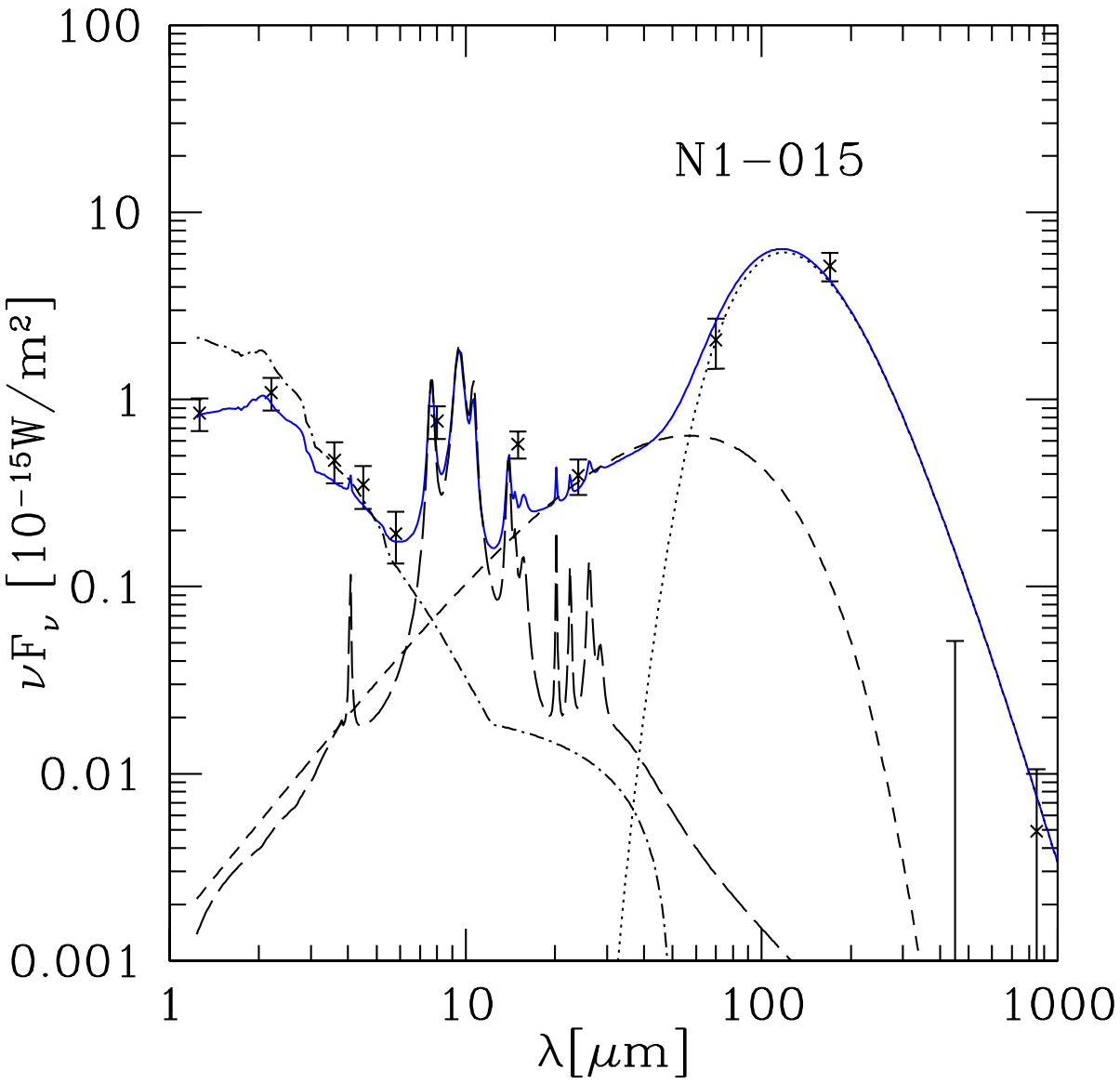

Fig. 4.8: An example of the SED model used here. This includes a greybody (*dotted line*), a warm power-law (*short-dash*), PAH emission (*long-dash*), and unextincted stellar emission (*dot-dash*) with $e^{-\tau_\nu}$ extinction allowed. The thick solid line is the total.

spectral sampling (such as due to redshift) have on the results obtained?

3) how does one disentangle physical correlations from said degeneracies?

Here we address the first two points and return to the last one in Section *4.3.4*. For further discussion, see also Blain et al. [8] and the alternative parameterization of Baugh et al. [5]. In essence, the function one is fitting has the form: $f_\nu = (\nu/\nu_0)^\beta * B_\nu$, where B is the Planck function:

$$B_\nu = \frac{2h}{c^2} \frac{\nu^3}{exp(h\nu/kT) - 1}. \tag{4.1}$$

The parameters to determine here are $T_{\rm d}$, β, and the nuisance parameter ν_0 (or some equivalent normalization). We wish to disentangle any correlations between the three. To begin with, to understand how degeneracies arise between the various parameters, we need to consider what it is that the code is actually fitting. Intuitively, to first order this is the overall amplitude of the dust emission, the position of the peak, and the slope in the Rayleigh-Jeans tail.

The first is the bolometric dust flux, $F_{\rm d}$, which is given by

$$F_{\rm d} = \int f_\nu d\nu = \frac{2h}{c^2 \nu_o^\beta} \left(\frac{kT}{h}\right)^{4+\beta} \Gamma(4+\beta)\zeta(4+\beta), \tag{4.2}$$

where Γ is the complete gamma function, and ζ is the Riemann zeta function[2]. Rearranging and substituting for $1/\nu_o^\beta$ removes the bulk of the degeneracies of the normalization parameter (which is now taken to be $F_{\rm d}$).

However the temperature and β are still correlated. As stated above, the fitting is also concerned with the position of the peak in the emission. By solving $df_\nu/d\nu = 0$ we obtain:

$$\beta = \left(\frac{h\nu_{\rm peak}}{kT}\right) \left[\frac{e^{h\nu_{\rm peak}/kT}}{e^{h\nu_{\rm peak}/kT} - 1}\right] - 3. \tag{4.3}$$

[2]Note that $\zeta(4+\beta)$ is ≈ 1 for any positive value of β, so does not affect the result much. $\log\Gamma(4+\beta)$ is closely approximated by $0.69(1+0.69\beta)$, which we use.

This equation provides a good fit to the observed correlation at higher values of β (see Fig. *4.2.1*), but fails as β approaches 1. The reason for this is obvious – apart from the peak, we also need to match the Rayleigh Jeans tail. The sub-mm data do not allow β to become arbitrarily shallow, although it can be compensated by increasing the temperature (which pulls the Planck function the other way). The constraint coming from the Rayleigh-Jeans tail can be parametrized with the sub-mm spectral index, $\alpha_{\rm submm}$ which is related to β, but in the Rayleigh-Jeans approximation the temperature dependence falls out leaving:

$$\beta = \alpha_{\rm submm} - 2\log(850/450) - 3. \tag{4.4}$$

Looking at our data (when the SNR at 450 μm was high), we find typical values of $\alpha \sim 5$, which means $\beta \sim 1.5$ from eq-n. 4.4, which is in fact often adopted for sub-mm sources. The joint constraint on the spectral index leads to:

$$\beta = \left(\frac{h\nu_{\rm peak}}{kT}\right)\left[\frac{e^{h\nu_{\rm peak}/kT}}{e^{h\nu_{\rm peak}/kT}-1}\right] + \alpha_{\rm submm} - 2\log(850/450) - 6. \tag{4.5}$$

In Fig. *4.2.1*, we show how the above two constraints act together and therefore how the available data drive the β and temperature values found. For example, in data without well determined peak position, assuming a low value of β (say, 1 – 1.5) will automatically lead to the conclusion of hotter temperatures. Conversely in data with cool temperatures and well determined peak, but poorly sampled sub-mm data, the conclusion will always be that β is high (even > 2 if the fit is allowed to go there). Better sampling (which could mean better SNR or more spectral points) in the sub-mm (relative to the peak) would likely change that un-physical conclusion. Conversely, as the redshift is increased, our data increasingly sample the peak rather than the tail of the thermal emission, and thus has the same effect. We return to point three here above in Section *4.3.4*.

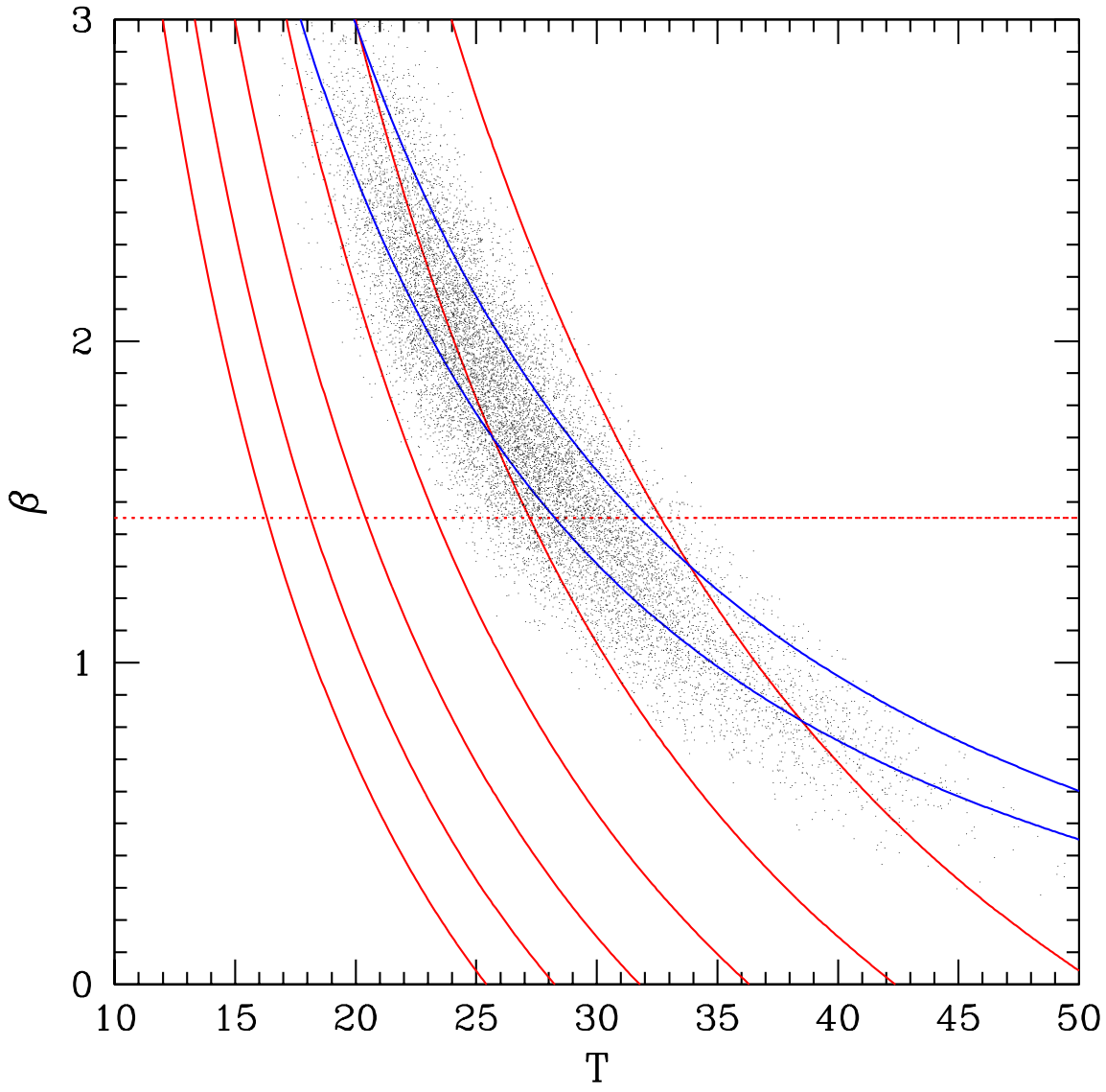

Fig. 4.9: Here we compare the relation in eq-n 4.5 and the observed degeneracy between the β and temperature parameters. The points are from the fit to N1-024. The red solid lines show the relation in eq-n 4.3, where the location of the peak moves in increments of 20 μm from 100 μm to 200 μm (top to bottom). Note the good agreement at higher β's and the deviation at lower-valued β's. The dotted line is the expectation of eq-n 4.4 with $\alpha_{\rm submm} = 5$ (consistent with observations). The solid blue lines are the combined constraint (eq-n 4.5) for peak locations of 160 μm and 180 μm respectively. Note that the observed distribution is now reproduced much better. Note that if not treated carefully, this parameter correlation, which exists in the fits *for each source*,

4.3 Results

After all this discussion, let us now prosent the results of our SED fitting procedure for our sample of 22 galaxies. The quantitative conclusions of our model-fitting are presented in Table 4.2, where the errors represent 68% confidence limits. The details of how the best-fit values and their uncertainties were arrived at is discussed in Appendix A. Note that, in Table 4.2, a quality flag is used to indicate whether or not problems exist with the fit, such as if the χ^2 achieved is poor, the results are ambiguous, or converged onto unphysical values. The ambiguous fits flag is used when the results for one or more parameter vary strongly depending on the method of arriving at the best-fit (see Appendix A). This is the case for the highest redshift sources where poor SNR in the near-IR and lack of sampling of the $\sim 6-11\,\mu$m PAH complex lead to these parameters (and their derivatives) being poorly constrained. The last flag is effectively only used when the best-fit β is $\gg 2$, although such instances are to be expected (see Section *4.2.1*). Below we discuss in turn both the general aspects of the fitted SEDs, and insights into specific physical properties.

Table 4.2: Derived properties for our sample. Errors are 95% confidence limits.

Source	z^a	$R^b_{\rm eff}$	T_d	β	$\log M_{\rm d}$	τ_V	$\log M_*$	$\log L_{3-1000}$	$\log L^c_{\rm PAH}$	SFR	qflag^d
		kpc	K		$M_\odot$		$M_\odot$	$L_\odot$	$L_\odot$	$M_\odot$/yr	
N1-001	0.030	4.41	25.4 ± 3.8	1.7 ± 0.5	7.09 ± 0.21	1.58 ± 9.86	9.37 ± 0.09	10.04 ± 0.06	9.07 ± 0.18	1.76 ± 0.25	2
N1-002	0.064	9.55	22.3 ± 5.0	2.0 ± 0.6	7.62 ± 0.21	5.41 ± 4.80	10.40 ± 0.18	10.62 ± 0.07	10.15 ± 0.16	5.3 ± 1.0	2
N1-004	0.064	14.29	23.0 ± 4.1	2.1 ± 0.5	7.59 ± 0.19	3.31 ± 3.38	10.37 ± 0.14	10.61 ± 0.07	9.69 ± 0.20	5.6 ± 1.2	1
N1-007	0.061	6.10	24.1 ± 6.6	1.4 ± 0.7	7.51 ± 0.23	5.40 ± 4.89	10.17 ± 0.18	10.42 ± 0.09	9.76 ± 0.19	3.6 ± 1.0	2
N1-009	0.053	5.56	23.3 ± 5.8	2.1 ± 0.6	7.16 ± 0.31	2.31 ± 2.64	10.22 ± 0.10	10.24 ± 0.07	9.66 ± 0.16	2.0 ± 0.5	1
N1-012	0.066	6.88	26.8 ± 6.3	1.9 ± 0.6	7.35 ± 0.34	2.20 ± 1.62	9.58 ± 0.10	10.44 ± 0.12	9.24 ± 0.19	4.1 ± 1.3	1
N1-013	(0.24)	12.12	26.5 ± 6.1	2.0 ± 0.7	8.43 ± 0.32	11.00 ± 4.90	10.29 ± 0.30	11.46 ± 0.11	9.70 ± 0.29	47 ± 12	1
N1-015	0.234	12.37	22.7 ± 4.7	2.0 ± 0.5	8.48 ± 0.35	2.77 ± 1.60	10.49 ± 0.17	11.39 ± 0.12	10.37 ± 0.19	36 ± 12	1
N1-016	0.092	6.10	31.5 ± 7.2	1.7 ± 0.6	7.46 ± 0.34	2.08 ± 1.89	10.18 ± 0.14	10.87 ± 0.07	10.29 ± 0.21	10.7 ± 1.9	1
N1-024	0.086	5.44	24.6 ± 6.8	1.8 ± 0.7	7.73 ± 0.23	3.28 ± 2.55	9.87 ± 0.15	10.60 ± 0.09	9.70 ± 0.17	6.0 ± 1.4	1
N1-029	0.144	9.75	26.2 ± 11.7	2.0 ± 0.8	7.85 ± 0.48	3.89 ± 2.38	10.33 ± 0.14	10.94 ± 0.12	10.12 ± 0.17	11.9 ± 4.0	1
N1-031	0.063	4.29	23.0 ± 10.1	2.5 ± 0.7	7.25 ± 0.51	1.96 ± 2.12	9.73 ± 0.10	10.16 ± 0.12	9.18 ± 0.19	2.03 ± 0.66	4
N1-039	0.269	14.21	25.2 ± 8.1	2.5 ± 0.6	8.44 ± 0.54	6.61 ± 4.65	10.47 ± 0.25	11.37 ± 0.16	10.23 ± 0.22	34 ± 13	4
N1-040	0.450	26.34	26.2 ± 5.4	1.9 ± 0.6	9.09 ± 0.20	18.76 ± 6.89	10.41 ± 0.37	11.82 ± 0.14	9.91 ± 0.40	110 ± 30	3
N1-041	0.120	7.85	25.3 ± 10.2	2.3 ± 0.7	7.63 ± 0.66	4.59 ± 2.47	9.94 ± 0.14	10.77 ± 0.14	9.95 ± 0.18	7.62 ± 2.86	1
N1-045	(0.03)	3.11	24.7 ± 8.5	1.7 ± 0.8	6.67 ± 0.39	3.48 ± 2.79	8.84 ± 0.12	9.38 ± 0.12	8.41 ± 0.19	0.38 ± 0.12	1
N1-064	0.910	17.54	31.1 ± 6.3	1.9 ± 0.7	9.30 ± 0.22	29.02 ± 7.57	11.40 ± 0.26	12.43 ± 0.12	11.73 ± 0.35	420 ± 140	3
N1-068	(0.19)	11.14	28.9 ± 15.8	1.5 ± 0.8	8.02 ± 0.53	3.07 ± 2.02	10.09 ± 0.19	11.07 ± 0.13	10.07 ± 0.21	19.1 ± 6.4	1
N1-077	(0.20)	11.60	26.5 ± 12.0	2.1 ± 0.7	7.91 ± 0.66	3.79 ± 2.43	10.11 ± 0.16	10.92 ± 0.14	10.06 ± 0.20	11.0 ± 4.3	1
N1-078	(0.91)	16.33	69.3 ± 14.5	1.2 ± 0.5	9.13 ± 0.25	27.20 ± 7.39	11.40 ± 0.23	12.90 ± 0.21	11.57 ± 0.38	1360 ± 570	3
N1-083	(0.20)	10.27	27.8 ± 11.6	2.0 ± 0.7	7.89 ± 0.56	5.56 ± 5.12	10.22 ± 0.19	10.93 ± 0.16	9.69 ± 0.27	11.8 ± 5.4	1
N1-0101	0.060	6.164	23.3 ± 11.5	2.1 ± 0.8	7.07 ± 0.66	4.79 ± 3.43	9.29 ± 0.20	9.90 ± 0.15	8.97 ± 0.19	1.05 ± 0.45	1

[a] Spectroscopic redshifts from Dennefeld et al. [32]; photometric redshifts are given in brackets (see Appendix B for details).

[b] The observed half-light radius at 8 μm converted to physical length.

[c] The integral under our full PAH template.

[d] Quality flag: 1=good; 2=$\chi^2_{\rm red} > 2$; 3=ambiguous fits; 4=unphysical values

4.3.1 General trends in the SEDs

Fig. 4.10 shows the data overlaid with the best-fit SED model for sources ranging between the $z \sim 0$ (top row) and $z \sim 1$ (bottom row). As expected, there is a greater range in SED shapes than accounted for by the data uncertainties. However, there are natural groupings, such as one can easily distinguish ULIGs (e.g. N1-064, N1-078) from starbursts (N1-015, N1-039) and from normal galaxies (e.g. N1-002). Details of the results derived from these fits will be discussed later. For now we focus on some generic features. In Fig. 4.11, we address the question of what is the 'typical' normal/cold galaxy spectrum based on our model fits. In order to minimize redshift bias, we construct a composite spectrum from all sources whose redshift is below 0.1, and for which 24 μm data are available. To minimize luminosity effects, we also normalize the spectra at 4.3 μm (which point resulted in the least amount of scatter across the SED). This procedure is consistent with results for *ISO* Key Project galaxies, where the stellar+PAH SEDs were found to be fairly constant [111]. Comparing the results with a number of common SED models, which produce good far-IR/sub-mm fits, we find that the mid-IR continuum for these galaxies has been uniformly overestimated. The first published 24 μm number counts [122] already suggested that the existing SED spectra might not be accurate in the mid-IR. To correct for this, the necessity for 'downsizing' the mid-IR in their starburst spectra was already pointed out by Lagache et al. [100]. It appears that, not surprisingly, such a correction is necessary for the cold (i.e. $T \sim 20-30$ K) galaxies as well. Note that the slight discrepancy we find between the *IRAS* 60 μm and MIPS 70 μm data (see Section *4.1.2*) might account for some of the observed gap at the far-IR end. This can be seen in the discrepancy between our composite SED and the Dale et al. [29] model (where we use the average $\log(S_{60}/S_{100})$ for the sources with *IRAS* detections). For comparison we plot both the old Lagache et al. [99]

cold galaxy model and the modified starburst model (used to explain the 24 μm counts). The starburst template naturally peaks at lower wavelengths; however, it provides a much better fit in the mid-IR. Lagache et al. [100] introduced the mid-IR modification simply as a possible way to match the observed number counts. Our study therefore confirms the validity of their assumption.

The cause for the discrepancy between previous SED models in the mid-IR and our current model is likely due to the fact that pre-*Spitzer*, 'mid-IR continuum' meant either ISOCAM 15 μm or *IRAS* 25 μm. The simpler models are a good approximation for galaxies with continuum-dominated mid-IR spectra (mostly AGN – see Chapter 3). However, for cold galaxies these are likely to be severly affected by PAH emission: the ISOCAM LM3 filter includes a forest of relatively weak features, as well as the strong 12.6 μm feature and the newly discovered, but quite prominent, 13.6 μm feature (see Section *4.2*); the *IRAS* 25 μm filter is about twice as wide as the MIPS 24 μm one, and might also be affected by mid-IR PAH features (see Fig. 4.7). The effects of mid-IR spectral features on broadband fluxes and colours have been discussed in greater detail in other studies [125]. Although investigating this further is beyond the scope of this thesis, it does appear that for fairly quiescent galaxies, with weak continuum and strong PAH emission, the previous broadband measurements have led to an overestimation of the mid-IR continuum. The effect of the PAH emission on the 15 μm fluxes is further supported by the fact that originally, for the sources without 24 μm fluxes (N1-004, N1-007, and N1-012), we obtained best-fit spectra with much stronger continuum, but after including the new PAH feature in the template (see Fig. 4.7), the spectra of these sources are more consistent with their *Spitzer*-constrained peers (see Fig. 4.10). Note that mid-IR spectroscopy pre-*Spitzer* was difficult to obtain, and thus relatively few such spectra exist. For

example, the low-resolution $2-12\,\mu$m spectra used in Chapter 3 are a large fraction of all such spectra available, and these are still much more common than $>12\,\mu$m spectroscopy and only exist for fairly active galaxies with strong mid-IR continuum (these being the only ones where suffucient SNR can be practically achieved). Thus the models were largely based on extrapolations from broadband photometry and a few spectra of bright sources. Note that moreover, the few available spectra are typically from local resolved galaxies, where only the central regions of the galaxy are sampled, such as Centaurus A [102]. This makes direct comparison with the colours of the integrated SEDs (such as all SEDs discussed here) difficult. We return to the point of centrally concentrated starbursts vs. extended disks in Section *4.3.5*. Here we merely note that even the more active (quite probably starbursting) galaxies in our sample have much cooler SEDs than that of the 'prototypical' starburst M82 (see [158] and references therein). We believe the most likely explanation for this discrepancy is not any uniqueness of M82, but rather the difference in the effective apertures.

Fig. 4.12 shows the best-fit SEDs for the two spectroscopically confirmed higher-z sources [19]. The dotted line represents Arp220 [158] at the appropriate redshift. In both cases the sub-mm data are well fit by the Arp220 template, but the mid-IR data differ by an order of magnitude. We note that our photometric highest-z source (N1-78) shows similar trends. Note that the PAH features in the best-fit N1-064 spectrum are not constrained by any data point and therefore a model with no PAH emission is quite acceptable as well (see the spread in Fig. 4.10). Despite it being poorly constrained for the few highest-z sources, we find clear evidence for prominent PAH emission for all sources in our sample, regardless of redshift (and hence luminosity). We explore further the relation between overall luminosity and PAH emission in Section *4.3.2*.

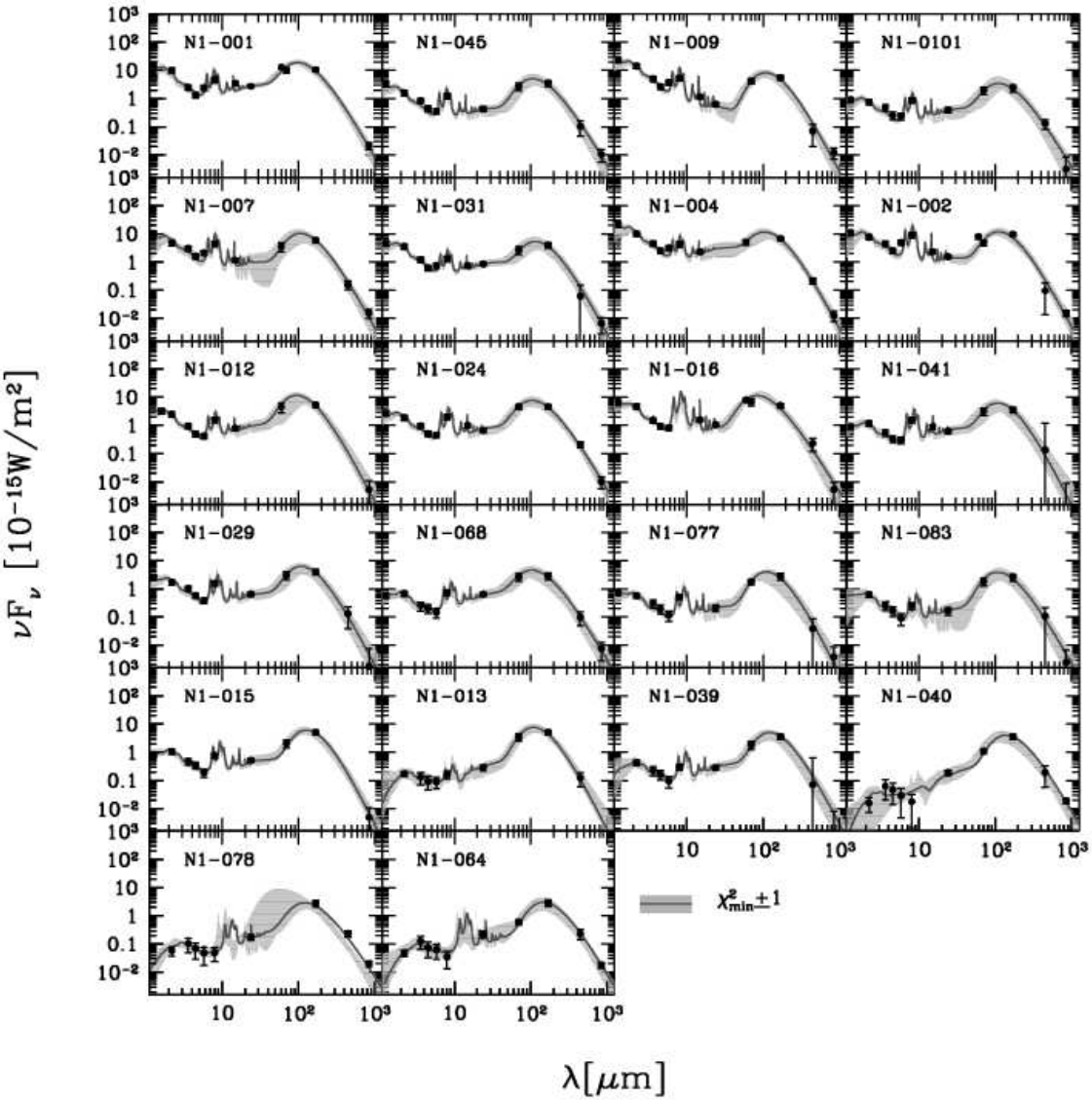

Fig. 4.10: The SED fits for our sample, where we show both the data and best-fit model together with an uncertainty band. Note that the least well-defined SED is that of N1-078, which is the only source without data in the range $24\,\mu$m$-170\,\mu$m. Redshift increases from top to bottom. Note the characteristic increase in the dust-to-stars emission ratio as one goes to higher (and hence more luminous) redshift sources.

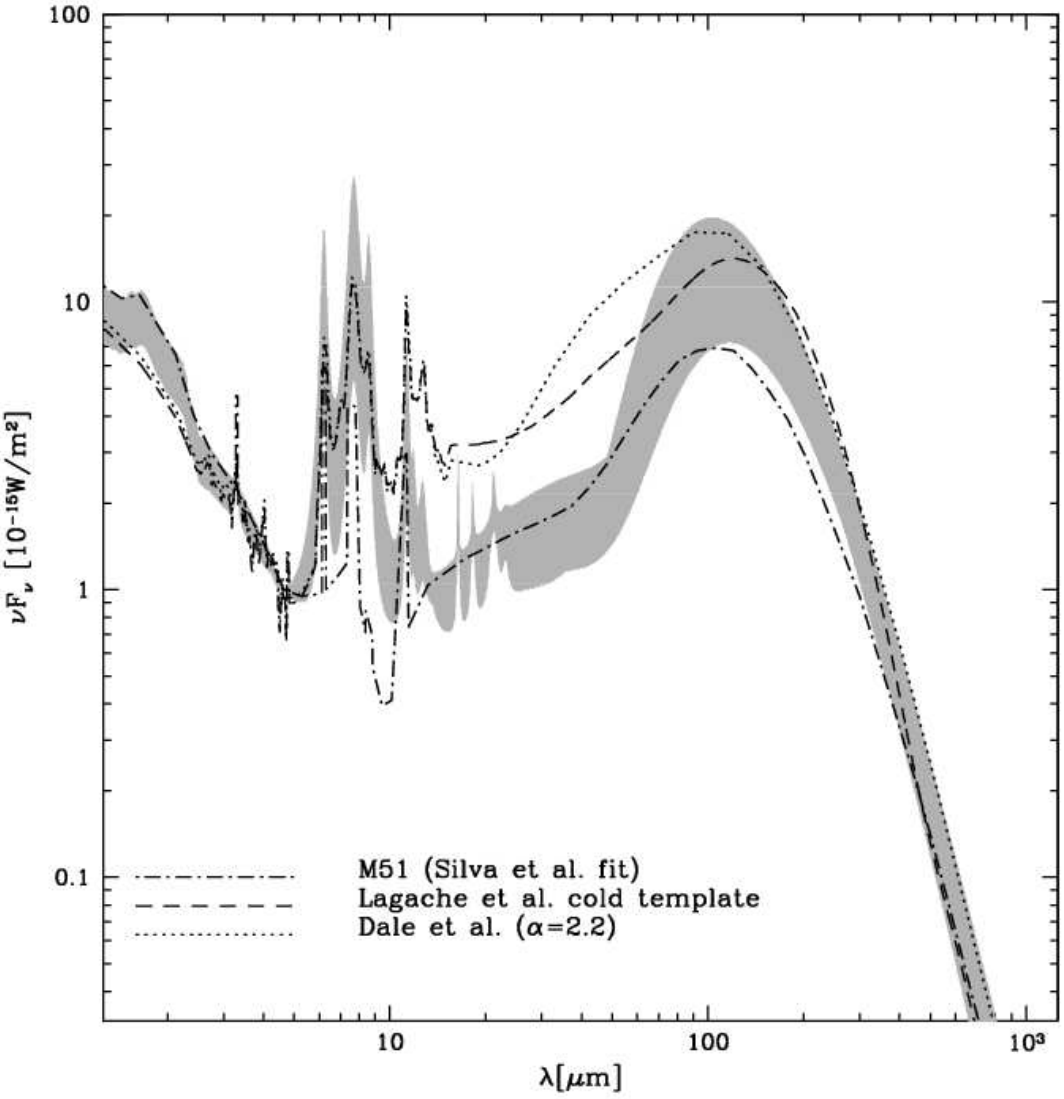

Fig. 4.11: The shaded region represents the range of spectra, where we have included all sources with $z < 0.1$ and which have 24 μm data. All SEDs are normalized at 4.3 μm, which is a neutral point between pure stellar and PAH emission. The shaded region should be regarded as a composite spectrum, representative of the 'cold' FIRBACK sources. For comparison we overlay a number of templates (see legend).

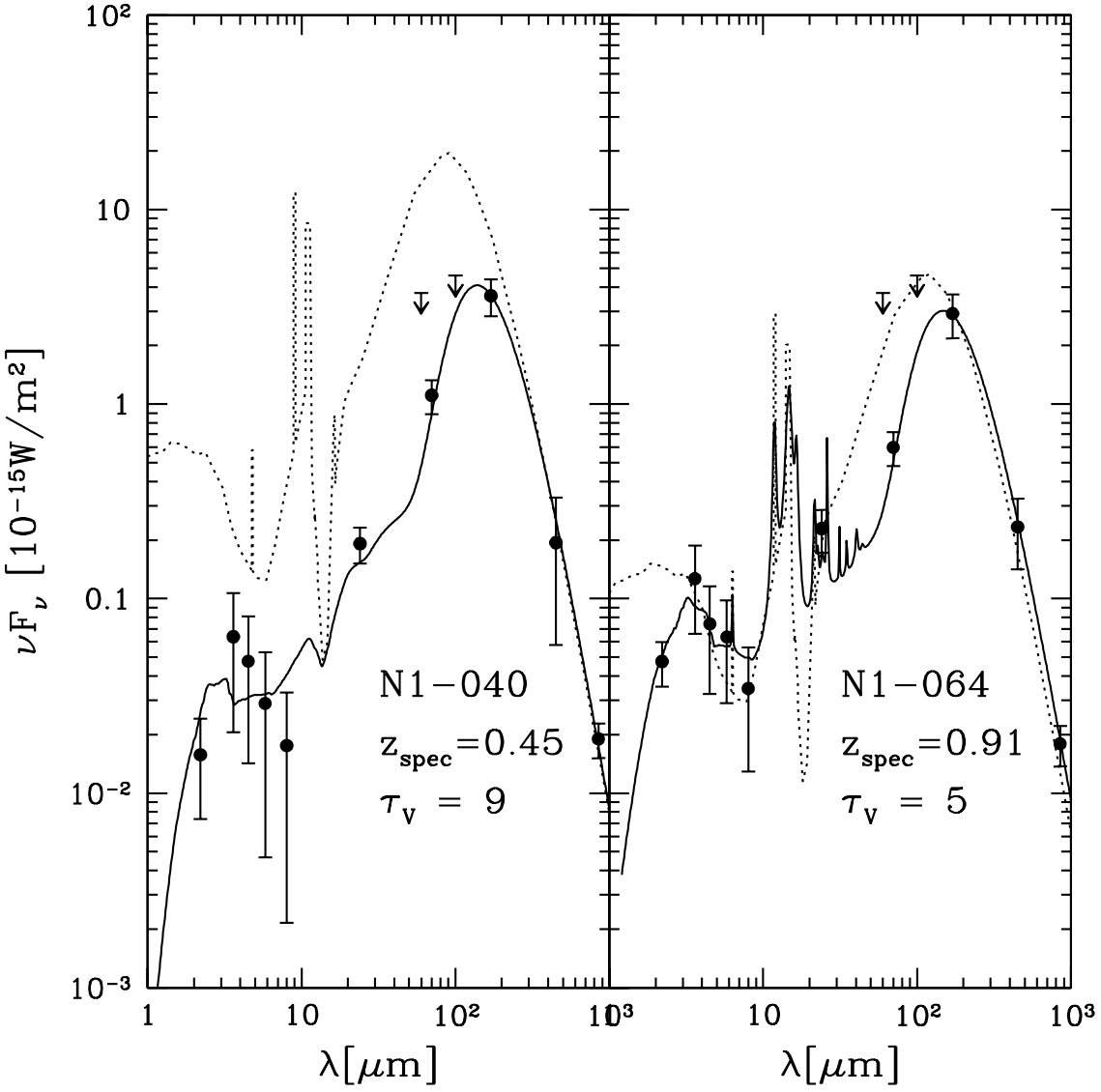

Fig. 4.12: The SEDs for the two spectroscopically-confirmed higher-z sources. The *IRAS* upper limits are also shown, although they are not included in the fit. The dotted line shows the appropriately redshifted Arp220 template [158]. The *Spitzer* fluxes suggest much cooler and less luminous sources than previously assumed.

4.3.2 Luminosities and SFR

In this section, we address both the total infrared power output of our sources (L_{3-1000}), and the luminsity due to PAH emission alone (see Table 4.2). Our model fitting is done in power vs. $\log(\lambda)$ where the power is in $10^{-15}\mathrm{Wm}^{-2}$ units[3]. Below is the equation we use to derive luminosities using this setup, and how it relates to the more common flux/frequency plane:

$$L \propto \Sigma F_\nu d\nu \equiv \Sigma \nu F_\nu \frac{d\nu}{\nu} \equiv \ln 10 \Sigma \nu F_\nu d\log\nu \equiv \ln 10 \Sigma \lambda F_\lambda d\log\lambda;$$

$$L_{3-1000} = 2250 \times 4\pi D_L^2 \ln 10 \Sigma_3^{1000} \lambda F_\lambda d\log\lambda \ \ [\mathrm{L}_\odot], \tag{4.6}$$

where $d\log\lambda = 0.005$ for the steps used in our modelling, which is another argument for the convenience of using constant $d\log\lambda$ for the x-axis here (in addition to the ease of redshifting as discussed in Appendix B). D_L denotes luminosity distance (defined so $D_L = (L/4\pi F)^{-1/2}$ for any cosmology[4] [17].) in Mpc. The overall luminsoties we derive are typically a few $\times 10^{10}\,\mathrm{L}_\odot$ for our lower-z targets, consistent with roughly L^* galaxies (see Fig. **??**). L_{PAH} is obtained in an identical manner, except that the summation is over the PAH component alone. We find the $L_{\mathrm{PAH}}/L_{\mathrm{IR}}$ fraction to be fairly constant at $\sim 5-10\%$. This is consistent with the results for the *ISO* Key Project galaxies [29]. In Fig. 4.13 we compare our results with previous estimates of the mid-IR/total-IR ratio. The solid lines are the best-fits for our sample. The relations are:

$$\log L_{\mathrm{PAH}} = (0.83 \pm 0.09) \times \log L_{\mathrm{IR}} + (0.8 \pm 1.0); \tag{4.7}$$

$$\log L_{24} = (1.15 \pm 0.04) \times \log L_{\mathrm{IR}} - (2.7 \pm 0.5). \tag{4.8}$$

[3]This is a convenient unit, as it results in values near unity and at the same time can be converted to observables easily, since multiplying by λ in μm and dividing by 3 leads to the flux in mJy.

[4]In the presence of a cosmological constant term and no curvature, the evaluation consists of the integral $D_L = (c(1+z)/Ho)\int_0^z [(1+z)^3\Omega_M + \Omega_\Lambda]^{-1/2} dz$

In the top panel of Fig. 4.13 we compare $L_{\rm PAH}/L_{\rm IR}$ for our galaxies with estimates from *ISO* (CE01; [23]) and *IRAS* (T05; [**?**]). Note that our results are consistent with all including L_{15} further supporting the PAH contribution to this mid-IR filter. Note that the traditional explanation for the similarity of the relations here is that the continuum and PAH components rise in proportion to each other. However, recall that the highest luminosity sources here, N1-064 and N1-078, are ambiguous in their $L_{\rm PAH}$'s (see Appendix A). Therefore, a suppression of PAH luminosity with luminosity cannot be excluded for these ULIGs. The two LIGs where such a suppression can be seen are N1-013 (whose redshift is uncertain), and N1-040 (where the suppression is definitely present).

The bottom panel of Fig 4.13 compares the relation between the *IRAS*-based L_{25} with our *Spitzer*-based L_{24}. The slopes are fully in agreement. It is clear however that our $24\,\mu$m fluxes are systematically below, by ~ 0.4 dex, those expected from *IRAS*. This is most likely due to the difference in the *IRAS* and MIPS filters. The sample used for the *IRAS* relation is flux-limited to all four *IRAS* bands leading to a bias toward sources with stronger warm continuum unlike our $170\,\mu$m where the selection is biased toward the presence of cold dust instead. Overall this follows from our discussion in Section *4.3.1.* As a consistency check, in Fig. 4.14, we examine the IR-radio correlation (for a recent discussion and full references see [132]), and find an excellent agreement with slope consistent with 1 as expected [132].

The total infrared luminosity is well known to trace the current SFR of a galaxy (e.g. [87, 91]). We use the Kennicutt relation here which is:

$$\mathrm{SFR} = (1.8 \times 10^{-10})\mathrm{L}_{8-1000}[\mathrm{M}_{\odot}\mathrm{yr}^{-1}], \tag{4.9}$$

where L_{8-1000} in in solar units. Note the slightly different definition of $L_{\rm IR}$, which is accounted for here (i.e. $8-1000\,\mu$m rather than $3-1000\,\mu$m). A harder to quantify uncertainty is that

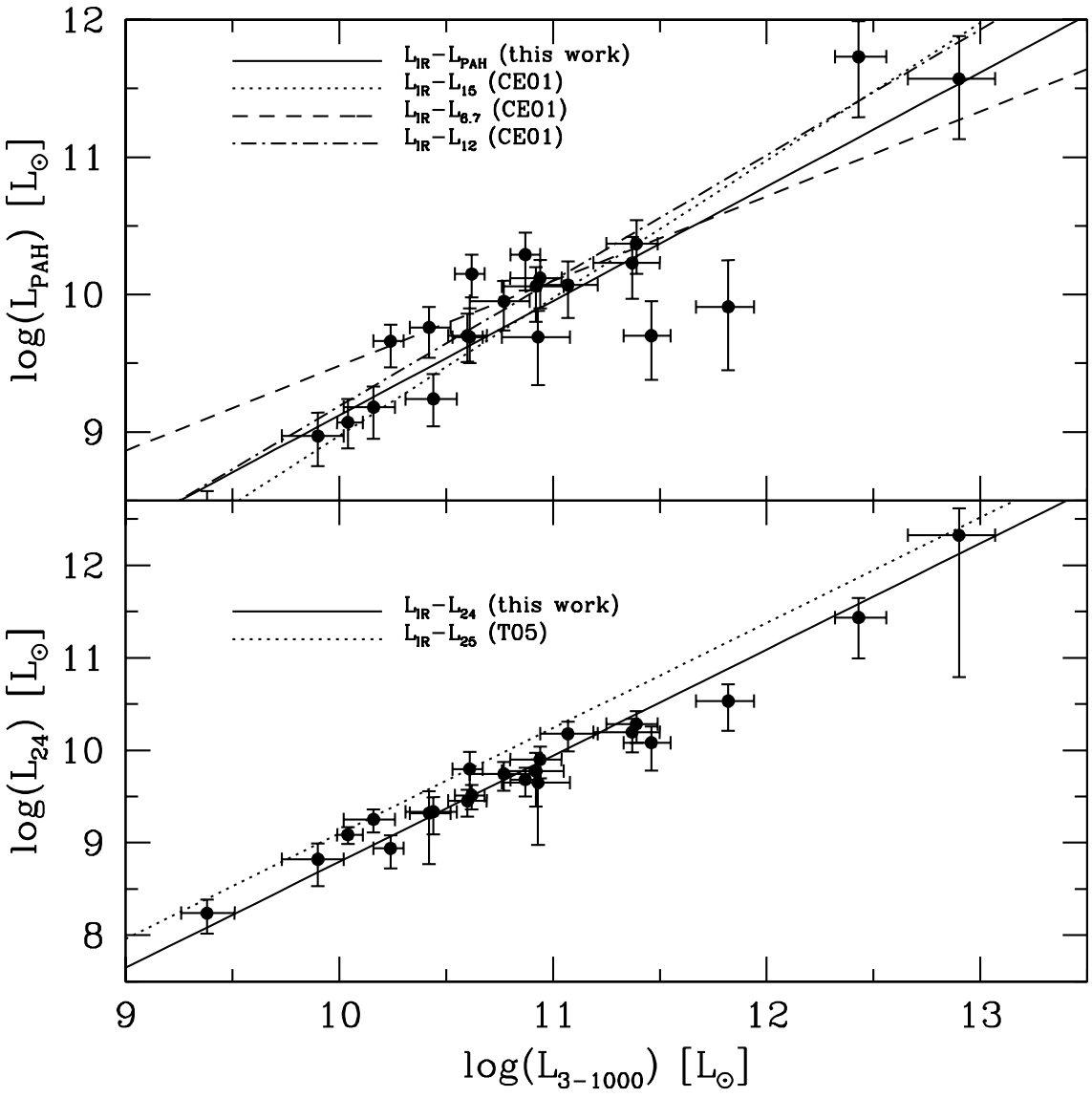

Fig. 4.13: *Top:* Here the fraction of the infrared luminosity in PAHs is plotted against the total infrared luminosity. The two highest luminosity sources are the $z \sim 1$ N1-064, and N1-078. The two LIGs apparently below the relation are: N1-013, and N1-040. *Bottom:* The 24 μm luminosity vs. the total infrared luminosity. See text for details.

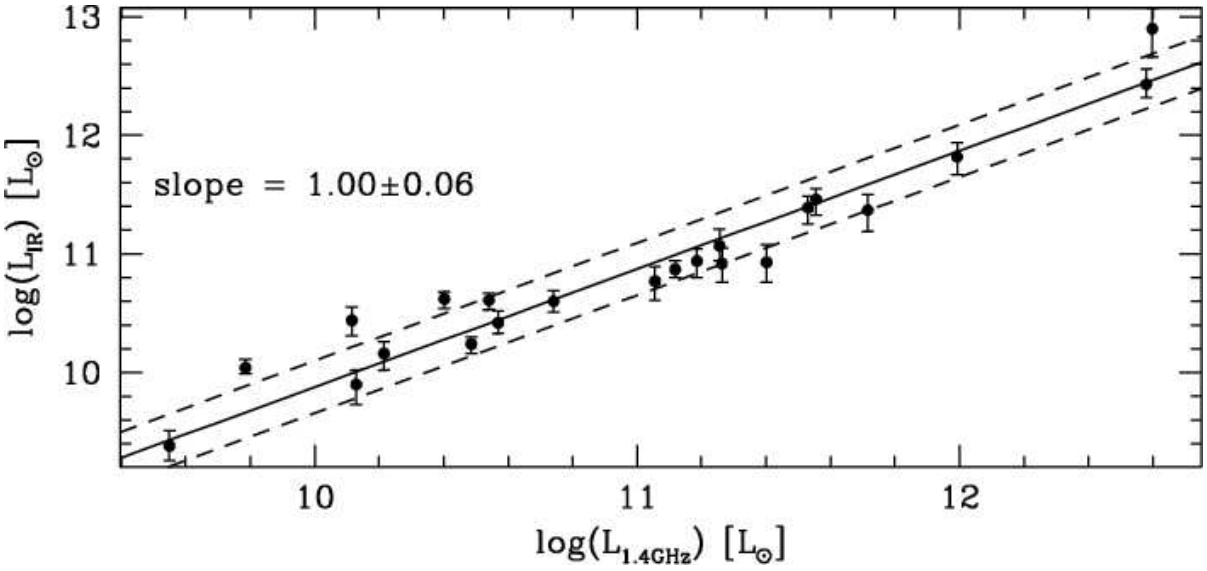

Fig. 4.14: Here the fraction of the infrared luminosity in PAHs is plotted against the total infrared luminosity. The two highest ratio points also have *IRAS* 60 μm which is in disagreement with their MIPS 70 μm thus likely $L_{\rm IR}$ should be increased by 20%, bringing them in closer agreement with the rest. The two sources with $z_{\rm spec}$ 0.4 both have slightly lower ratios than the mean of the rest. The other two 'ULIGs' here are N1-013, and N1-77 whose redshifts might be in fact lower.

traditionally L_{8-1000} is derived from the *IRAS* luminosties of the galaxies [72] and this likely differs somewhat from our L_{IR}. However, the consistency of the IR-radio correlation observed here, with the one derived from *IRAS* data (slope ~ 1, intercept ~ 0) suggest that there is no major discrepancy. Moreover, we compared our luminosities with those derived in other studies using standard templates consistent with the available and expected *IRAS* colours [99, 32]. For 11 sources with maximum coverage, we compare the infrared luminosities we find from our SED fitting approach with those obtained from the above method. We find that the two agree with each other to an rms of 0.06 dex, which is within the $1\,\sigma$ uncertainties of our estimates. Thus,

the difference in definition does not appear to bias us significantly.

About 70% of the sample have $\log(L/L_{\odot}) < 11$, while the remaining 30% have $\log(L/L_{\odot}) > 11$. This can be thought of as the break-up between fairly quiescent and more actively starforming galaxies. Throughout the rest of this Chapter, we will occasionally return to this division, while also attempting to place the quiescent/starburst classification on a firmer basis.

The use of PAH emission as a quantitative SFR indicator as well has been proposed [54, 74], based both on observations, and on theretical expectations which suggest that PAH are excited predominantly by the UV photons of young stars. This is controversial, however, as the PAH emission might in fact be more sensitive to the general ISRF (i.e. optical photons), rather than to the young stars which trace current SF [28, 65, 127]. In fact both may be true, as in richer UV environments, the UV photons could be the primary source, while in UV-poor environments astronomical PAH (which are likely to be larger and 'dirtier' than laboratory PAH molecules) might be efficiently excited by the optical photons of older stars [107]. Assuming, that the total infrared luminosity is dominated by the young/massive stars (which is apparently true although optical heating is also present [134, 136]), we can test whether, or not this is also true for the PAH luminosity, by looking for variations in the $L_{\rm PAH}/L_{\rm IR}$ ratio as a function of $L_{\rm IR}$. Within the scatter, there is no evidence that this fraction drops with increasing luminosity (see Fig. 4.13). However, as discussed above, our data does not allow us to rule such a variation out, and in fact there is at least one case (N1-040) where this is indeed observed.

4.3.3 Stellar mass and dust obscuration

As part of our SED model fitting we estimate the k-corrected, and dust corrected near-IR stellar emission. The near-IR is preferred for deriving stellar mass as it is fairly robust against

both uncertainties in the dust obscuration level (a factor of $\sim$10 less so than in the optical), and to the details of the stellar population and SFH (being largely sensitive to the red giant population only – see Fig. **??**). The transformation between the observed luminosity and the inferred stellar mass is parametrized in the mass-to-light ratio, γ, and is derived by comparing the colours of galaxies with the expectations of spectral evolutionary models [170, 52, 14]. This is now the standard approach [59, 6, 36, 64, 15] being applied to both nearby and distant galaxies. Here we use the slightly simplified form based on the near-IR only where we first calculate the un-extincted, restframe $L_{\rm K}$, and convert this to stellar mass by assuming an appropriate $\mathcal{K}$-band mass-to-light ratio, γ_K. Despite its relative insensitivity to young stars, the near-IR mass-to-light ratio does increases as the fraction of young/massive stars in the galaxy increases. In addition, a degeneracy exists in that a more massive and dustier galaxy can appear similar to a less massive and less obscured one (see e.g. Fig. **??**). The significance of this effect grows for sources without J-band data or with poor near-IR SNR, both of which are more common for the higher-z sources. For a screen geometry, the uncertainty in stellar mass is $d\log M_* = d\log\gamma + d\tau$. A mean value of $\gamma_K = 0.6$ was found by Bell & de Jong [6] for their sample of spiral galaxies, while Gil de Paz et al. [59] find γ_K to be ~ 0.92 for their sample of starburst and HII galaxies. Bell & de Jong [6] consider a wide range of reasonable population models, finding $d\log\gamma_K \sim 0.2$ dex (although this is smaller if the $\mathcal{B}-\mathcal{K}$ colour is known, due to the effect of the young stars). The luminosities we found in Section *4.3.2* suggest that our sources range between quiescent spirals, mild starbursters, and ULIGs, and therefore it is likely that the appropriate values of γ_K lie in the above range. We therefore assume the mean of the above values, or $\gamma_K = 0.78$, which assuming the Bell & de Jong uncertainty (from the unknown SFHs) of 0.2, includes the above range of possible mass-to-light ratios. For our typical sources,

$d\tau_V$ is ~ 2, which leads to $d\tau_K$ comparable to $d\log\gamma$ for any reasonable extinction law. The uncertainty in τ is already included in our quoted stellar mass uncertainties, since extinction is a parameter in the model. Consequently, the uncertainties in τ_V are roughly $10\times$ that in the stellar masses (in accordance with the typical τ_V/τ_K values). The values given in Table 4.2 do not explicitly include the uncertainty in γ, since a single stellar model is assumed and therefore an additional error of 0.2 dex should be adopted.

With the above assumptions, we find $\langle M_{\rm star}\rangle \sim 1.4\times10^{10}\,{\rm M}_\odot$,[5] where the $\log(L/L_\odot)<11$ sources and those with $\log(L/L_\odot)>11$ differ by ~ 0.6 dex. Note, however, that from the above discussion we expect that somewhat higher values for γ are appropriate for the more luminous (higher SFR) galaxies, and vice versa for the lower luminosity ones. Taking this into account, the observed difference in mass is likely to be even stronger in reality. We return to this point in Section *4.4*.

We find modest levels of dust extinction ($0<\tau_V<5$, peaking at ~ 3) for most sources. This assumes a screen geometry, and would increase in a uniform mixture of dust and stars. This result, for the bulk of the FIRBACK N1 galaxies, is consistent with the average $A_V\sim 3$[6] found from the optical spectra of the FIRBACK-South galaxies [123]. This generally increases for $z\gtrsim 0.3$ sources, with N1-040 requiring the greatest optical depth, consistent with its near-IR faintness (note however that the mean-likelihood and MCMC approaches disagree on the optical depths of the high-z sources – see Appendix A).

In the previous section, we found that the SFRs for our sample are fairly modest, typically $1-5\,{\rm M}_\odot{\rm yr}^{-1}$. We would like to address the question of whether our galaxies appear to be

[5]For comparison, typical M^* values are $\sim 3\times10^{10}\,{\rm M}_\odot$.

[6]The extinction in magnitude, A_λ is related to the e-folding extinction in flux, or the optical depth, τ_λ as $A_\lambda = 1.086\tau_\lambda$.

undergoing a star-burst, or are in a quiescent phase. There is no single absolute definition of a star-burst, but some commonly used incidators [71] include: a low ratio of the gas depletion timescale to the dynamical timescale; a high intensity of star-formation; or a high birthrate parameter (SFR/$\langle$SFR$\rangle$). The first indicator is intuitively the most robust, but is often difficult to estimate in practice (see Section *4.3.6*). The second is complicated by the need to know the size of the star-burst region, which is not necessarily the size of the galaxy (see Section *4.3.5*). The last is made ambiguous by the dependence on the epoch of the observation.

Here we examine a related quantity, the specific SFR [59], which is equivalent to the birthrate assuming a uniform epoch. The best way to interpret this is through comparison with other samples whose properties are already known. To that purpose, we use the compilation of Gil de Paz et al. [59]. However, such comparisons should be carried out with some caution, since the samples are selected in very different ways and their quoted SFRs are based on different indicators. The main distinction here is that these other samples are based on the strength of the Hα emission line, while ours are based on the overall IR emission. The two are comparable, but not identical (largely due to the effects of dust extinction on the line strength at the high-L end and possible contribution of older stars to the IR emission at low luminosities). Here we use the empirical relation of Kewley et al. [91] to convert our IR-based SFRs to $H\alpha$-based ones. Lastly, we standardize to the Kennicutt relation [88]. In Fig. 4.15, we plot stellar mass vs. specific SFR for our sample. For comparison we overplot the data for local normal spirals, strong Hα emitters, and HII dwarfs taken from Gil de Paz et al. (see [59], and references therein). In the units used, $\log(\text{specific SFR}) \sim \mathcal{O}(1)$ is taken to divide star-bursts from quiescent galaxies.

Fig. 4.15 suggests that, overall, our sample is somewhat less massive and more active than

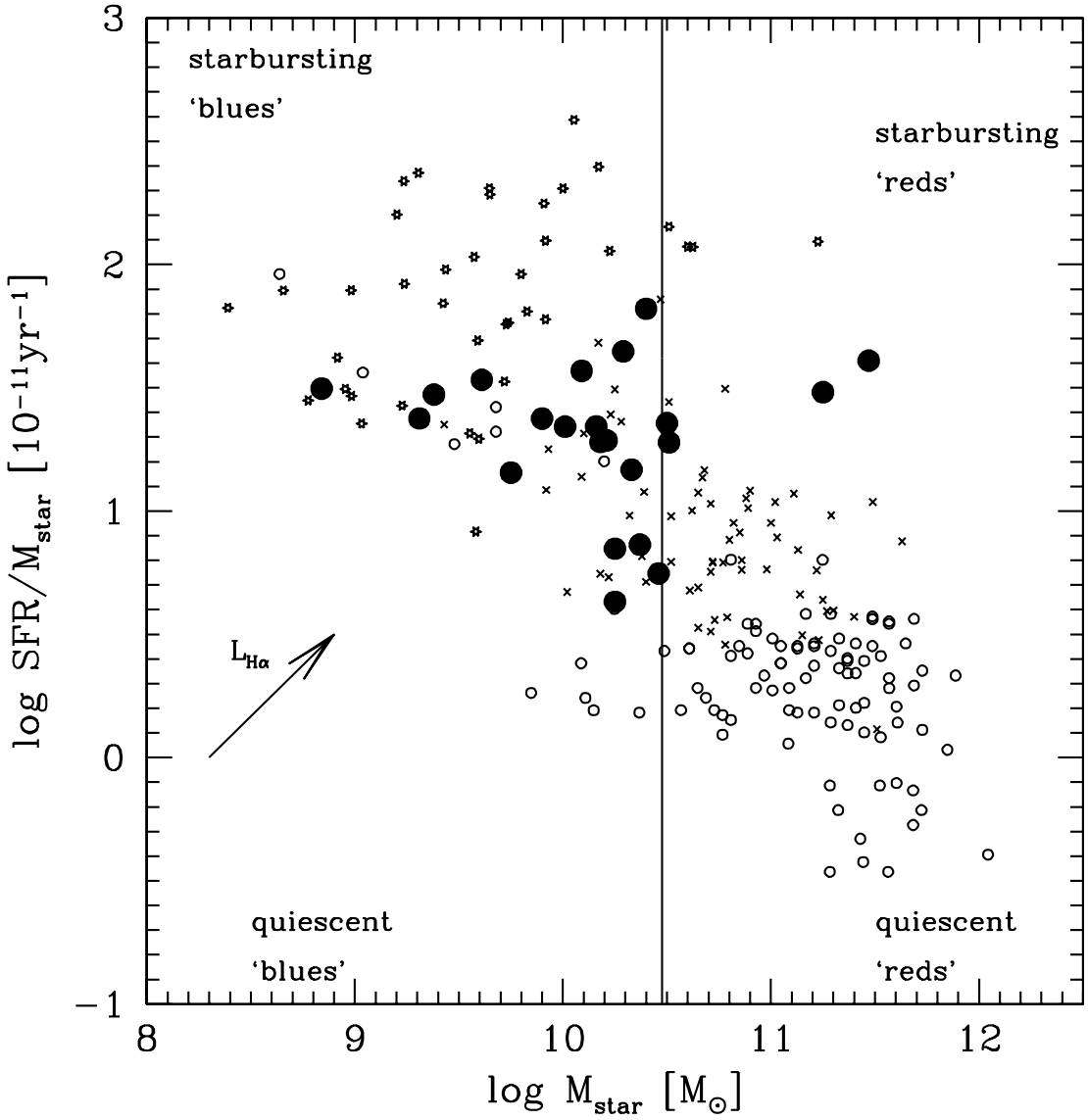

Fig. 4.15: Stellar mass vs. specific SFR. This compilation of comparison galaxies is from Gil de Paz et al. (see [59] for more discussion and full references); however we have converted their SFRs to the standard Kennicutt et al. relation [88] (a difference of –0.87 dex). Shown are: normal spirals (*open circles*); local Hα-selected star-forming galaxies (*crosses*); dwarf/HII galaxies (*stars*). Our FIRBACK sample is shown as the filled circles. Note that for consistency, we have converted our IR-based SFR to Hα-based SFR using the Kewley et al. [91] relation. The arrow shows the direction of increasing Hα luminosity from Gil de Paz et al. [59]. The mass boundary (shown by the vertical line) is the observed boundary in physical properties seen in the SDSS

typical local spiral galaxies. However, the bulk are larger and less star-bursty than the average local HII dwarf. In fact they resemble most strongly the comparison sample of Hα-selected local star-forming galaxies (from the UCM survey – [59]). The two outliers are the two ULIGs N1-064, and N1-078 which are predictably both massive and active.

4.3.4 Dust properties: $T-\beta$ relation and dust mass

The single greybody approach we take (see Section *4.2*) in modelling the dust emission of these galaxies, although in common use and the only one possible when only a few data points are available, is clearly only an approximation (see also [44, 8]). More realistically, a distribution of dust grain characteristics, such as optical properties and geometry, results in a distribution of effective temperatures and β's. In addition, degeneracies arise in fitting this model due to the functional form and spectral sampling (see Section *4.2.1* for further discussion).

For our sample, values of $T_{\rm d} \simeq 20-30\,{\rm K}$ and high values of β ($\simeq 2$) are most representative. These are in good agreement with the typical far-IR temperatures ($\sim 22\,{\rm K}$) of local spiral and irregular galaxies [28, 165] (for comparison the canonical value for ULIGs is $\sim 50\,{\rm K}$), as well as theoretical expectations which place the big grain emission (dominating the thermal peak of normal galaxies) of a standard ISM at $T_d\,15-30\,{\rm K}$ with $\beta \sim 2$ [40]. Our estimates are also consistent with but somewhat cooler than the values found by Taylor et al. [169] for the FIRBACK galaxies in ELAIS-N2. Recall that when fitting each source, there is an inverse correlation between $T_{\rm d}$ and β, the origin of which degeneracy is discussed in Section *4.2.1* and shown in Fig. *4.3.4*. This degeneracy is empirically well known [8]. Apart from this degeneracy arising from the functional form used, there has also been suggestions that a physical inverse relationship exists as well. In particular, this was seen when the best-fit temperature and

β values for different Milky Way environments were compared by Dupac et al. [46]. The relative homogeneity of our sample does not allow us to firmly support or reject this relationship (although the apparently warmest source, N1-078, supports it). A wider range of galaxy types with well sampled SEDs would be needed to address this firmly. However, we note that, as discussed in Section *4.2.1*, as the peak of the SED shifts the combined β, T distribution moves as well. But in the Dupac et al. sample the shortest wavelength is $100\,\mu$m, thus whenever the peak is shortward of that (corresponding to $\sim 30\,$K for $\beta \sim 2$), the sub-mm index begins to dominate the fit, flattening the distribution. At the other extreme for example, as the peak reaches the coldest observed values (corresponding to peaks at $\sim 200\,\mu$m), we are sampling a distirbution where $T \sim 15$ for $\beta \sim 2$ (see Fig. *4.2.1*). Therefore, it appears that this correlation is easily explained as a sequence of progressively colder/hotter environments. However, the claimed $\beta - T$ correlation is unlikely to have any physical significance. Our investigation suggests that it is merely a combination of the intrinsic correlation between $T_{\rm d}$ and β for individual sources and limited wavelength coverage.

The cold dust mass is estimated in the usual way: $M_{\rm d} = S_{850} * D_L^2[(1+z)\kappa B(T,\nu_e)]^{-1}$ [50], where $B(T,\nu_e)$ is the Planck function for the given temperature, at the emission frequency, and the dust absorption coefficient κ parameterizes the unknown grain properties. We assume the value of κ=$0.077 \pm 0.02\,{\rm m^2 kg^{-1}}$ as advocated by James et al. [81], although there are arguments for a value up to 3 times higher [30]. We return to the effect of κ below. We find $M_{\rm d} \sim 10^7$–$10^8\,M_\odot$, which is comparable with the masses found by Dunne et al. [44] for the SCUBA Local Universe Galaxies Survey (SLUGS) galaxies. As expected, the higher z, more luminous galaxies have higher dust masses, typically $\sim 10^8 - 10^9\,{\rm M_\odot}$.

We now have two independent measures of the dust content (using absorption and emission).

Above we derived the dust mass based on the far-IR emission of our galaxies. In principle, the optical depth derived in the previous section can also be converted to dust mass, provided the surface area of the optical region is known. We do this using the following equation, adapted from [109] by using $\tau_B = 1.3\,\tau_V$ and assuming the geometry is an inclined disk:

$$M_{\rm d}^{\rm opt} = (1.1 \times 10^5)\tau_V R^2 {\rm cosi}, \tag{4.10}$$

where i is the the inclination, such that 0° is face-on and 90° is edge-on.

In anticipation of the next section, here we will use the effective radii of our sources. In Fig. 4.17, we compare this optically derived dust mass and the IR-derived dust masses. The two clearly correlate, as expected. However, the best-fit slope is 0.86 unlike the expected 1.00. The arrows define the directions in which either increasing disk inclination or increasing κ push the points. Note that increasing inclination is equivalent to decreasing the size of the region contributing the bulk of the IR emission (s.a. a nuclear starburst). Therefore at the high-mass end, the good agreement suggests that the dust (behind the IR emission in particular) is distributed throughout the entire disk rather than being a nuclear starburst (see next section). Somewhat constradictory, the high values of τ_V we find are also fully consistent (but the lower values implied by the likelihood analysis are not – see Appendix A). The two can be reconciled by a more complex geometry. At the low mass end we find consistently higher dust masses than expected from the above formula and the derived optical depths (hence the shallower slope). This may merely indicate that the highest-SFR regions responsible for the dust emission, are behind a foreground screen of much less obscured older stars responsible for the near-IR emission. Another interpretation, is that our IR-based dust mass is overestimated. If we adopt the extreme end of κ values in the literature [30], $\kappa \sim 0.2$, will decrease our estimates by about 0.4 dex. The two are much more consistent now. The inclination cannot explain this as it

only affects the points to the right of the dashed line (face-on case). This relation should not be interpreted any further than this, since both expressions are approximations to much more complex systems and seeking a perfect agreement between them is therefore unrealistic. Within the uncertainties, we are gratified that our two independent estimates of the dust content agree as well as they do.

Another relation of significance we can now address is the $L-T_{\rm d}$ relation (see e.g. [8]). This relation is of particular significance to far-IR/sub-mm selected samples, as in principle it can reveal something of the nature of the sources based on only a few spectral points (enough, to for example, for a single greybody fit), because it is simply a relation between the location of the far-IR peak and its overall strength. We can compare the location of our sample in the (L, $T_{\rm d}$) plane with other infrared-selected samples, namely the SCUBA-selected high-z sources [21] and the bright *IRAS*-selected galaxies [44]. The general trends can be understood simply by recalling that $L \propto R^2 T^4$. This leads to luminosity increasing with temperature if the size is kept constant, or conversely to a more concentrated starburst being hotter than a galaxy of the same luminosity but with more spread-out (as in throughout the full disk) star-formation. Empirically, it is found that $T_{\rm d} \propto L^K$ where the parameters vary with source type [4]. In Fig. 4.18 we overplot the relations appropriate for merging and quiescent galaxies [4]. With a few exceptions, our sample is consistent (within the uncertainties, and given the different selection from that of *IRAS* galaxies) with the relation for quiescent galaxies (for further discussion of the relation see [20]).

4.3.5 Size and morphology

The closest galaxies in our sample appear disk-like by visual inspection of the IRAC images (see Fig. 4.1). In addition, we would like to determine the typical sizes of our sample, and whether there is a noticeable morphological difference as a function of infrared activity (i.e. $L_{\rm IR}$). Fortunately, all 22 sources considered here are at least mildly resolved by IRAC (diffraction limit $\sim 2''$ at $8\,\mu$m). The effective radii given in Table 4.2 are the $8\,\mu$m half-light radii converted to physical distance[7] (note there is no noticeable difference here if we used any other IRAC band). We find that, typically, $R_{\rm eff} \sim 5-10\,$kpc, although a tail of the sample extends to larger radii. These sizes are consistent with those of large spirals (c.f. $\sim 4\,$kpc for the Milky Way, $\sim 50\,$kpc for Malin 1).

However, as mentioned previously, it is possible that some of our sources (especially among the higher-L ones) are primarily powered by nuclear starbursts, and that the above sizes are in fact appropriate to an extended dust disk instead (which also leads back to the question of what powers the PAH emission – see Section *4.3.2*). In Fig. 4.18, a few sources (N1-016, N1-064, and the more extreme N1-078) have higher temperatures per luminosity than most galaxies, arguing for such concentrated starbursts. We can determine the actual sizes of the star-forming regions in our galaxies by using the well known relation between gas surface density and SFR surface density (the Schmidt law, [154]). Observationally (the Kennicutt relation [87]), it has been shown that over many orders of magnitude the SFR density scales with the gas density of the galaxy, arguing that the efficiency of star-formation is a universal constant. The slope of the relation $\mathrm{SFR} \propto \rho^n$ is $n = 1.4$ [87]. However, the dependence of both quantities on radius is

[7] This is simply: $\mathrm{R} = \theta D_A$, where D_A is the angular diametr distance related to the previously discussed D_L via $D_A = D_L(1+z)^{-2}$ [17], and θ is the angular half-light radius of the galaxy.

the same ($\propto 1/r^2$), meaning that a change in the effective radius takes the form of a translation along a line of slope $n = 1.0$. Thus, assuming that the efficiency of star-formation is indeed universal, any departure from the Kennicutt relation should be attributed to a difference in effective radius.

We estimate the gas mass by assuming the Milky Way gas-to-dust ratio of 100 [93], although the values for extenal galaxies especially show a large spread of about an order of magnitude (see e.g [165]). With these estimates, in Fig. 4.19, we overplot our sample onto the original Kennicutt sample of normal spirals, and IR-bright starbursts. Most galaxies lie exactly on this relation somewhat above the spirals consistent with Fig. 4.15. This suggests that the bulk of our sample is indeed forming stars throughout their extended disk, although slightly more actively (due to more gas-rich disks) than local spirals. Note, however, that this might largely be an effect of the redshift of these galaxies. Given their typical redshift of $\simeq 0.06$, our galaxies are observed about 0.5 Gyr in the past. Assuming a typical SFR of $\sim 5\,\mathrm{M_\odot\,yr^{-1}}$, leads to about $2 \sim 10^9\,\mathrm{M_\odot}$ of stars being created (or gas being depleted) over this timescale, which is still not enough to overlap with the average for local spirals (either in Fig. 4.15, or Fig 4.19), suggesting that the typical spirals of today formed the bulk of their stars earlier than for the FIRBACK galaxies (which are slightly less massive). This is consistent with the idea of 'downsizing' whereby the star-formation activity on average shifts to progressively smaller systems (e.g. [84]).

In Fig. 4.19, we also distinguish between the low-L and high-L galaxies, but find that the difference is not dramatic, although the latter are clearly more 'active'. The only true outliers are N1-064, and N1-078 which are our highest redshift sources and are classified as ULIGs. N1-078 is somewhat to the left of the relation and thus might harbour a more concentrated starburst; however, the scatter in the relation makes this uncertain. Therefore, for the entire

sample, the good agreement between our sample and the Kennicutt relation suggests that both the radii and the assumed standard dust-to-gas ratio are likely close to the truth. The inset in Fig. 4.19 gives the size distribution of the sample, which is consistent with that of local spiral galaxies [175]. An *HST*-based study of the size distributions of slightly higher redshift ($z \sim 0.2-1$) disk galaxies suggested suggested effective radii in the same range and peaking at $\sim 6\,$kpc to $\sim 4\,$kpc as the redshift decreases [141].

Locally, ULIGs are almost always associated with major mergers that clearly disturb the disk morphology of the merging clumps [174]. The induced star-formation activity is typically concentrated in the central few kpc of the galaxy. However, there is no compelling evidence that this is the case for our ULIGs (also supported by their unusually cold colours). The physical difference (rather than merely in scale) between LIGs and ULIGs was already discussed in Chapter 1, therefore the large sizes for our LIGs is not a surprise.

As a final test, we double check the above conclusions by looking at the relation between $L_{\rm IR}$ and $T^{4+\beta}R^2$. As expected we find a good correlation between the two. The linear fit gives:

$$\log L = (0.9 \pm 0.1) \times \log(T^{4+\beta}R^2) + (1.5 \pm 1.3), \tag{4.11}$$

where L is in $L_\odot$, T is in K, and R is in kpc. There are no obvious outliers (the rms is 0.4), suggesting that given the cold temperatures derived, the radii inferred from the $8\,\mu$m images are appropriate (to within a factor of 2).

4.3.6 Starbursts? Its about timescales

In the previous sections, we looked at various combinations of our fitted parameters compared with other samples. The principle goal of this exercise was to gain insight into the physical properties of the FIRBACK galaxies and how they compare with other galaxy populations. A

key question here is whether they can be considered to be undergoing starbursts or not. Some representations show them to be borderline starbursts (specific SFR, Schmidt law), while others suggest more quiescent systems ($L-T_{\rm d}$ relation). As discussed in Section *4.3.3*, the principle quantity determining whether a galaxy should be considered to be a starburst is the ratio of the gas depletion timescale ($\tau_{\rm depl}$) to the dynamical timescale ($\tau_{\rm dyn}$) of a galaxy. The idea is that if the current rate of SFR is such that if sustained the available gas reservoir will be exhausted in a time shorter than the dynamical time, then the source is bursting.

We are now in a position to estimate this for our sample. The depletion timescale is simply $M_{\rm gas}$/SFR. Here, the SFRs are estimated from the total IR emission (Section *4.3.2*), while the gas mass is derived from the dust mass and an assumed dust-to-gas ratio (Section *4.3.5*). Using these estimates, we find that, typically, $\tau_{\rm depl} \sim 8\times 10^8\,{\rm yr}$. The dynamical time is defined as $\tau_{\rm dyn} \sim (R/GM_{\rm tot})^{1/2}$. To estimate this, we begin by ignoring the dark matter contribution, and calculate the dynamical time using the gas mass. We then note that including any dark matter contribution would only have the effect of decreasing $\tau_{\rm dyn}$ and thus any source that appears quiescent will remain so regardless of the extra mass (we return to this point below). Using this approach we find that typically $\tau_{\rm dyn} \sim 1\times 10^8\,{\rm yr}$. When the dark matter halo mass is included[8], the only starbursts in our sample are N1-013, and N1-078 (with N1-064, and N1-077 being borderline). Note, however, that the question of the size of the effective starburst region is relevant here as well. This might be affecting the LIGs N1-015 and N1-039, which surprisingly do not appear to be starbursts by this criterion. Overall, the bulk of our sample, despite their being apparently somewhat more active than normal spirals, do not appear to be bona fide star-bursts.

[8]Using the relation $M_{\rm halo}/M_{\rm gas} \approx 34.7(M_{\rm gas}/10^7 M_\odot)^{-0.29}$ [113, 129]

4.4 Discussion

In this Chapter, we have presented a comprehensive study of the full infrared SEDs of a sample of 22 FIRBACK galaxies. Our new multi-component model together with the MCMC fitting technique have allowed us to test various previous assumptions about FIRBACK galaxies, as well as the spectral templates used to model them and related populations. In Fig. 4.21, we summarize our results for the derived physical parameters by plotting their distributions separately for quiescent ($\log(L/L_{\odot}) < 11$) and active ($\log(L/L_{\odot}) > 11$) galaxies. On the whole we find that the latter are larger, warmer, dustier, and generally more massive than their less luminous counterparts.

One of the primary questions we wanted to answer with this study was the nature of these galaxies. Initially from the sub-mm data [150] and later through optical spectrosocopy follow-up [32], it was already known that in their majority these galaxies are not the $z \sim 1$ ULIGs that early models predicted for the FIRBACK survey [98]. Beyond that however, little has been known of their nature, and in particular their masses, sizes, and moded of star-formation have been poorly constrained up until now. Here we have addressed these issues from a number of (admittedly not always independent) perspectives and concluded that the sample is consistent with $\sim M^*$ mass galaxies, which are forming stars somewhat more actively than local spirals, but are likely not actually starbursting according to the usual definition. Their mode of star-formation is consistent with slightly enhanced activity in the disk, rather than the nuclear bursts associated with major mergers. Their cool colours also exclude any significant contribution from AGN activity. A study of the ELAIS-N2 FIRBACK galaxies by Taylor et al. [169] used a set of theoretical templates for cirrus (i.e. quiescent), starburst, and AGN galaxies. They conclude that 80% of the FIRBACK sources are star-bursts (with a few ULIGs proportionately to our

sample), while 20% are cirrus galaxies. Given the flexible definition of 'starburst', we find that our conclusions are consistent.

As discussed in Chapter 1, recent studies, both theoretical and observational, have found that the strong increase in SFR toward $z \sim 1$ [108, 76] is most likely due to an increase in the average SFR in spiral galaxies (possibly caused by minor mergers with satellites) rather than the extreme star-formation events resulting from major mergers, which probably dominate at higher-z's (e.g. SCUBA sources at $z \sim 2$ [21]). As this picture is strongly reminiscent of our sample, as found in this thesis, we would like to explicitly address the following questions: how common are FIRBACK-like galaxies; and what is their contribution to the SFR density of the Universe?

4.4.1 Contribution to the L* luminosity density of the Universe

In this chapter we found that the FIRBACK galaxies emit less in the mid-IR than previously expected. We speculated that this is due to selection effects, such as for example *IRAS* being biased toward sources that are more mid-IR bright than typical. In fact, right from the start it was clear that *IRAS* is missing the majority of L^*[9] galaxies [152], when compared with optical surveys such as the SDSS [10], and this could be due to just such a difference in the SEDs.

For comparison with the *IRAS* luminosity function, we begin by selecting only the $z < 0.1$ sources in our sample. This leaves us with 11 sources. Assuming that our sample is representative of the FIRBACK survey as a whole, this represents $10-30\%$ (depending on the nature of the non-unique identifications) of the number density for the whole survey. Next we compute a

[9]This is the knee of the luminosity function in the Schecter parameterization where $\phi = \phi_o (L/L^*)^\alpha e^{-L/L^*}$ and ϕ is the number density.

comoving volume[10] out to $z = 0.1$ (for appropriate comparison with the *IRAS* and SDSS luminosity functions). The average luminosity for these low-z sources is $\log(L/L_{\odot}) = 10.3$ and their number density, $\log \phi$, is –2.0 to –2.5 [dn/dlogL/Mpc^3/ster] based on the above range. Note that, Dole et al. [37] find that the $4\,\sigma$ FIRBACK catalogue ($\equiv 180$ mJy) is only 85% complete. In general, we have used the $3\,\sigma$ catalogue ($\equiv 135$ mJy) as well, but the above redshift cut effectively selects only the $4\,\sigma$ sources. Correcting for this incompleteness brings the numbers up slightly, but insignificantly compared with the uncertainty caused by the unidentified sources.

In Fig. 4.22, we reproduce the *IRAS* results by comparing the *IRAS* luminosity function [160, 152], with the $z < 0.1$ normal galaxies luminosity function [10]. Note that this comparison has several caveats, since by $L_{\rm bol}$ we mean $infrared$ in one case and *optical* in the other. However, for the average galaxy these are roughly comparable and thus on the log scale shown the effect would not be very noticeable (see also [160]). On top of this we plot our estimates for the FIRBACK galaxies. Clearly, the density of $\sim L^*$ FIRBACK galaxies is higher than the density of the correspondingly luminous *IRAS* sources. It appears that FIRBACK is picking out the bulk of the local L^* population. A consequence of this is that the rest of the CIB (i.e. the lower flux 170 μm sources) comes mainly from galaxies at higher redshifts, rather than just lower luminosity galaxies.

4.4.2 Contribution to the SFR density in the Universe

Assuming that our sample of 22 sources is unbiased with respect to the entire FIRBACK survey, we can use the redshifts and SFRs derived in this Chapter to estimate the contribution

[10]The comoving volume out to some redshift z and within a solid angle $d\Omega$ is simply $V d\Omega = (D_M^3/3) d\Omega$ [17], where D_M is the proper distance related to D_L by $D_M = D_L/(1+z)$, and $d\Omega$ is the sky coverage of the survey in steradians.

of FIRBACK galaxies (i.e. far-IR bright sources) to the Universal star-formation rate density otherwise known as SFRD or $\dot{\rho}$. The previous section leads us to expect that at low-z we see most of the SFRD, while at high-z we should only see a fraction (since our flux-limited survey selects only the highest luminosity sources at redshifts $z \gg 0$).

We start by defininining two redshift bins: at low-z ($z = 0.075 \pm 0.075$), and high-z ($z = 0.53 \pm 0.38$), which essentially divides the $\log(L/L_{\odot}) < 11$ and $\log(L/L_{\odot}) > 11$ sources. As before, we assume that our sample represents $\sim 10-30\%$ of FIRBACK as a whole. Now we sum the SFR of all sources in each redshift bin and divide by the volume element sampled at the given redshift[11]. Given that the area of the ELAIS-N1 FIRBACK survey is 1.98 sq.deg., we obtain $\log(\dot{\rho}) = -1.7$ to $-2.2\, M_{\odot}\mathrm{yr}^{-1}\mathrm{Mpc}^{-3}$ for the low-z bin and $\log(\dot{\rho}) = -2.4$ to $-2.8\, M_{\odot}\mathrm{yr}^{-1}\mathrm{Mpc}^{-3}$ for the high-z bin depending on the range. The high-end of the low-z estimate is consistent with seeing all the SFR locally (given the scatter between various estimates[76]), while the low-end underestimates it by about a factor of 3. Our $> 10^{12}\, L_{\odot}$ galaxies (ULIGs) contribute only negligibly to the SFRD of the Universe at $z \sim 0.5$ consistent with the idea that mildly starbursting spirals (such as LIGs) are responsible.

[11] Given a non-zero cosmological constant, the formula is: $dV = \frac{c}{H_0(1+z)^2} \frac{D_L^2\, dz\, d\Omega}{\sqrt{(1+z)^3\Omega_M + \Omega_\Lambda}}$ where $d\Omega$ is the sky coverage of the survey in steradians. Note that this is simply $dV/d\Omega = D_M^2 dD_M$

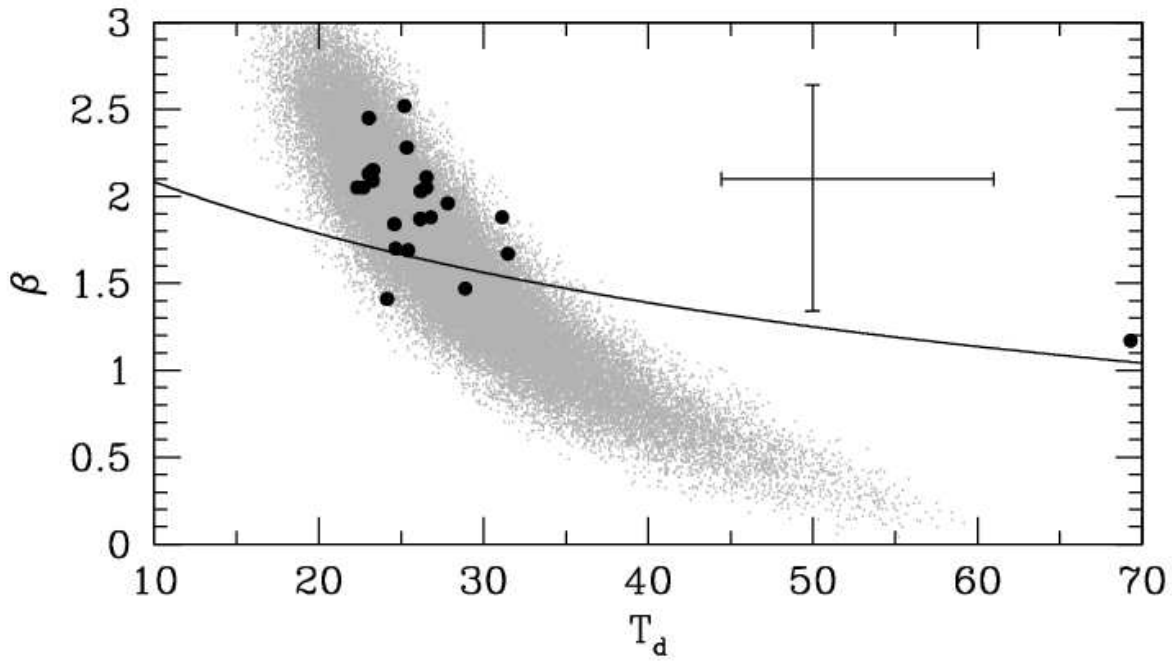

Fig. 4.16: The best fit values for $T_{\rm dust}$ and β. The solid line is the Dupac et al. [46] relation. For comparison the greyscale points show the $\chi^2_{\rm min}+3$ region for N1-024. The error bars represent the average 68% uncertainties on individual sources (note that it is driven by the least constrained sources, while the grey points give a better sense of the scatter in well constrained sources). The outlier near 70 K is N1-078, for which no data exist between 24 μm and 170 μm.

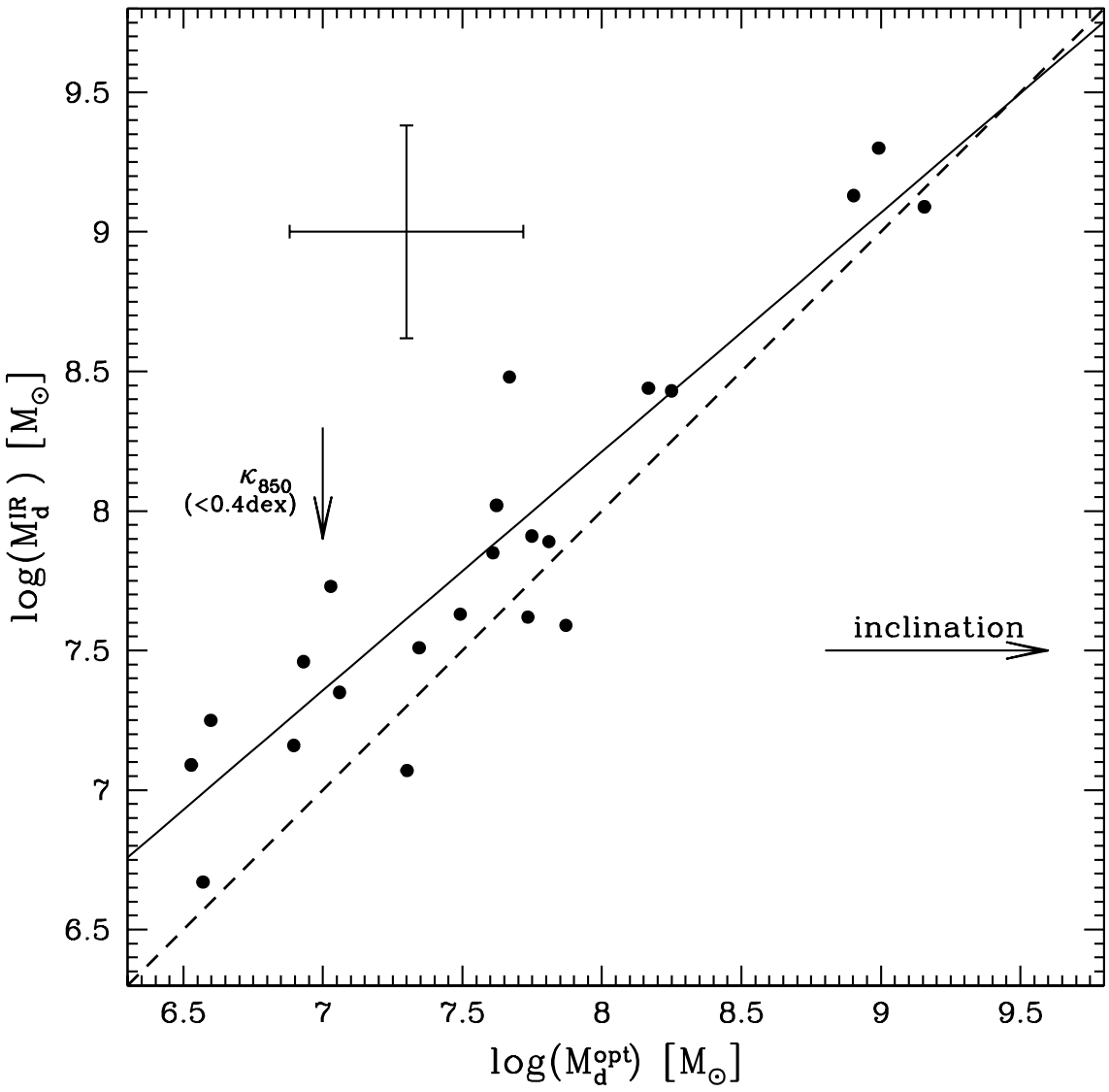

Fig. 4.17: Optically-derived dust mass compared with IR-derived values. The solid line is the best-fit, while the dashed line is the expected $y = x$ line (for face-on disks). The directions of increasing disk inclination, and κ are shown.

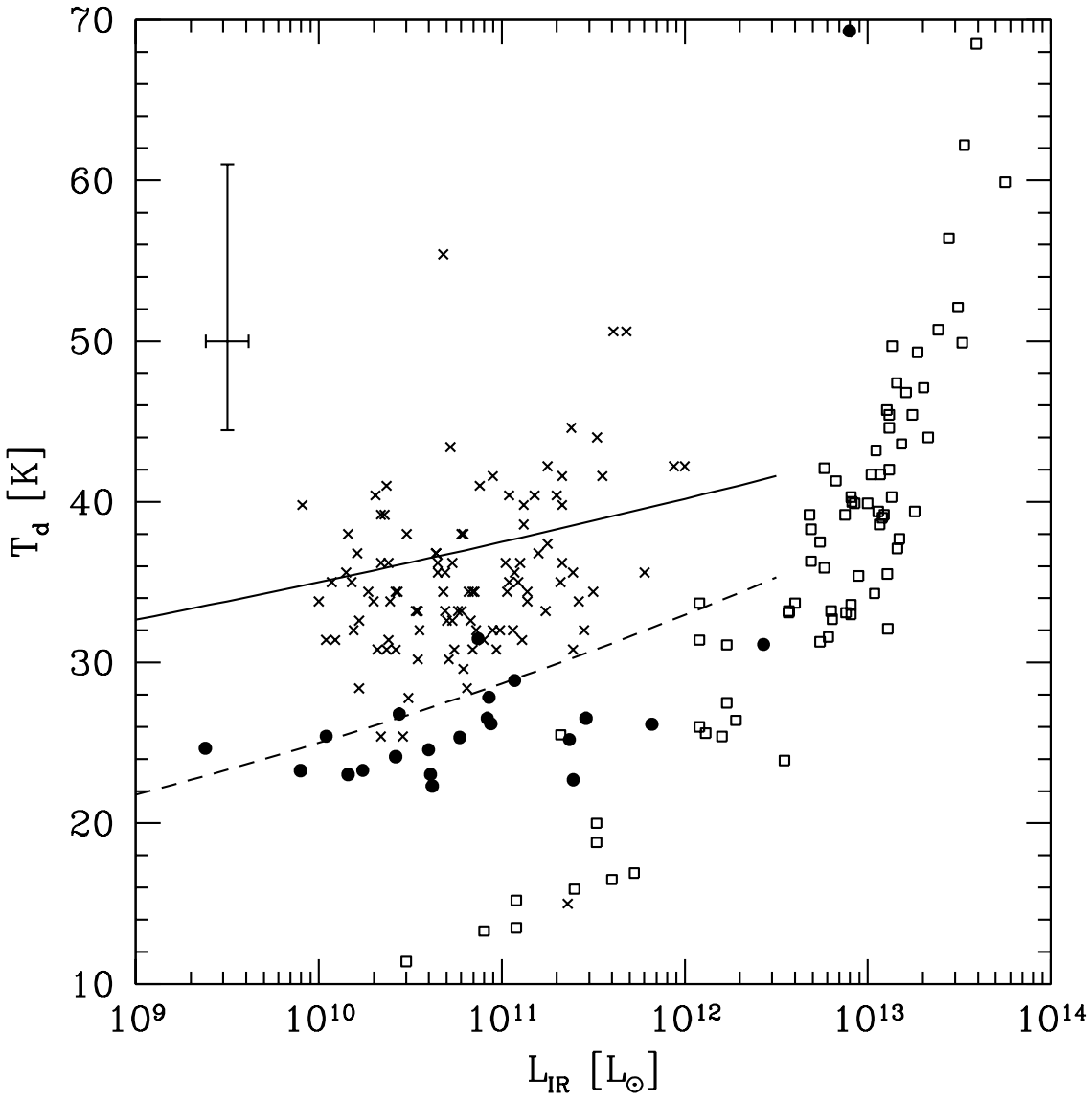

Fig. 4.18: A comparison of the luminosity-temperature relation for our sample (*solid circles*) with other infrared-selected galaxies including *IRAS*-bright galaxies [44] (*crosses*), and SCUBA-selected galaxies [21] (*open squares*). The solid and dashed lines represent merging and quiescent galaxies respectively [4]. Note that our sample is consistent with the expectation for quiescent starformers.

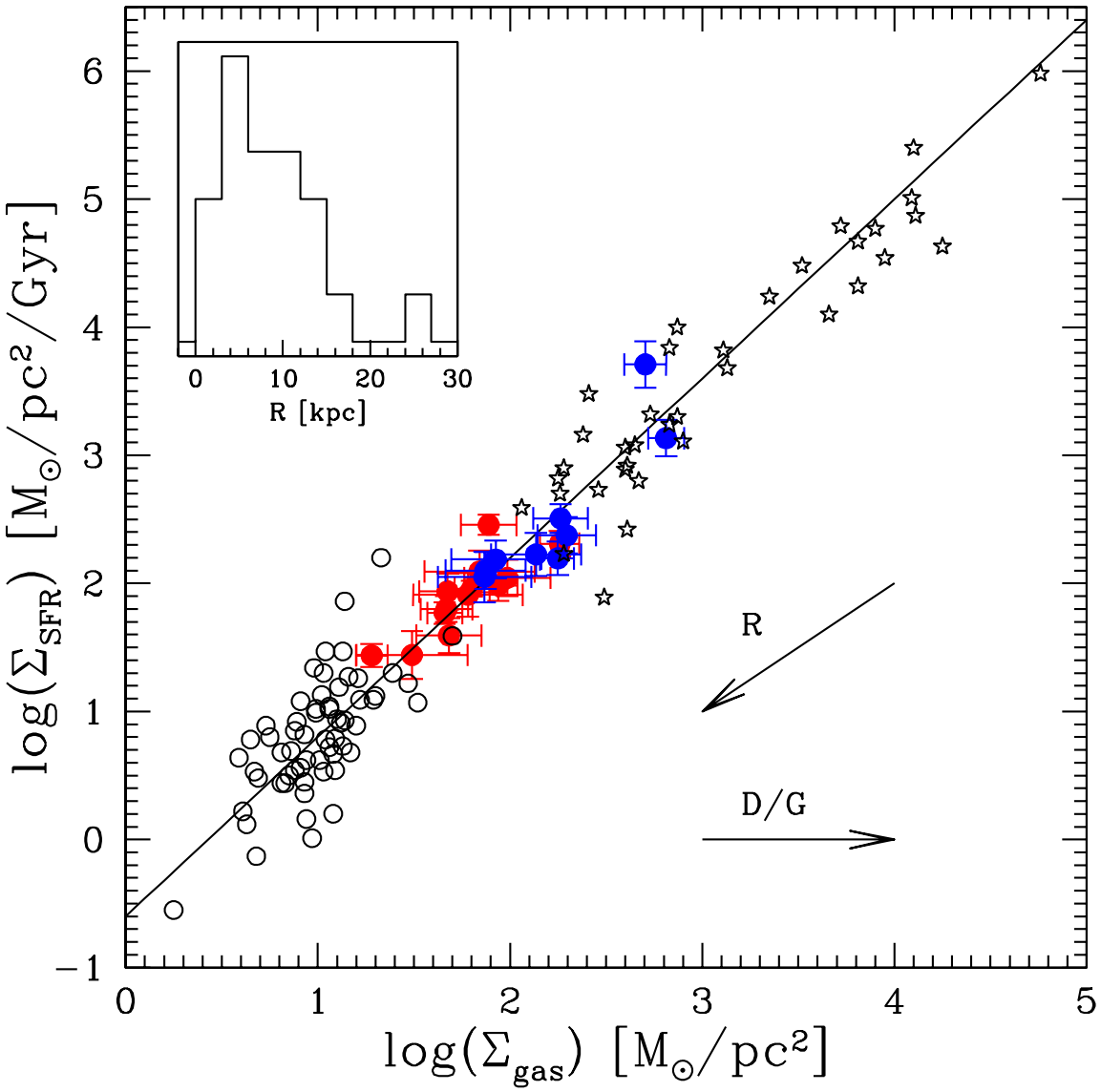

Fig. 4.19: The Schmidt law, $\Sigma_{SFR} = \alpha\,\Sigma_{gas}^{n}$, where $1 < n < 2$ for normal spiral galaxies [87]. Here the red filled symbols are our $\log(L/L_{\odot}) < 11$ galaxies while the blue symbols are the $\log(L/L_{\odot}) > 11$ ones. Errorbars are 68% uncertainties. The solid line is the Kennicutt relation with $n = 1.4$. The inset shows the size distribution for the sample. The slope = 1 arrow shows the direction of increasing radius. the flat arrow shows the direction of increasing dust-to-gas ratio (D/G).

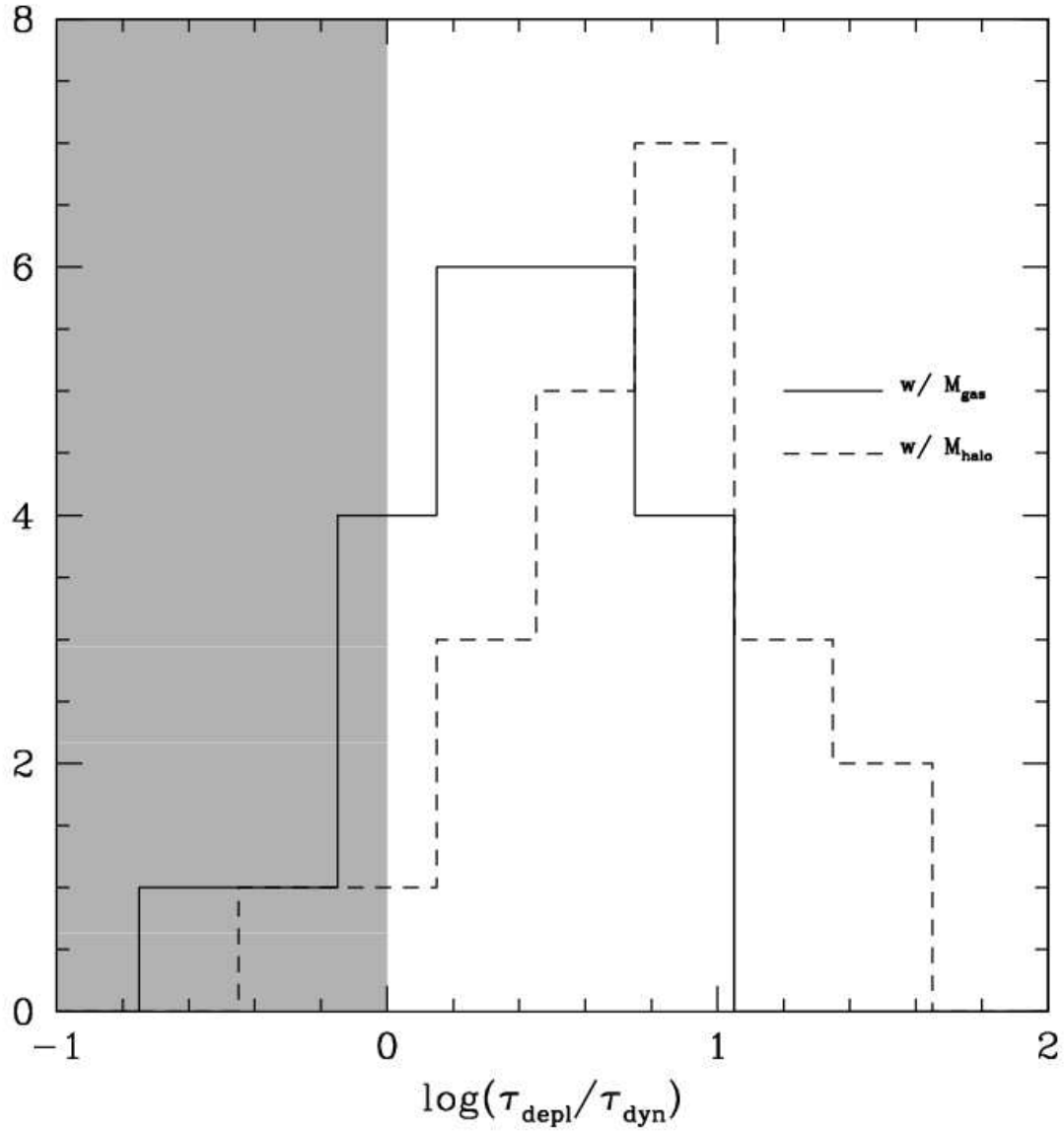

Fig. 4.20: The ratio of gas depletion vs. dynamical timescales. The two histograms are for the case where DM is not included (solid line) vs. when it is (dashed line). The shaded region corresponds to the classical definition of a starburst.

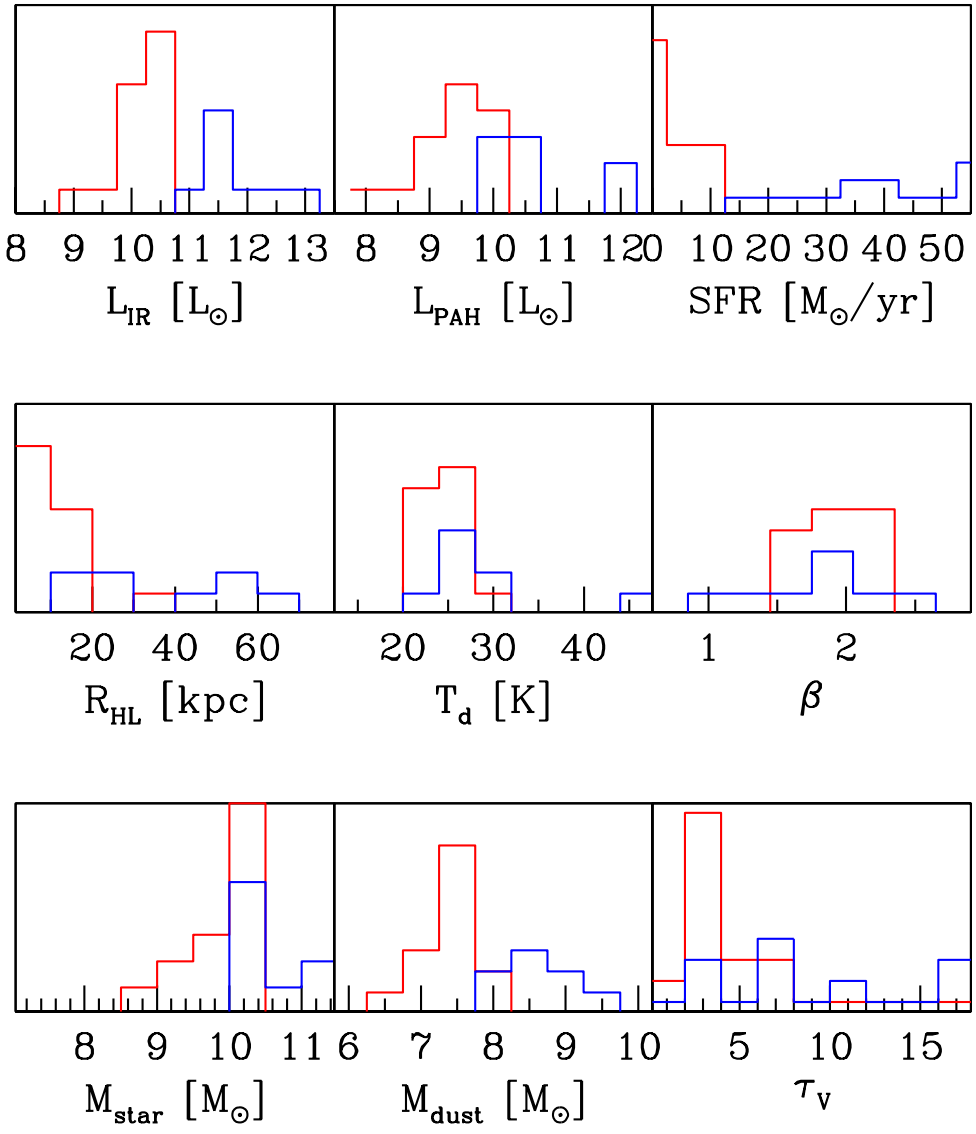

Fig. 4.21: The distributions in the physical parameters derived in Section *4.3*. Quiescent galaxies (defined as having $\log(L/L_\odot) < 11$) are in red, while more active galaxies (defined as having $\log(L/L_\odot) > 11$) are in blue. Note the higher stellar and dust masses (and by extension gas masses) for the latter.

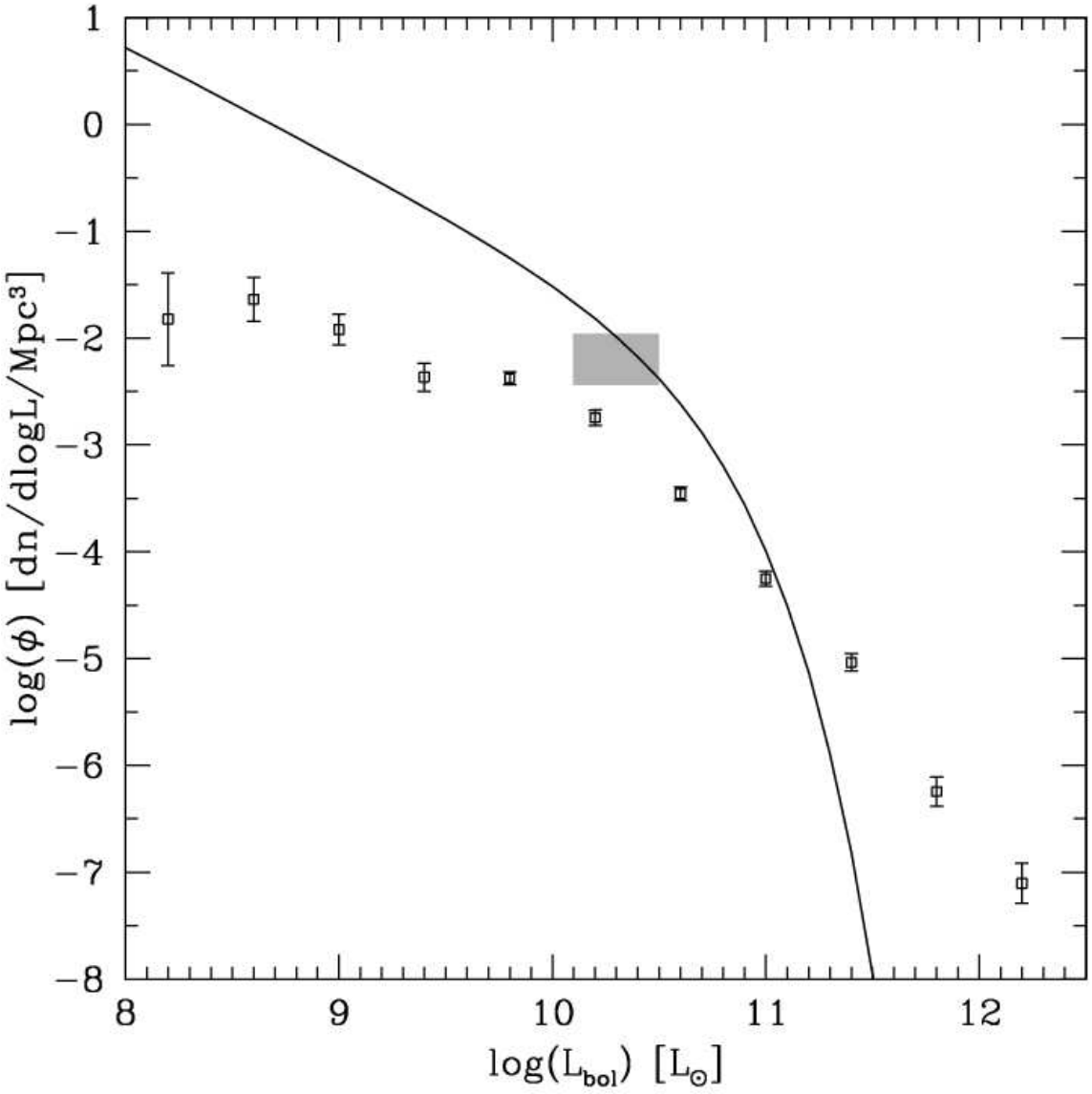

Fig. 4.22: Here we compare the luminosity density derived for our low-z sample (shaded region) with the *IRAS* luminosity function (*open squares*), and the luminosity function of local SDSS galaxies (*solid line*).

CHAPTER 5

IMPLICATIONS AND PREDICTIONS

In Chapter 1, we discussed the importance of knowing the SED shape, both when interpreting the sources detected in infrared surveys, and when constructing galaxy evolution models.

We developed these ideas in Chapter 3, where we argued that colour-colour plots hold diagnostic potential for understanding broadband survey data, which is far is largely unexplored.

In Chapter 4, we constrained a set of SEDs covering the range $\log(L/L_{\odot}) \sim 10-12$. These represent the brightest $\sim 10\%$ of the CIB contributors near to its peak. We have found them to be mainly moderately star-forming large/massive disks with relatively cold SEDs and with a small fraction of more luminous and distance sources. We would like to gauge the importance of FIRBACK-like galaxies in interpreting the data from infrared surveys – i.e. should such cold templates be included in models for the new *Spitzer* sources or the SCUBA-selected sources? And what is the nature of the remaining 90% of the far-IR CIB contributors?

In this Chapter we will further explore some of these questions, giving some illustrations of how our approach to fitting the properties of individual galaxies can be extended to study populations of sources.

5.1 The relevance of FIRBACK-like galaxies

In Section *4.4*, we found out that L^* FIRBACK galaxies are nearly an order of magnitude more common than low-luminosity *IRAS* sources. We found that FIRBACK galaxies can

account for the SFR density of the Universe at low-z and their analogues (rather than extreme star-formers) might account for the higher density of star-formation at $z \sim 1$. Here we would like to elaborate this point further through comparisons with other infrared-selected samples and with the colours of the CIB itself.

5.1.1 Implications for the faint 24 μm sources

Over the past year, *Spitzer* has revealed large numbers of faint (roughly $\sim$10–1000 μJy) 24 μm sources. There has been much speculation about their nature, with obvious implications for various galaxy evolution models. In Fig. 5.1, we evolve the SEDs of an L^* galaxy, a LIG and an ULIG from our FIRBACK sample. We compare these with the detectability thresholds of the wide and shallow SWIRE survey [166] and the deepest current *Spitzer* survey, GOODS-North [22]. The SWIRE sources are expected to be predominantly low-z, meaning that FIRBACK-like galaxies (at only slightly higher redshifts) are likely to make up a significant component of them. For the deeper GOODS survey, FIRBACK analogues are expected to be a significant component up to $z \sim 1$, while in the $z \sim 1-2$ range GOODS appears to be dominated by $11 < \log(L/L_{\odot}) < 12$ sources such as the ULIG-tail of our sample, as discussed by Chary et al. [22]. Overall, Fig. 5.1 suggests that understanding the faint 24 μm sources requires taking into account not only M82 or Arp220 type sources, but also the much less luminous and colder FIRBACK sources, especially in the crucial $z \lesssim 1.5$ regime. This is supported by the fact that while SCUBA-selected sources have close to 100% detectability in the current generation 24 μm surveys [48, 55], most of the 24 μm-selected sources do not have individual SCUBA-counterparts (stacking analyses show them to have individual 850 μm flux $\sim$0.5 mJy [156], which is below the confusion limit of SCUBA).

5.1.2 Implications for the SCUBA galaxies

Fig. 5.1 indicates that if the SCUBA galaxies are as cold as our ULIGs (and given that their redshifts are typically in the range $z \sim 2-3$) then SWIRE cannot detect any but the most luminous or the most AGN-dominated ones among them. This has implications for the *Spitzer* overlap with SCUBA galaxies in wide-field sub-mm surveys, such as SHADES [43], and those being planned with SCUBA2. The difference between the FIRBACK far-IR and blank-sky sub-mm sources is further highlighted in Fig *5.1.2*. Here we show shaded regions to indicate the colours of normal $\log L < 11$ galaxies, with $\log L > 11$,ones indicating their rough redshift evolution. Note in particular, the influence of the PAH feature complex as it traverses the $24\,\mu$m filter at $z \sim 2$. It appears that, compared with our ULIG template, the bulk of the SCUBA sources are redder in both colours. As the $24\,\mu$m flux pull them in different directions here, this rather suggests that the reddening of one colour drives the overall effect. The S_{24}/S_8 colour is reddened by redshift, optical depth, the presence of AGN, or increased PAH strength (at $z \sim 2$). Since our sample has no AGN examples, we use the recent models of Siebenmorgen & Efstathiou [157], which span a range in luminosities, size of emitting region, and optical depths to test the AGN locus on this diagram. We find that luminous, highly obscured AGN (we use the $\tau_V = 16$ model in Fig. *5.1.2*) most closely match the SCUBA galaxies colours. These optical depths are consistent with their extreme optical/near-IR faintness.

Note however, that even with these differences in mind it appears unlikely that SWIRE will detect the bulk of these sources (given that the SCUBA sources are typically at most $\sim 10\,$mJy, and SWIRE's $24\,\mu$m limit is $0.45\,$mJy).

The three FIRBACK ULIGs we have studied here are N1-040, N1-064 and N1-078. In Chapter 4, we concluded that these sources are colder, and likely have more extended star-

formation activity than typically assumed for ULIGs. This is qualitatively consistent with the cirrus models of Efstathious & Rowan-Robinson [147], which was also claimed as a possible model for the SCUBA galaxies. A small fraction of the SCUBA sources are indeed consistent with the SEDs of these galaxies, redshifted slightly to $z \sim 1-2$ (although even these are also consistent with type-I AGN). Most SCUBA galaxies, however, appear consistent with warmer ULIGs and highly obscured AGN, as discussed above. This is consistent with the conventional view that they are highly obscured, extreme starformers – the result of major mergers.

Whether or not AGN are present in SCUBA galaxies is an important question, in light of the evolutionary scenario for AGN-galaxy growth. Previous studies have shown, through analysis of their far-IR, radio, and X-ray emission, that the SCUBA galaxies are predominantly powered by extremely high levels of star-formation, and any AGN present do not contribute significantly to the sub-mm emission (and are likely to be highly obscured). The mid-IR colours of the bulk of the GOODS-North sources, however, are consistent with the idea of highly obscured AGN. The most recent X-ray stacking analysis in fact confirms that the majority of sources indeed harbour highly obscured AGN (although their sub-mm emission is dominated by the star-formation activity) [1].

It is also worth noting that the use of the commonly proposed 850 μm to 24 μm flux ratio as a redshift indicator, will at best be highly unreliable, due to the 24 μm band traversing the PAH emission and Si absorption features in the mid-IR, as well as because of the range of possible far-IR SEDs. On the whole the SCUBA galaxies appear to exhibit a large enough range in SED shapes that applying a single model to their mid-IR photometry would be misleading.

5.1.3 Implications for the CIB

Assuming that the sample discussed in Chapter 4 is fully representative of the entire FIRBACK population, we can use our fitted SEDs to constrain the contribution of $S_{170} > 135\,\mathrm{mJy}$ galaxies to the entire CIB. Fig. 5.3 shows the total contribution from the FIRBACK sources as the shaded region. Note that this region effectively corresponds to a single-source SED shape, due to the small range in redshifts of the sample. As already known from Dole et al. [37], the FIRBACK galaxies contribute $\lesssim 10\%$ of the CIB near to its peak. We can use this improved knowledge of their full IR spectra to constrain the nature of the remaining $\sim 90\%$ of the CIB contributors. One way to do this is to estimate the $\log(S_{850}/S_{24})$ colour of the residual spectrum (essentially of the CIB itself as the FIRBACK contribution is so small). Note that given the uncertainties in the CIB measurements this is only a very rough estimate. We estimate the $850\,\mu$m CIB at $\sim 0.9\,\mathrm{nWm^{-2}ster^{-1}}$ and the $24\,\mu$m one at $\sim 4\,\mathrm{nWm^{-2}ster^{-1}}$, which leads to $\log(S_{850}/S_{24})$ of ~ 0.9. In the previous section, we already discussed the redshift evolution of this colour and its dependence on galaxy type (see Fig. *5.1.2*). By comparing this with the residual CIB colour, we can immediately exclude significant contributions from quiescent spirals, AGN-dominated sources, and extremely cold sources (such as N1-040). This offers qualitative support to various galaxy evolution models which predict the CIB to be dominated by $z \sim 1$ starbursts/ULIGs, but not the typical/higher-z SCUBA sources, which are substantially warmer (see [23, 99]). With the unprecedented sensitivity of *Spitzer* in the mid-IR, we are now in a position to detect the average galaxy out to cosmologically-significant redshifts (see Fig. 5.1) as opposed to the usual picking off just the bright-end of the luminosity function. The colours of the CIB and the predicted redshift range of the bulk of the contributors suggest that they are already detected in these mid-IR surveys. A decisive test of this conclusion will be the

future *Herschel* observatory whose expected confusion limit of $\sim 20\,\mathrm{mJy}$ at $170\,\mu\mathrm{m}$ mean that it should be able to resolve the bulk of the CIB at its peak (which is its primary science goal). Optimally, this would happen by matching future *Herschel* sources with existing *Spitzer* data (e.g. as in the SWIRE ELAIS-N1 field). Below we test this directly.

5.2 Do the SWIRE colours support our views on galaxy evolution?

In Chapter 1, we discussed how our current views on recent galaxy evolution (i.e. since $z \sim 1$), involve a rapidly evolving, (approximately $\propto (1+z)^{\,4}$), LIG population, which is likely responsible both for the rapid rise in SFR density in that range and for the bulk of the far-IR CIB. The census of IR galaxies is completed by the rising importance of ULIGs, which are expected to dominate by $z \sim 2$. Despite its shallowness, the SWIRE survey, whose data we have made use of here, should largely detect both these populations given the moderate redshifts involved. In this section, using our new SEDs, we would like to decompose the SWIRE (star-formation-dominated) population, in order both to see whether such sub-populations are apparent, and to test the levels of evolution claimed for these types of galaxy. A full-blown analysis of galaxy evolution and luminosity functions is beyond the scope of this thesis, and therefore we aim here only at a more modest consistency check; however, we aim to do so using only the infrared colours of the SWIRE galaxies in order to demonstrate the power of colours to discriminate between models and different populations, as we speculated about in Chapter 3. Comparing the distribution of FIRBACK and SWIRE colours and fluxes in Fig. 4.6, we immediately see that, while FIRBACK is selecting low-z galaxies with high PAH-to-stars ratio (consistent with their vigorous SFR), the SWIRE galaxies as a whole are fainter and have bluer $\log(S_{8.0}/S_{4.5})$ colours. From our simulations in Chapter 3 this immediatelly leads us to

the conclusion that the redshift peak of the SWIRE population is higher than for our sample. Previous studies find the peak to be at $z \sim 0.2$, but extending beyond $z \sim 1$ [149].

5.2.1 Isolating star-formation-dominated sources

We start by selecting from the SWIRE ELAIS-N1 catalogue only those sources that are detected in all 4 IRAC bands and MIPS 24 μm. This leaves us with 3817 sources. We then wish to isolate the sources of greatest interest, i.e. the star-formation-dominated $z < 2$ sources. This involves applying the two cuts shown in Fig. 5.4, where 117 stellar-dominated sources are removed from the (S_{24}, S_8) plane, and a further 766 power-law-dominated sources are removed from the IRAC colour-colour plot leaving us with 2934 sources. These numbers tell us that the SWIRE MIPS sources are about 75% star-formation-dominated, and 25% AGN-dominated. This is in good agreement with the $\sim$70% star-foming galaxies, 30% AGN mix found by the SWIRE team in their ELAIS-N1 and Lockman Hole fields [149]. Some of the $\sim$5% difference in these results is probably due to our cutting out some $z \sim 2$ ULIGs along with the AGN, due to our simplistic colour cut (see for example Fig. *3.6.2*).

In the next subsections we will try to match the absolute number as well as the colour distribution of sources observed. Note, however, that although the SWIRE MIPS-covered ELAIS-N1 field is 1.3 deg^2, some of the sources have no quoted 24 μm flux, due to photometry problems such as confusion. Thus our criterion of MIPS detection might lead us to adopting a smaller effective survey area – we return to this below.

5.2.2 Survey simulation

In order to interpret the data we need to simulate surveys, as usual, we begin our simulation by taking a number of galaxy types, which we expect make up the bulk of the SWIRE sources.

Ideally, this would be represented by a continuum of sources as discussed in Chapter 3. However, for simplicity, here we take some representative SEDs only, and apply a colour scatter of $\sigma \sim 0.5$ to them to roughly emulate both the distribution of SED shapes and the photometric errors. As a representative set of SEDs, we choose a typical FIRBACK low-z galaxy (N1-007), a LIG (N1-015), and a ULIG (N1-064). We also expect a significant component of spiral galaxies, but since we do not have a good example in our sample, we take the closest SED (N1-009) and lower its PAH contribution slightly so that its $z \sim 0$ $\log(S_{8.0}/S_{4.5})$ colour is ~ 0.5, as expected for less vigorous starformers. Without this additional population, we cannot reproduce the large number of SWIRE sources observed to have a similar colour. We do not attempt to perform a rigorous statistical fit, but will merely look for qualitative agreement between our expectations and the observed colour distributions.

In order to have realistic relative numbers for the galaxy types at each redshift, we start with the luminosity function presented in Fig. 4.22. For the FIRBACK galaxies, we take the estimate we arrived at in Chapter 4 or $\log \phi = -2.3$ $[d \log L^{-1} \mathrm{Mpc}^{-3} \mathrm{ster}^{-1}]$. For the spirals we assume $\log \phi = -1.8$ (corresponding to the luminosity of N1-009 for the SDSS luminosity function). For the LIGs we assume a number density of the form: $\log \phi = -4.7 + (4.0 \pm 0.5) \log(1 + z)$, and for the ULIGs we assume: $\log \phi = -7.5 + (4.0 \pm 0.5) \log(1 + z)$. We weight these galaxy type/redshift pairs by including N realizations in the simulation, where $N \equiv \phi dV$, and dV is the relevant volume element. The observed $24\,\mu$m $3\,\sigma$ flux limit of 0.45 mJy is then imposed. Fig. 5.1, shows where this cuts off the various sources. Note that in order to arrive at a total number of sources consistant with that observed (2810 vs. 2934), we had to assume an effective survey area of $2.2\,\mathrm{deg}^2$. This is too large by ~ 1.5. We expect this to be due to our simplistic model where only a few SEDs (and therefore luminosities) are included, while the full spread

is accounted for by colour smearing. The sense of the correction suggests that this procedure has biased us against the low-L rather than the high-L end of the luminosity function (i.e. we are accounting for some more numerous and less luminous sources via less numerous and more luminous sources). We return to this point below.

5.2.3 Comparing 1D colour distributions

Due to its primary dependence on star-formation activity and secondary dependence on redshift, we first compare our simulated survey against the observed cumulative distribution in $\log(S_{8.0}/S_{4.5})$. This should tell us first whether or not we have the correct mix of SED types, and next whether or not we have the correct relative numbers as a function of redshift. Due to the flux limit imposed, we quite dramatically fail to reproduce the SWIRE distribution, if we only use FIRBACK-like galaxies, as expected. However, the inclusion of the other populations, especially the strongly-evolving LIGs, indeed brings us much closer to the observed distribution. Thus our chosen mix of galaxy types appears reasonable. Recall, however, that substantial colour smearing has been applied in order to yield smooth simulated distributions, and that in reality a continuum of source SEDs are present.

The cumulative colour distributions from 100 simulations, including all these galaxy types, are compared with the observed distribution in Fig. 5.5. It is apparent that our simple assumptions, based on current views of the degree of evolution of dusty galaxies since $z \lesssim 1$, are in good agreement with the observed $\log(S_{8.0}/S_{4.5})$ distribution. Significantly weaker or stronger evolution for the LIG or ULIG components would bring us below or above the curve, respectively. The greatest discrepancy between the observed and simulated distributions is for the bluest colours (we return to this point in the next sub-section).

Returning to the question of the unresolved CIB contributors, here we estimate the total contribution of our simulated galaxies to the 170 μm background. It is $\sim 13\,\mathrm{nWm^{-2}ster^{-1}}$. The CIB emission at $\sim 170\,\mu$m is poorly constrained, but estimates (at $\sim 140\,\mu$m in fact) range between ~ 15 and $50\,\mathrm{nWm^{-2}ster^{-1}}$ (see [69]). Within the uncertainties, it appears that, in our model, SWIRE galaxies can account for the bulk of the 170 μm CIB (see also Fig. 5.3). Lagache et al. [101] suggest that the 160 μm CIB will be resolved to better than 80% out to $z \sim 2.0$, whereas here it apperas that much lower redshift sources should be able to accomplish this.

In Fig. 5.5 we also show the distributions in 170 μm flux for our simulated galaxies and compare these with the FIRBACK *ISO* survey's $3\,\sigma$ limit, as well as a future *Herschel* survey's expected $3\,\sigma$ limit of $\sim 20\,$mJy. From our model simulations, we conclude that the CIB should be largely resolved by sources brighter than ~ 30. *Herschel* should therefore easily resolve the far-IR CIB (at least at the shorter wavelengths of the PACS instrument) as expected. Moreover, the SWIRE+*Herschel* overlap here will be very useful in establishing the nature of these sources. Comparing with other published work, we find that some predictions have been more pessimistic about the required flux for resolving the CIB (as low as $\sim 2-5\,$mJy [37]). Recall, however, that our simulation suffers from a bias agains high number density, but low-L galaxies. In light of that, our estimates are probably only upper limits.

5.2.4 Comparing 2D colour maps

In the previous section, we saw that even having a single colour allows us to constrain the degree of evolution of our chosen sources, as well as to test whether or not we were missing some galaxy populations from our model. In principle, looking at the 2D distribution of a colour-colour plot (or even higher dimensional spaces of multi-colour distributions) should be

even more constraining as discussed already in Chapter 3.

In Fig. 5.6, we compare the distributions of source density obtained from binning the observed IRAC colour-colour plot from the SWIRE data, with a similar 'map' obtained from a random realization of our simulated survey. The first thing to note, is that without any special effort, we can roughly reproduce the broad distribution of galaxy colours. Note that, we did not see the now noticeable vague discontinuity at $\log(S_{8.0}/S_{4.5}) \sim 0.3$ in our simulations of Chapter 3, because there we did not include extinction effects. This shape arises simply because beyond $z \sim 0.3$ the flux limit does not allow us to detect $\log(L/L_{\odot}) \lesssim 11$ galaxies. Thus the bottom half of this plot consists of LIGs and ULIGs whose typical optical depths are higher, leading to redder $\log(S_{5.8}/S_{3.6})$ colours. However, as the redshift increases, this colour climbs the stellar peak, which makes it progressively bluer again until $z \sim 1.5$, when there is an abrupt turn towards the red again (at which point we enter the domain of the colour cut-off discussed in Section *5.2.1*).

The largest discrepancy between our model and the observed colour-colour plot in Fig. 5.6, is in the blue tail of the distribution next to the LIG-ULIG sequence. Higher redshfits than those considered here would push us in the opposite direction, toward redder $\log(S_{5.8}/S_{3.6})$ colours, as discussed above. It appears that the only way to obtain colours like these is to have low-z galaxies with very low (but higher than in the ellipticals) dust-to-stars ratio. These galaxies, moreover, all have low $24\,\mu$m fluxes, $\lesssim 1$ mJy. This, combined with the inferred low redshifts, implies that they have dwarf-like luminosities (i.e.$\lesssim 10^{10}\,\mathrm{L}_{\odot}$). Starforming dwarfs are commonly believed (although the point is debatable) to have lower PAH emission, because of carrier destruction due to the too weak shielding provided by their metal-poor ISM. It seems believeable therefore that this part of the colour-colour diagram belongs to the so far undiscussed

metal-poor star-forming dwarf galaxies. Note that this deficit is fill in by our more-luminous spiral and FIRBACK galaxies to add up to the total number of sources (as discussed above). This excess is therefore also evident in the absolute difference map.

5.2.5 **A new approach to galaxy evolution modelling**

In this section, we have shown that the 1D and 2D colour distributions are useful tools in constraining evolutionary models, and moreover are more sensitive to the choices of SEDs included in the models than if number counts alone are used. The next step in fitting galaxy evolution models would be to use these multi-dimensional distributions. Ideally, we would like to be able to find the best model through some form of optimization process, rather than the traditional method of guesswork and anecdotal comparison. One approach, for example, would be to generate similated flux and colour distributions as in the previous section, and directly compare these with the observed one via a maximum likelihood analysis, taking into account Poisson statistics and selection biases. This is a similar application to matching simulated colour-magnitude diagrams to constrain the SFHs of stellar systems (as in nearby dwarf galaxies) [38], statistical studies of spectra of optical galaxy samples such as SDSS [121], or fitting luminosity functions of radio galaxies (e.g. [42]).

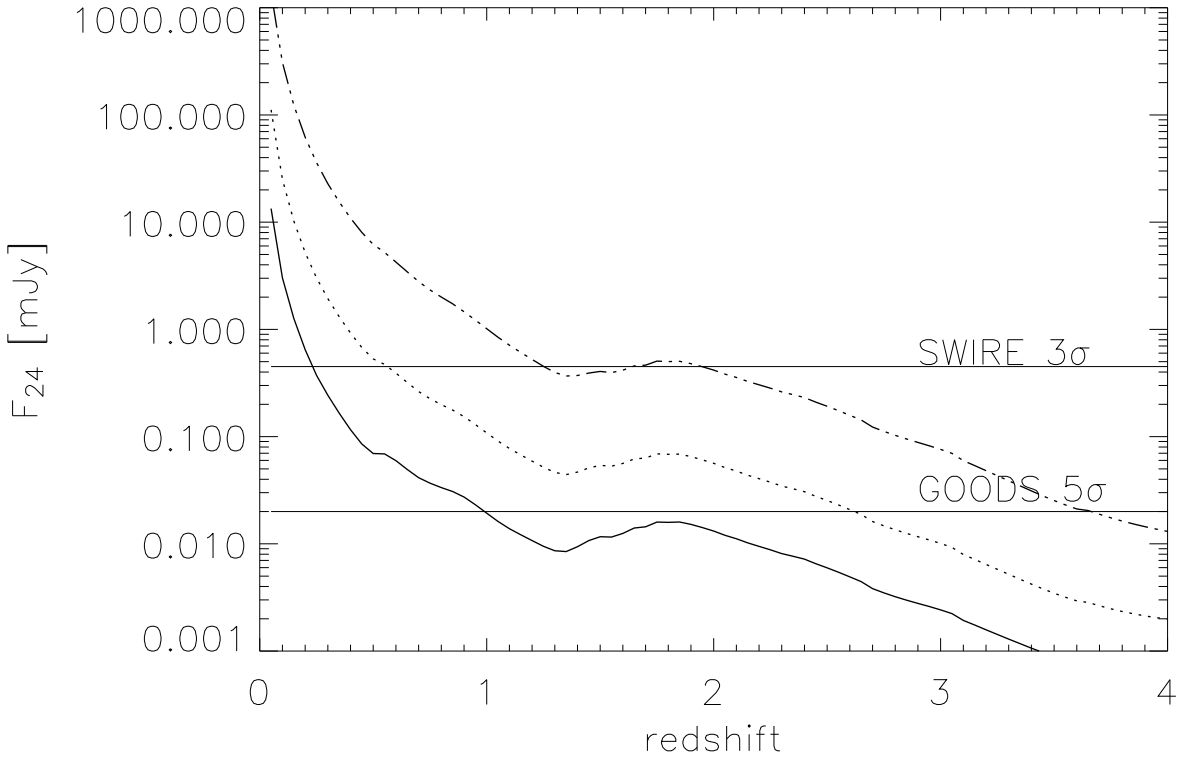

Fig. 5.1: Detectability of FIRBACK galaxies as a function of redshift compared with the *Spitzer* 24 μm survey limits for SWIRE [166], and GOODS [22]. The solid line SED corresponds to a typical low-z FIRBACK source (N1-007), while the dotted line represents a LIG (N1-015), and the dashed line is a cold ULIG (N1-064). Note that the level of PAH contribution is uncertain in the last case and therefore it might not be detectable by SWIRE at $z \sim 2$ as suggested in this figure.

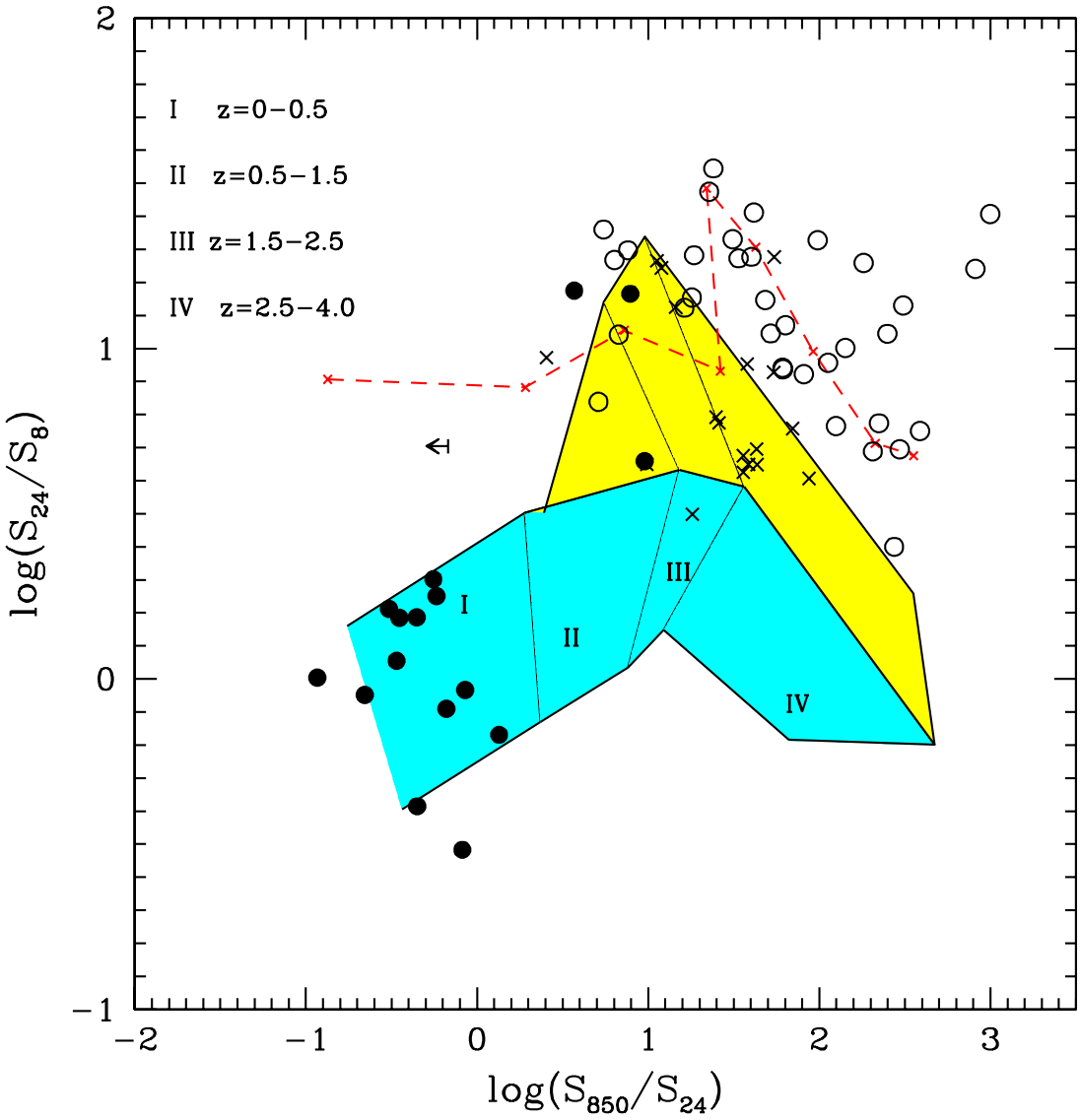

Fig. 5.2: The evolution of two diagnostic colours: S_{850}/S_{24} and S_{24}/S_8. The solid circles are our FIRBACK sample, and the open circles are SCUBA-selected galaxies from GOODS-North (Pope et al. in preparation), while the crosses are other SCUBA-selected samples from shallower surveys [48, 55]. The upper limit is N1-013 ($S_{850} < 0$). The cyan region represents $\log L \lesssim 11$ while the yellow region stands for $\log L \gtrsim 11$ (the boundaries should be regarded as fuzzy). The redshift evolution of the SEDs is done in steps of 0.5 from $z = 0$ to $z = 4$. The SED curves used from top to bottom are: N1-064, N1-015 and N1-009. The red dashed curve is a $\tau_V = 16$ AGN model [157].

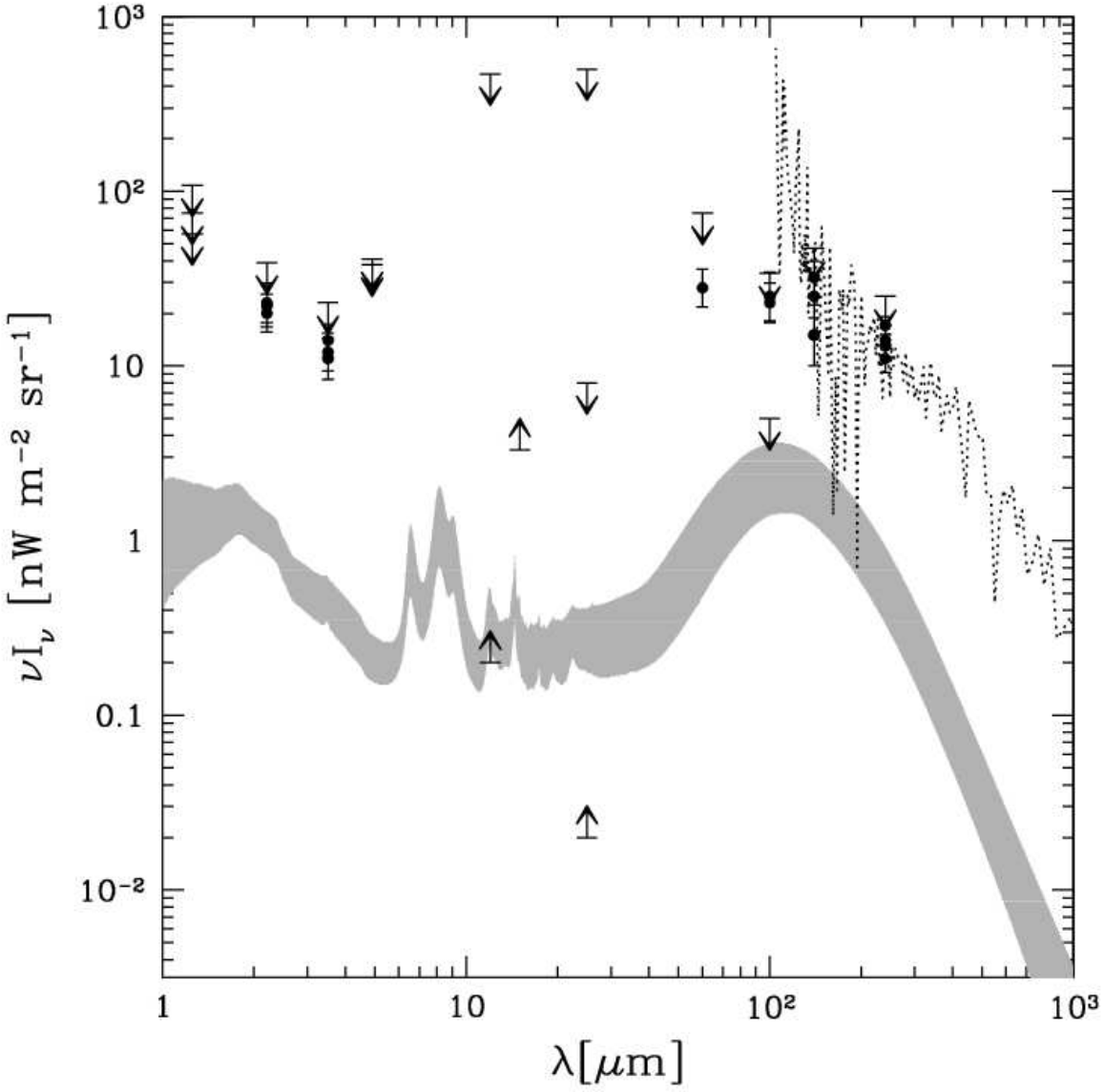

Fig. 5.3: The greyscale contribution of FIRBACK galaxies to the CIB assuming our sample is representative of the entire catalogue. Constraints of the CIB consist of a set of upper and lower limits, as well as different estimates for detection, not all of which are consistent with each other – see Hauser & Dwek [69] for details of these CIB measurements, as well as full references.

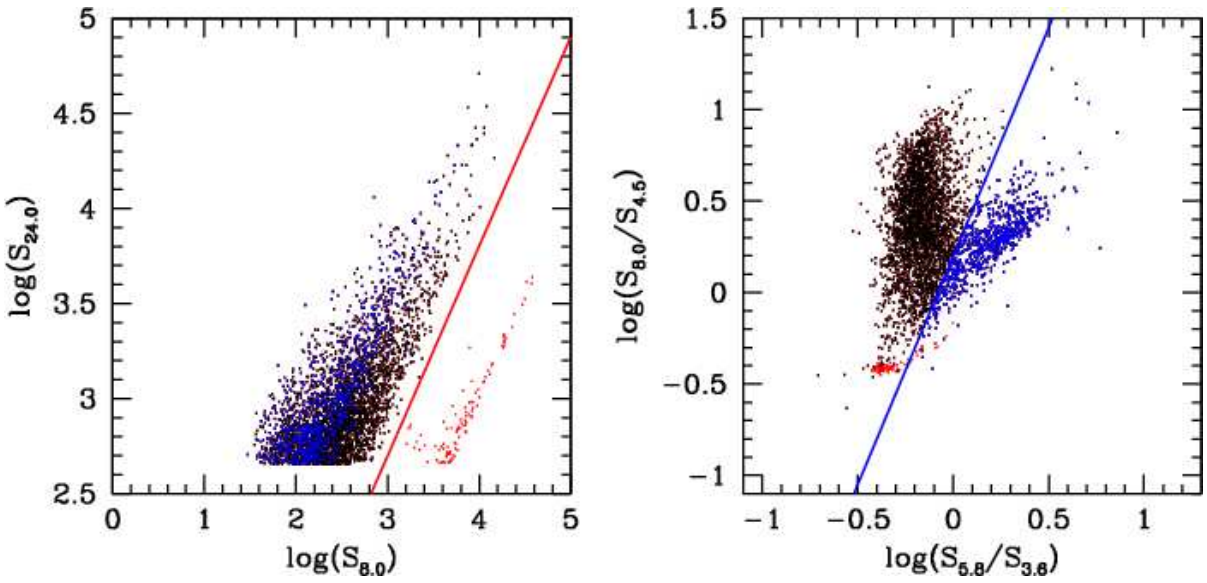

Fig. 5.4: *Left:* The SWIRE flux-flux distribution used for removing ellipticals (red points). *Right:* The SWIRE colour-colour distribution used for removing AGN, and some potential higher-z sources (the blue points). After these steps a total of 2934 sources detected in all five bands are left in the ELAIS-N1 catalogue.

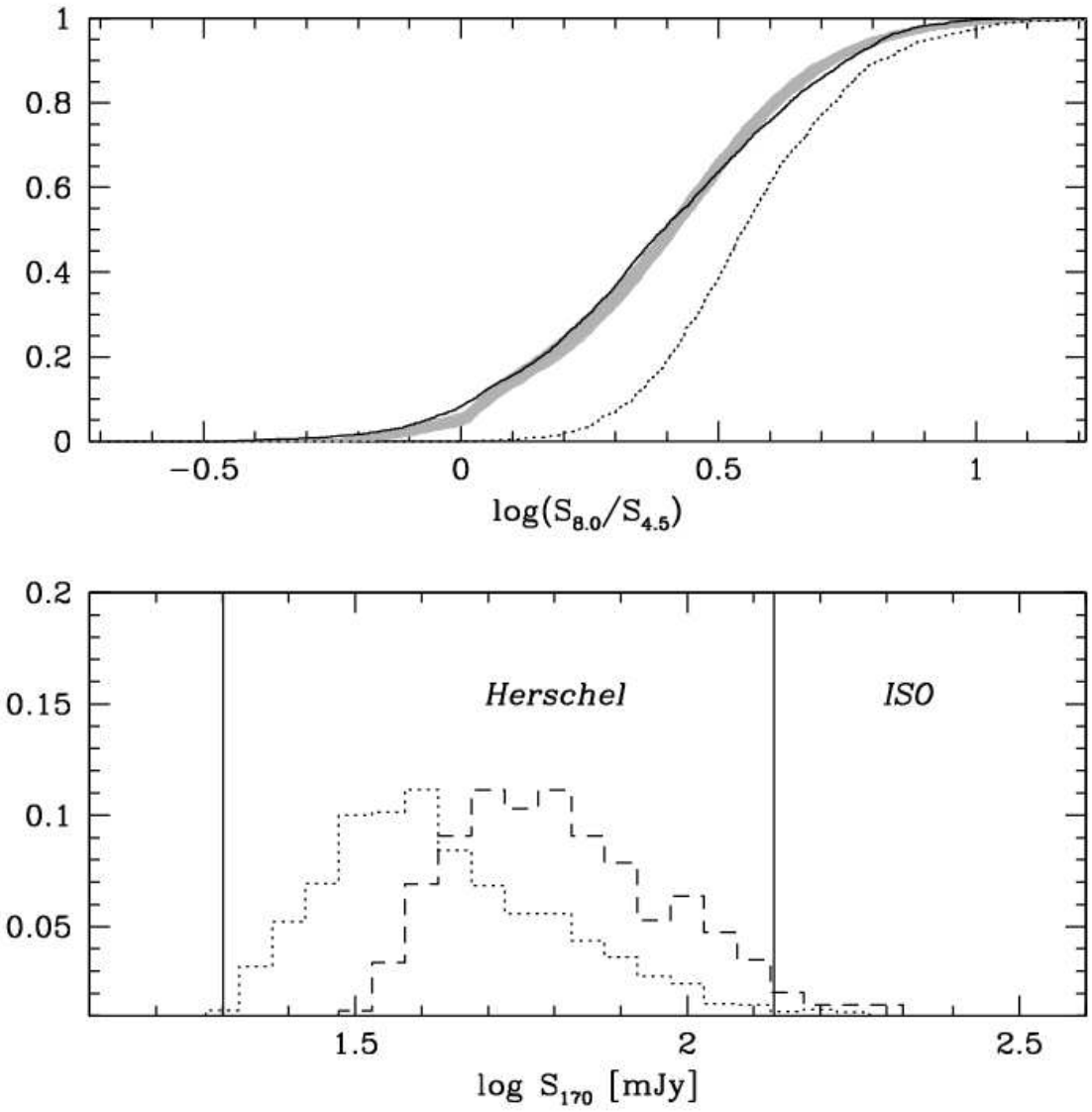

Fig. 5.5: *Top:* The solid black line shows the observed cumulative distribution of the fraction of sources above a given colour for the SWIRE survey, after AGN and elliptical galaxies have been removed. The grey lines show 100 simulations including low-z FIRBACK galaxies, spirals, and strongly-evolving LIGs, and ULIGs. The dotted line shows the contribution of the low-z FIRBACK sample alone. It is clear that the same colour distribution cannot fit the spread of SWIRE $S_{8.0}/S_{4.5}$ colour – this requires galaxies with a much higher fraction of bluer colours. *Bottom:* The distribution of 170 μm flux, where the dotted line represents the more quiescent sources (FIRBACK-like plus spirals), while the dashed line represents the LIG and ULIG population. The solid

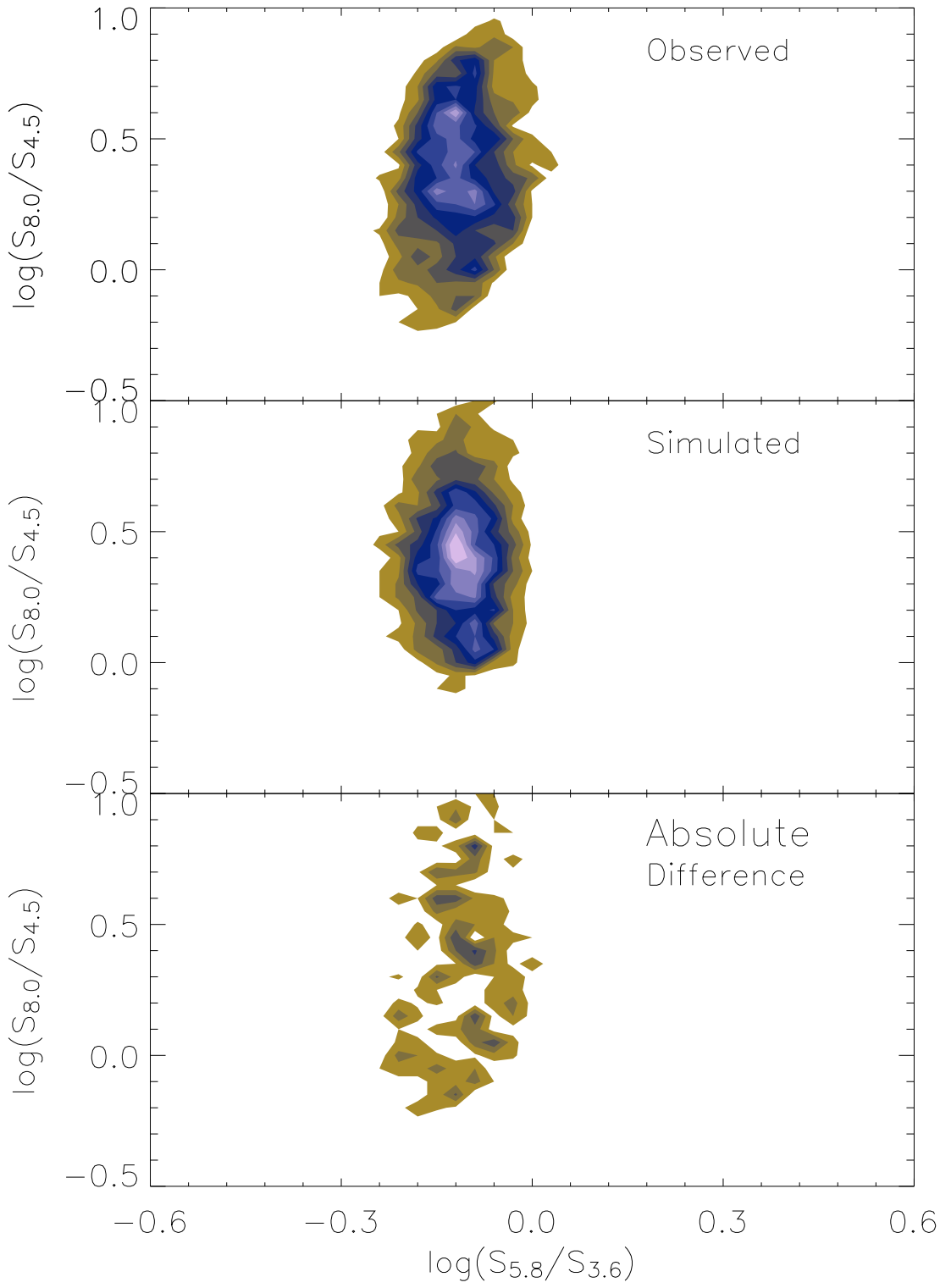

Fig. 5.6: *Top:* The binned $\log(S_{8.0}/S_{4.5})$ vs. $\log(S_{5.8}/S_{3.6})$ distribution from SWIRE, after AGN and elliptical removal. The binsize used is 0.05 in log(colour). *Middle:* The same plot for the simulated survey, as described in the text. *Bottom:* The residual distribution. In all cases the levels range from 5 to 50 sources in steps of 5.

CHAPTER 6

SUMMARY & FUTURE WORK

6.1 Summary of thesis

A better grasp of the subject of this thesis, the infrared SEDs of star-forming galaxies, is crucial for optimal use of the present and upcoming generations of multi-wavelength infrared survey data. We have shown that IR data are particularly useful tools for following the evolution of strongly star-forming galaxies, which are our tools for testing and furthering our understanding of galaxy formation and evolution. This thesis addresses several issues related to the observations, modelling, and use of broadband IR SEDs in interpreting multiwavelength data and constructing galaxy evolution models.

In Chapter 3, we used a sample of low resolution *ISO* spectra of a wide range of galaxy types as a basis for predicting what the then yet-to-see-first-light *Spitzer* Space Telescope would reveal. This was accomplished with a new phenomenological model of mid-IR spectra based on breaking them up into the principle components responsible for broad-band spectral variations. Simulated colour-colour diagrams for the IRAC and MIPS instruments resulted including the effects of redshift. These diagrams were used throughout the rest of this thesis, as a diagnostic to understanding the mid-IR colours of galaxies.

Next, we presented a comprehensive study of the full $1-1000\,\mu$m SEDs of a sample of 22 FIRBACK galaxies selected at $170\,\mu$m, near the peak of the CIB. Our new multi-component model and MCMC fitting techniques have allowed us to test various previous assumptions

about FIRBACK galaxies and the spectral templates used to model them as well as related populations. In particular, we find them to be colder than suspected on the basis of earlier models. This finding supports the modification applied by Lagache et al. [100] to their starburst template in order to fit the 24 μm number counts [122]. Similarly, our ULIGs are found to be much colder that the 'prototypical' ULIG Arp220. A general conclusion is that in cases where the data allow, as is the case here, multi-component models always provide better fits than (effectively single-parameter) known galaxy templates. Moreover, the use of the Markov Chain Monte Carlo approach, allows not only for accurate multi-parameter fits, but also accurate error determination.

In the process of carrying out this SED study, we have addressed several issues of practical concern including: source confusion, the practicality of estimating purely infrared-based photometric redshifts; the pitfalls of the ubiquitous greybody fitting approach; and selection biases in particular filter-based biases in our ideas of 'typical' SEDs. In addition, we have been able to extract for our sample several SED-based physical parameters, including luminosities, masses, optical depths, and SFRs. We combined these in a variety of ways to learn more about the nature of our sources. The extraction of some of these parameters is quite model dependent, and we discussed the limitations this imposes.

In Chapter 5, we considered possible implications of our findings on the infrared SEDs of normal star-forming galaxies for some current issues in extragalactic astronomy. We ended by pulling together the experience of the previous two chapters to speculate on the nature of the remaining roughly 90% of the CIB contributors, based on a comparison with the colours of the SWIRE sources.

6.2 Future work based on this thesis

The field of multi-wavelength SED fitting of extragalactic populations is still very much open to investigation in general. However, we can mention several specific points of future research, which could directly follow from this thesis:

1) It should be possible to construct SED shapes of a wider range of galaxies up to $z \sim 1$ as a function of luminosity, mass, and metallicity. This could include traditional optical data, and in principle could extend all the way from X-ray to radio. Deep ongoing surveys, and detailed spectroscopy of individual sources (including use of *Spitzer* and *Herschel*) will help immensely to constrain the crucial mid-IR waveband. Consequently, it should be possible to determine what underlying properties are most important in defining the SED shape.

2) How are the integrated SEDs we observe in distant galaxies assembled? If we look at local resolved galaxies, can we add up their parts to obtain an overall SED, which matches that of an unresolved distant galaxy? And consequently what information can we extract (if any) about spatial structure using unresolved or weakly resolved galaxies? For example, can we understnad why global relations such as the Schmidt law and the $L_{\rm IR}-{\rm SFR}$ relation work, and when they break down?

3) Can the relationshipo between star-formation and AGN activity be consistently modelled and tested? The standard view of merger-induced ULIGs suggests the predominance of a nucleated burst of star-formation (such as required to possibly feed a black hole), which seems contrary to our findings (given that we found no clear evidence of our ULIGs being centrally

concentrated). This suggests that the merger process and accompanying star-formation is far more complex. A study of resolved multi-colour images of ULIGs (at $z \gg 0$) would be particularly enlightening here.

4) To what a degree does the known variability of the PAH features (with environment) affect the global spectra? What is the relative contribution of optical/UV photons to heating the PAH carriers? Does the strength of the PAH features really trace SF or the general ISRF?

5) How does the currently poorly known mid-IR SED vary with redshift? Are PAH features ubiquitous in high-z sources (as suggested by some of our ULIGs), and if so why (given the expectations of carrier destruction in the intense ISRF s)?

6) Given the often significant differences in beamsize, assigning counterparts in a multi-wavelength study is non-trivial, since often multiple source of unknown redshifts contribute comparably. Is there a better, more probabilistic approach to disentanging these contributions and deriving SED information, which would be preferable to choosing the brightest/most central source (as is often done currently).

7) How can one improve the photometric redshift techniques suggested here so they can be used in a wider range of applications, especially for wide field infrared surveys without the traditionally necessary optical coverage. Even if optical coverage exists this might allow us to investigate at a wider range of sources (in particular very dusty ones) or double check for accuracy among different redshift indicators.

8) As an extension of the previous, can significant improvement be made via the direct determination of redshift in the far-IR or sub-mm, using lines of CO or low ionization atomic species (such as CII or OI)? Such data will soon be available through instrument on GBT, CSO, LMT, etc.

9) A more efficient use of survey data requires the inclusion of multi-dimensional colour information to constrain galaxy evolution models. Several issues need to be sorted our before this becomes practical including the optimal statistic to use, allowing for a continuum of source SEDs (or allowing SED mixing in the code), and correct inclusion of statistical and systematic noise.

10) Lastly, we have made extensive use of the Markov Chain Monte Carlo technique in this thesis. We have found it to be a powerful tool in our work. We believe its use in astronomy will grow in the near future, and in particular in problems related to the highly complex processes behind galaxy formation. However, without proper optimization of the relevant numerical parameters the technique can be unyieldy. We discussed in Appendix A how we addressed these for our particular fitting procedure. However, before this technique can be more widely accepted, its virtues and limitations need to be explored further than we have done here. In particular, we believe, that it will be most powerful in combination with other algorithms such as for example simulated annealing (as used in Chapter 3), simulated tempering, genetic algorithms, or downhill-simplex to name but a few examples.

Many of these are well known issues in extragalactic, infrared astronomy and are on the agenda of large collaborations such as SINGS [89] and SWIRE [110]. Moreover, in the further future, IR studies will no longer be starved of SNR and resolution as they are now (e.g. ALMA, JWST, SPICA), which will overcome many of the current limitations.

BIBLIOGRAPHY

[1] Alexander DM, Bauer FE, Chapman SC, et al. 2005, ApJ, in press, (astro-ph/0506608)

[2] Archibald EN, et al. 2002, MNRAS, 336, 1

[3] Aretxaga I, Hughes D, Dunlop JS 2005, MNRAS, 358, 1240

[4] Barnard VE, PhD thesis, University of Cambridge, 2002

[5] Baugh CM, Lacey CG, Frenk CS, et al. 2005, MNRAS, 356, 1191

[6] Bell EF, & de Jong RS 2001, ApJ, 550, 212

[7] Bell EF, Papovich C, Wolf C, et al. 2005, ApJ, 625, 23

[8] Blain A, Barnard VE, Chapman S 2003, MNRAS, 338, 733

[9] Blain AW, Smail I, Ivison RJ, Kneib J-P, Frayer DT 2002, PhR, 369, 111

[10] Blanton MR, et al. 2003, ApJ, 592, 819

[11] Blumenthal GR, Faber SM, Primack JR, Rees MJ 1984, Nature, 311, 517

[12] Boselli A, Sauvage M, Lequeux J, Donati A, Gavazzi G 2003, A&A, 406, 867

[13] Boulanger F, Boissel P, Cesarsky C, & Ryter C 1998, A&A, 339, 194

[14] Bruzual G, & Charlot S 2003, MNRAS, 344, 1000

[15] Bundy K, Ellis RS, & Conselice CJ 2005, ApJ, 625, 621

[16] Cabanac RA, de Lapparent V, Hickson P 2002, A&A, 389, 1090

[17] Carroll SM, Press WH, Turner EL, 1992, ARAA, 30, 499

[18] Cesarsky CJ, et al. 1996, A&A, 315, L32

[19] Chapman SC, Smail I, Ivison RJ, Helou G, Dale DA, Lagache G 2002, ApJ, 573, 66

[20] Chapman SC, Helou G, Lewis GF, & Dale DA 2003, ApJ, 588, 186

[21] Chapman SC, Blain AW, Smail I, & Ivison RJ 2005, ApJ, 622, 772

[22] Chary R, et al. 2004, ApJS, 154, 80

[23] Chary R, Elbaz D 2001, ApJ, 556, 562

[24] Clavel J, Schulz B, Altieri B, Barr P, Claes P, et al. 2000, A&A, 357, 839

[25] Cohen M, Wheaton WA, & Megeath ST 2003, AJ, 126, 1090

[26] Connolly AJ, Csabai I, Szalay AS, Koo DC, Kron RG, & Munn JA 1995, AJ, 110, 2655

[27] Conselice CJ 2003, ApJS, 147, 1

[28] Contursi A, Boselli A, Gavazzi G, Bertagna E, Tuffs R, & Lequeux J 2001, A&A, 365, 11

[29] Dale D, Helou G, Contursi A, Silbermann N, Kolhatkar S 2001, ApJ, 549, 215

[30] Dasyra KM, Xilouris EM, Misiriotis A, Kylafis ND, A&A, in press, (astro-ph/0503698)

[31] Dekel A, & Silk J 1986, ApJ, 303, 39

[32] Dennefeld M, et al. 2005, in press, (astro-ph/0504344)

[33] Désert FX, Boulanger F, & Puget J-L 1990, A&A, 2347, 215

[34] Devlin MJ, et al. 2004, Proc. SPIE, 5498, 42

[35] Dickinson M, Giavalisco M, & The Goods Team 2003, *The Mass of Galaxies at Low and High Redshift*, 324

[36] Dickinson M, Papovich C, Ferguson HC, & Budavári T 2003, ApJ, 587, 25

[37] Dole H, et al. 2001, A&A, 372, 364

[38] Dolphin AE, 2002, MNRAS, 332, 91

[39] Dopita MA, et al. 2005, ApJ, 619, 755

[40] Draine BT, & Lee HM 1984, ApJ, 285, 89

[41] Draine B 2003, ApJ, 598, 1017

[42] Dunlop JS, & Peacock JA 1990, MNRAS, 247, 19

[43] Dunlop JS 2005, ASSL Vol. 329: *Starbursts: From 30 Doradus to Lyman Break Galaxies*, 121

[44] Dunne L, & Eales SA 2001, MNRAS, 327, 697

[45] Dunne L, Eales S, Ivison R, Morgan H, & Edmunds M 2003, Nature, 424, 285

[46] Dupac X, et al. 2003, A&A, 404, L11

[47] Dyson JE, Williams DA, 1997 *The Physics of the Interstellar Medium*, IOP Publishing

[48] Egami E, et al. 2004, ApJS, 154, 130

[49] Eggen OJ, Lynden-Bell D, & Sandage AR 1962, ApJ, 136, 748

[50] Farrah D, Serjeant S, Efstathiou A, Rowan-Robinson M, & Verma A 2002, MNRAS, 335, 1163

[51] Fazio GG, et al. 2004, ApJS, 154, 10

[52] Fioc M, Roca-Volmerange B 1997, A&A, 326, 950

[53] Firth AE, Lahav O, & Somerville RS 2003, MNRAS, 339, 1195

[54] Förster Schreiber NM, Roussel H, Sauvage M, & Charmandaris V 2004, A&A, 419, 501

[55] Frayer D, et al. 2004, ApJS, 154, 137

[56] Gamerman D 1997, *Markov Chain Monte Carlo: Stochastic Simulation for Bayesian Inference*, Chapman and Hall, London

[57] Gelfand AM, Sahu SK 1994, Journal of Computational and Graphical Statistics, 3(3), 261

[58] Giavalisco M, et al. 2004, ApJ, 600, L103

[59] Gil de Paz A, Aragón-Salamanca A, Gallego J, Alonso-Herrero A, Zamorano J, & Kauffmann G 2000, MNRAS, 316, 357

[60] Gil de Paz A, Madore BF, & Pevunova O 2003, ApJS, 147, 29

[61] Gilmore G 2001, ASP Conf. Ser. 230: *Galaxy Disks and Disk Galaxies*, 230, 3

[62] Gordon KD, et al. 2004, ApJS, 154, 215

[63] Gregory P, 2005, *Bayesian Logical Data Analysis for the Physical Sciences*

[64] Guzmán R, Östlin G, Kunth D, Bershady MA, Koo DC, & Pahre MA 2003, ApJ, 586, L45

[65] Haas M., Klaas U., & Bianchi S. 2002, A&A, 385, L23

[66] Hammer et al. 2001, ApJ, 550, 570

[67] Harwit M 2004, Advances in Space Research, 34, 568

[68] Hastings WK 1970, Biometrika, 57, 97

[69] Hauser MG, & Dwek E 2001, ARA&A, 39, 249

[70] Heavens A, et al. 2004, Nature, 428, 624

[71] Heckman T 2005, ASSL, 329: *Starbursts: From 30 Doradus to Lyman Break Galaxies*, 3

[72] Helou G, Khan IR, Malek L, & Boehmer L 1988, ApJS, 68, 151

[73] Helou G, Lu NY, Werner MW, Malhotra S, Silbermann N 2000, ApJ, 532, 21

[74] Hogg DW, Tremonti C, Blanton MR, Finkbeiner DP, Padmanabhan N, Quintero AD, Schlegel DJ, Wherry N 2005, ApJ, 624, 162

[75] Holland W, et al.,1999, MNRAS, 303, 659

[76] Hopkins AM 2004, ApJ, 615, 209

[77] Houck JR, et al. 2004, ApJS, 154, 18

[78] Hudgins DM & Allamandola LJ 2004, *Astrophysics of Dust* Publisher: ASP. Editors: Witt, A., Clayton, G. & Draine, B.

[79] Hughes DH, et al. 1998, Nature, 394, 241

[80] Ivison RJ, et al. 2004, ApJS, 154, 124

[81] James A, Dunne L, Eales S, & Edmunds MG 2003, Revista Mexicana de Astronomia y Astrofisica Conference Series, 17, 269

[82] Jarrett TH, Chester T, Cutri R, Schneider SE, & Huchra JP 2003, AJ, 125, 525

[83] Jenness T, & Lightfoot JF 1998, ASP Conf. Ser. 145: Astronomical Data Analysis Software and Systems VII, 145, 216

[84] Juneau S, Glazebrook K, Crampton D, et al. 2005, ApJ, 619, L135

[85] Kauffmann G, et al. 2003a, MNRAS, 341, 33

[86] Kauffmann G, et al. 2003b, MNRAS, 346, 1055

[87] Kennicutt RC 1998, ApJ, 498, 541

[88] Kennicutt RC 1998, ARA&A, 36, 189

[89] Kennicutt RC, et al. 2003, PASP, 115, 928

[90] Kessler MF, et al. 1996, A&A, 315, L27

[91] Kewley LJ, Geller MJ, Jansen RA, & Dopita MA 2002, AJ, 124, 3135

[92] Kirkpatrick S 1984, Journal of Statistical Physics, 34(5/6), 975

[93] Knapp GR, & Kerr FJ 1974, A&A, 35, 361

[94] Koo DC, Bershady MA, Wirth GD, Stanford SA, & Majewski SR 1994, ApJ, 427, L9

[95] Lacy M, Canalizo G, Rawlings S, Sajina A, Storrie-Lombardi L, Armus L, Marleau FR, & Muzzin A 2005, Memorie della Societa Astronomica Italiana, 76, 154

[96] Lacy M, Storrie-Lombardi LJ, Sajina A, Appleton P, Armus L, et al. 2004, ApJS, 154, 166

[97] Lacy M, et al. 2004, ApJS, in press, (astro-ph/0507143)

[98] Lagache G, & Puget JL 2000, A&A, 355, 17

[99] Lagache G, Dole H, & Puget J-L 2003, MNRAS, 338, 555

[100] Lagache G, et al. 2004, ApJS, 154, 112

[101] Lagache G, Puget J-L, Dole H, 2005, ARAA, in press, (astro-ph/0507298)

[102] Laurent O, Mirabel IF, Charmandaris V, Gallais P, et al. 2000, A&A, 359, 887

[103] Le Floc'h E, Pérez-Gonzales PG, Rieke GH, Papovich C, et al. 2004, 154, 170

[104] Leinert C, et al. 1998, A&AS, 127, 1

[105] Lemke D, Wolf J, Schubert J, & Patrashin MA 1993, Proc. SPIE, 1946, 261

[106] Lewis A & Bridle S 2002, Phys. Rev. D, 66, 103511

[107] Li A, & Draine BT 2002, ApJ, 572, 232

[108] Lilly SJ, Le Fevre O, Hammer F, Crampton D 1996, ApJ, 460, 1

[109] Lisenfeld U, & Ferrara A 1998, ApJ, 496, 145

[110] Lonsdale CJ, et al. 2003, PASP, 115, 897

[111] Lu N, Helou G, Werner MW, Dinerstein HL, Dale DA, et al. 2003, ApJ, 588, 199

[112] MacArthur LA, Courteau S, Bell E, & Holtzman JA 2004, ApJS, 152, 175

[113] Mac Low M-M, & Ferrara A 1998, LNP Vol. 506: IAU Colloq. 166: *The Local Bubble and Beyond*, 506, 559

[114] Magorrian J, et al. 1998, AJ, 115, 2285

[115] Massarotti A, Iovino A, Buzzoni A, 2001, A&A, 368, 74

[116] Metropolis N, Rosenbluth AW, Rosenbluth MN, Teller AH, Teller E 1953, Journal of Chemical Physics, 21, 1087

[117] Murakami H, 1998, Proc. SPIE 3356, 471

[118] Nagamine K, et al. 2004, ApJ, 610, 45

[119] Neugebauer G, et al. 1984, ApJ, 278, L1

[120] Oliver S, et al. 2000, MNRAS, 316, 749

[121] Panter B, Heavens AF, & Jimenez R 2003, MNRAS, 343, 1145

[122] Papovich C, et al. 2004, ApJS, 154, 70

[123] Patris J, Dennefeld M, Lagache G, & Dole H 2003, A&A, 412, 349

[124] Pearson CP, et al. 2004, MNRAS, 347, 1113

[125] Pearson CP, Chan KW, & Onaka T 2004, MNRAS, 350, 473

[126] Peeters E, Hony S, van Kerckhoven C, Tielens AGGM, Allamandola LJ, Hudgins DM, & Bauschlicher CW 2002, A&A, 390, 1089

[127] Peeters E, Spoon HWW, & Tielens AGGM 2004, ApJ, 613, 986

[128] Pei YC, Fall SM, & Hauser MG 1999, ApJ, 522, 604

[129] Persic M, Salucci P, Stel F 1996, MNRAS, 281, 27

[130] Phillipps S, 2005, *The Structure and Evolution of Galaxies*, John Wiley & Sons

[131] Pier EA & Krolik JH 1993, ApJ, 418, 673

[132] Pierini D, Popescu CC, Tuffs RJ, Völk HJ 2003, A&A, 409, 907

[133] Piovan L, Tantalo R, & Chiosi C 2003, A&A, 408, 559

[134] Popescu CC, Misiriotis A, Kylafis ND, Tuffs RJ, & Fischera J 2000, A&A, 362, 138

[135] Popescu CC, & Tuffs RJ 2005, AIP Conf. Proc. 761: *The Spectral Energy Distributions of Gas-Rich Galaxies: Confronting Models with Data*, 761

[136] Popescu CC, et al. 2005, ApJ, 619, L75

[137] Puget J-L, Leger A, & Boulanger F 1985, A&A, 142, 19

[138] Puget J-L, Abergel A, Bernard J-P, Boulanger F, Burton WB, Désert F-X, Hartmann D 1996, A&A, 308, L5

[139] Puget J-L, Lagache G, Clements D, Reach WT, Aussel H, Bouchet FR, Cesarsky C, Désert F-X, et al. 1999, A&A, 345, 29

[140] Quinn T, Katz N, & Efstathiou G 1996, MNRAS, 278, L49

[141] Ravindranath S, et al. 2004, ApJ, 604, L9

[142] Rieke GH, et al. 2004, ApJS, 154, 25

[143] Roberts GO, Gelman A, Gilks WR 1997, Annals of Applied Probability, 7, 110

[144] Robson I, Priddey RS, Isaak KG, & McMahon RG 2004, MNRAS, 351, L29

[145] Rodighiero G, Lari C, Fadda D, Franceschini A, Elbaz D, Cesarsky C 2004, A&A, 427, 773

[146] Rowan-Robinson M 2001, New Astronomy Review, 45, 631

[147] Efstathiou A, & Rowan-Robinson M 2003, MNRAS, 343, 322

[148] Rowan-Robinson M, et al. 2004, MNRAS, 351, 1290

[149] Rowan-Robinson M, et al. 2005, AJ, 129, 1183

[150] Sajina A, Borys C, Chapman S, Dole H, Halpern M, Lagache G, Puget J-L, Scott D 2003, MNRAS, 343, 1365

[151] Sajina A, Lacy M, Scott D 2005, ApJ, 621, 256

[152] Sanders DB, Mirabel IF 1996, ARA&A, 34, 749

[153] Schlegel DJ, Finkbeiner DP, & Davis M 1998, ApJ, 500, 525

[154] Schmidt M 1959, ApJ, 129, 243

[155] Scott D, Lagache G, Borys C, Halpern M, Sajina A, Ciliegi P, Clements DL, et al. 2000, A&A, 357, L5

[156] Serjeant S, et al. 2004, ApJS, 154, 118

[157] Siebenmorgen R, & Efstathiou A 2005, AIP Conf. Proc. 761: *The Spectral Energy Distributions of Gas-Rich Galaxies: Confronting Models with Data*, 761, 245

[158] Silva L, Granato GL, Bressan A, Danese L 1998, ApJ, 509, 103

[159] Simpson C & Eisenhardt P 1999, PASP, 111, 691

[160] Soifer BT, Sanders DB, Madore BF, Neugebauer G, Danielson GE, Elias JH, Lonsdale CJ, & Rice WL 1987, ApJ, 320, 238

[161] Somerville R, Primack J, Faber S 2001, MNRAS, 320, 504

[162] Spoon HWW, Keane JV, Tielens AGGM, Lutz D, Moorwood AFM, & Laurent O 2002, A&A, 385, 1022

[163] Springel V, White SM, Jenkins A, et al. 2005, Nature, 435, 269

[164] Stern D, et al. 2004, American Astronomical Society Meeting Abstracts, 205

[165] Stickel M, et al. 2000, A&A, 359, 865

[166] Surace JA, et al. 2004, VizieR Online Data Catalog, 2255, 0

[167] Takeuchi TT, Buat V, Iglesias-Páramo J, Boselli A, Burgarella D 2005, A&A, 432, 423

[168] Tauber JA 2004, Advances in Space Research, 34, 491

[169] Taylor EL, Mann RG, Efstathiou AN, Babbedge TSR, Rowan-Robinson M, et al. 2005, MNRAS, in press, (astro-ph/0506273)

[170] Tinsley BM 1968, ApJ, 151, 547

[171] Tinsley BM, & Larson RB 1979, MNRAS, 186, 503

[172] Toomre A, & Toomre J 1972, ApJ, 178, 623

[173] Urry CM, Treister E, Van Duyne J, Bauer FE, Grogin NA, Koekemoer A, Stern D, & GOODS AGN Team 2004, American Astronomical Society Meeting Abstracts, 205

[174] Veilleux S, Kim D-C, & Sanders DB 2002, ApJS, 143, 315

[175] Vertchenko L, & Quiroga RJ 1998, A&A, 335, 894

[176] Werner MW, et al. 2004, ApJS, 154, 1

[177] Williams RE, et al. 1996, AJ, 112, 1335

[178] Willott CJ, Percival WJ, McLure RJ, Crampton D, Hutchings JB, Jarvis MJ, Sawicki M, & Simard L 2005, ApJ, 626, 657

[179] Wolf C, Meisenheimer K, Rix H-W, Borch A, Dye S, & Kleinheinrich M 2003, A&A, 401, 73

[180] Xilouris EM, Madden SC, Galliano F, Vigroux L, Sauvage M 2004, A&A, 416, 41

[181] Xu CK, Lonsdale CJ, Shupe DL, Franceschini A, Martin C, Schiminovich D 2003, ApJ, 587, 90

[182] Yan L, et al. 2004, ApJS, 154, 60

[183] Zheng XZ, Hammer F, Flores H, Assémat F, & Pelat D 2004, A&A, 421, 847

APPENDIX A

MARKOV CHAIN MONTE CARLO FITTING

We use a Markov Chain Monte Carlo (MCMC) [56] approach in order to sample the posterior parameter distributions, allowing us to both find the best solutions and the associated errors on the derived parameters. Taking $\mathbf{a}$ to be the array of parameter values defining a given model, and $\mathbf{y}$ to be the array of data values available, according to Bayes theorem, we have $p(\mathbf{a}|\mathbf{y}) \propto p(\mathbf{y}|\mathbf{a})\mathrm{p}(\mathbf{a})$ where $p(\mathbf{a}|\mathbf{y})$ is the posterior probability distribution, $p(\mathbf{y}|\mathbf{a})$ is the likelihood of the data for the given model, and $p(\mathbf{a})$ is the prior. Normalizing this (via the global probability of the data) is usually impossible in practice, since in principle it requires knowledge of all possible models. Here, as is often the case, a single model is assumed and what we are interested in is the shape of the distribution $p(\mathbf{a}|\mathbf{y})$ such that the most probable values for the parameters and their errors can be derived. What we really want then, is a measure of the relative probability of a given parameter value compared with some other value. Rearranging Bayes theorem, we have:

$$\frac{p(\mathrm{a_i}|\mathbf{y})}{p(\mathrm{a_i'}|\mathbf{y})} = \frac{p(\mathbf{y}|\mathrm{a_i})}{p(\mathbf{y}|\mathrm{a_i'})}\frac{p(\mathrm{a_i})}{p(\mathrm{a_i'})}. \tag{A.1}$$

The priors ratio is equal to 1 if a flat prior is assumed or is equal to $e^{a_i/a_i'}$ if a prior that is log-flat is chosen instead. Note that eq-n A.1 can be used to adjust the results of a chain sampled with flat priors to test the effect of other choices of priors [106]. This is the approach we take when returning to the effect of priors in Section A.1. For now flat priors are assumed for all parameters, and therefore below the posterior and likelihood distributions are used synonymously.

In principle, arbitrary shapes of the posterior distribution can be sampled using a simple Monte Carlo approach. However for multi-dimensional problems where the ratio of high-probability volume to total volume is very small, this can quickly become computationally prohibitive. The basic idea behind MCMC is to effectively sample this distribution by building up chains of random guesses of parameter values where each successive guess is chosen from some much smaller proposal distribution, q, around the previous chain link. This move is accepted or rejected according to some criterion, which both pushes the chain toward higher probability regions, and allows for some random deviation from the straight gradient descent-type path. We follow the Metropolis-Hastings algorithm [116, 68] where all parameters are varied at once, and a guess is accepted according to the criterion: $\alpha_{i+1} = \min[u, p_{i+1}q_{i+1}/p_i q_i]$, where the stochastic element is provided by the random number $u \,\epsilon\, [0, 1]$. For the proposal distribution, we use a multivariate Gaussian, which, being symmetric, leads to q_{i+1}/q_i of unity. Note that the exact shape of the proposal distribution is not important, but its effective width strongly affects the efficiency of the MCMC (see below). We assume that the likelihood of a given solution is the usual expression given by eq-n A.2.

$$\log \mathcal{L} = \text{const} - \sum \left(\frac{\mathrm{y_i} - \mathrm{y_{model}}}{\sigma_\mathrm{i}} \right)^2, \tag{A.2}$$

where the second term is the χ^2. The probability (p) that the system finds itself in a given state is given by the Boltzman factor, where the 'energy' is χ^2, and thus p_{i+1}/p_i is $\exp(-\Delta\chi^2/T)$ (this is called the 'odds' of the given solution). The temperature, T, has effectively the same function as the width of the proposal distribution in that it determines how easy it is for the system to jump a particular distance from its present state.

Since brute-force MCMC is a fairly slow procedure, rather than initialize the chain at some random point we begin with some reasonable guess at the best model (other possibilities

include simulated annealing such as used in Chapter 3, or equivalently using variable widths of the proposal distribution, or using any other optimization technique to find the high probability regions a priori). For our purposes here, starting with a reasonable guess is deemed sufficient since we still explore the full region of physically plausible solutions.

The numerical parameters which need to be set are: the width of the proposal distribution for each parameter (the q-width), the temperature, and the overall length of the chain. Too low a q-width, will tend to acceptance of too many trials, while too high a value will give some jumps far outside the high probability regions resulting in low acceptance rates. Trial-and-error has shown an acceptance ratio in the range 10–30% to be reasonable (this is supported by empirical studies which show that $\sim 25\%$ acceptance rate in problems with > 2 dimensions minimizes internal correlations in the resulting chain [143]). To find the appropriate q-width, we make shorter (30,000) runs where we vary only one parameter at a time. We start with a guess at the q-widths for each and incrementally adjust them until the resulting acceptance rates are 50–80% (which is appropriate for 1-dimensional problems). By trial and error we have found that this leads to acceptance rates in the desired 10-30% range when all seven parameters are varied simultaneously. This approach works better for our sample than fixing the widths a priori, since the dynamic range for the various parameters is too high. Such optimization of the proposal distributions before the main run speeds up the process, while preserving the ergodicity of the MCMC algorithm [57]. We set T to 0.9, which results in points $\Delta\chi^2 \sim 1$ away from the best solution to be accepted with 30% probability. Note however, that since increasing the temperature increases the acceptance rate as well (preserving the $\Delta\chi^2/T$ ratio) and vice versa, in principle the temperature and q-width are degenerate and therefore the exact value of the temperature chosen is not crucial as it will be compensated for in the above width adjustment.

For the overall length of the chain, we need to find the length which both samples well the posterior probability distribution and at the same time for practical reasons is not much longer than just needed to accomplish this. We use 600,000 iterations, since our experience shows that the posterior probability around the best solution is well-sampled by this time.

This procedure still leaves us with little sensitivity to highly disjointed solutions of equal goodness-of-fit, although this is not of concern here as such solutions will most likely converge onto unphyiscal values. Since we start at a high-probability part of the parameter space, the 'burn-in' period is less well defined than when starting at a random position, and we therefore do not formaly subtract a 'burn-in' part of the chain (however in deriving the best-fit parameters and errors below we apply a cut of $\Delta\chi^2 = 5$ from the minimum χ^2 solution which isolates the region of interest and thus has the same function as the 'burn-in' removal). Fig. A.1 shows an example of the resulting chain in various projections.

A.1 Error estimates

As discussed above, the MCMC procedure samples the likelihood surface, which is proportional to the posterior probability distribution of interest. We use flat priors, where negative values are not accepted for all parameters. In addition, upper limits are set for the temperature (100 K), optical depth (30), and β (3). The latter is necessary, since for many sources the SNR in the sub-mm data is very low, leading to the difference in overall χ^2's for unphysically large values of β to be small, and the chain can get stuck in such regions. Since β is believed both on theoretical and observational grounds to be in the range $\sim 1-2$ (see [46] and references therein), we believe our $0-3$ prior is reasonable. The temperature limit is also necessary because of the above difference in SNR. The optical depth limit is only relevant for the few sources with higher τ and

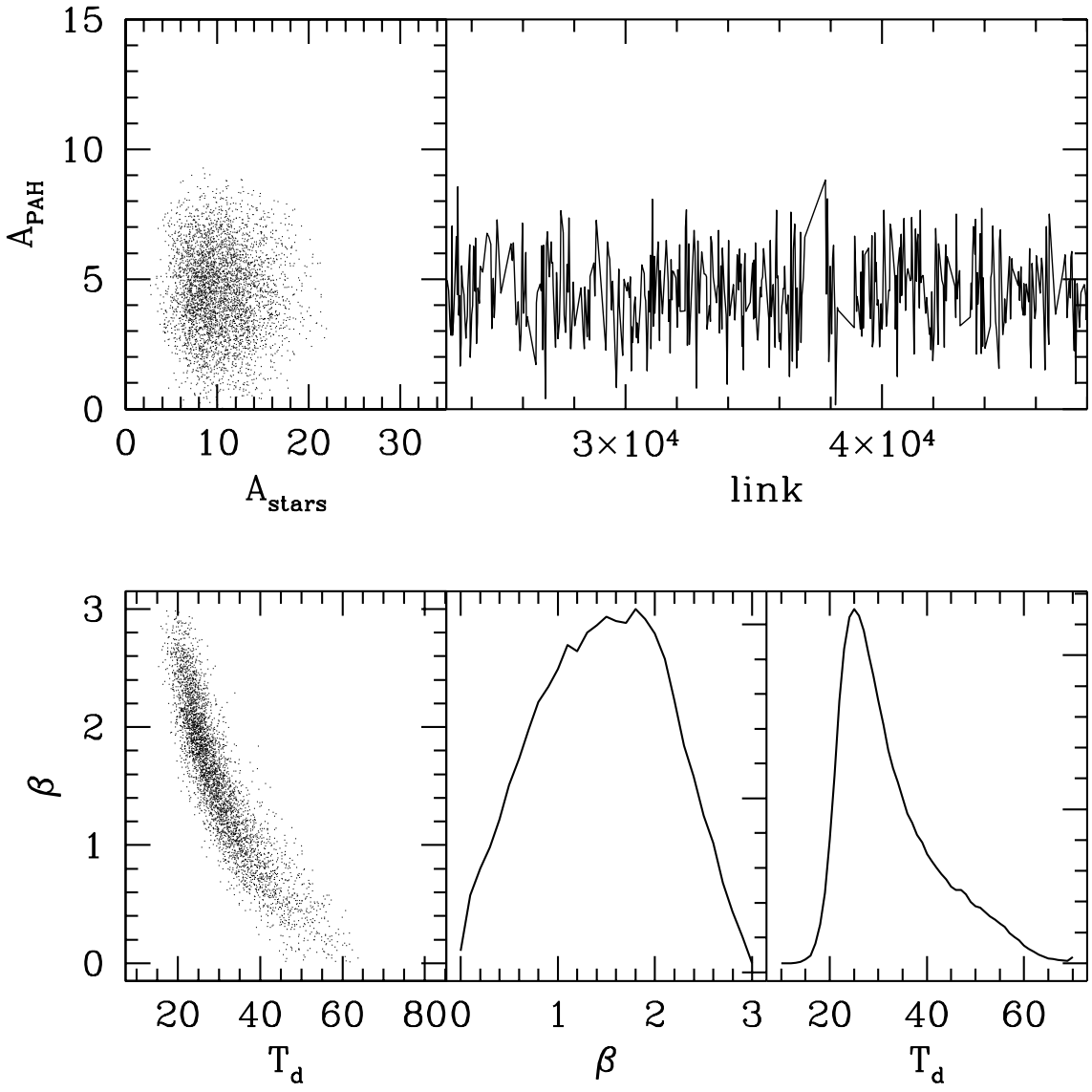

Fig. A.1: Here we demonstrate what the resulting chain looks like after the above procedure. The two left-most panels show examples of both uncorrelated and correlated parameters. A thinning factor of 30 has been applied. Throughout we plot all points with $\chi^2 \leq (\chi^2_{\rm min} + 5)$. The top right panel shows a section of the chain demonstrating the evolution of the PAH amplitude parameters. The bottom middle/right panels show the marginalized distribution for the β and $T_{\rm d}$ parameters. Note the non-Gaussian shapes.

faint near-IR/IRAC detections (e.g. N1-040, N1-064). These limits are imposed by returning the chain to the vicinity of its initial state in order to avoid getting stuck at the edge. We come back to the effects of the prior below.

The chains obtained above allow for two distinct routes to obtaining the probability distributions for each parameter. The first is the easier straight marginalization of the given parameter over all the others. This is given by:

$$p(a_j)da_j = \int_{i,i\neq j}^{N_i} p(a_i)da_i, \tag{A.3}$$

which in practice is just counting the number of times the chain visits a particular bin of values for the given parameter a_j. However, since we record the χ^2 value for each chain link, we can also directly obtain the likelihood distribution (see eq-n A.2) for the parameter. In practice, a simplified form of this is the mean likelihood distribution [106]. The idea is to calculate the average χ^2 for each bin and then compare this with the minimum χ^2 achieved by the chain as

$$p(a_j) \propto \exp[-(\chi_j^2 - \chi_{\rm min}^2)], \tag{A.4}$$

where χ_j^2 is the mean χ^2 in the j^{th} bin.

In Figs. A.2 – A.7, we show the distributions for all parameters obtained using both methods for the whole sample. Note that since we have applied a χ^2 cut (see above), secondary features in the marginalized distributions, such as blended peaks and tails, are still fairly likely. For example, in the case of N1-101 $T_{\rm d} \sim 25\,{\rm K}$ is the preferred solution, but $T_{\rm d} \sim 40\,{\rm K}$ is still quite likely. The uneven error-bars indicate this. Note that in Table 4.2 for simplicity, we quote the average error only, but indicate the different error-bars in the figures. However, that due to its definition, applying a χ^2 cut when estimating the mean likelihood tends to flatten the distributions. Therefore in that case, the most 'peaked' distributions possible are obtained if

the whole of the chains are used. In that case, parameters poorly constrained by the χ^2 are clearly visible in the likelihood curves (e.g. $L_{\rm PAH}$ for the highest-z sources N1-064, and N1-078).

The best-fit values we use are merely the peak of the above distributions. To obtain the uncertainties on those we define a desired confidence level and, starting from the peak of the distribution, move to incrementally lower equal probability bins on each side of it until the area covered is equal to the total area times the desired confidence level. Thus unsymmetric errorbars are indicative of asymmetric probability distributions.

From Fig. A.2 and Fig. A.3, we see that in general the marginalized and mean likelihood distirbutions agree reasonably well with each other. There are two instances where the two disagree substantially. One is for β, where likelihood tends toward unphysically high values. The origins of this were discussed in Chapter 4. The imposed prior confines the marginalized distribution to more reasonable values. We also find significant difference between the two approaches for τ_V. Here we are again clearly affected by our choice of prior. Fig. A.8 shows how our uniform prior-based distribution transforms into the mean likelihood distribution by application of the Jeffreys prior [63] to the same. Note that the offsets in the PAH luminosity and stellar mass values are also due to this difference.

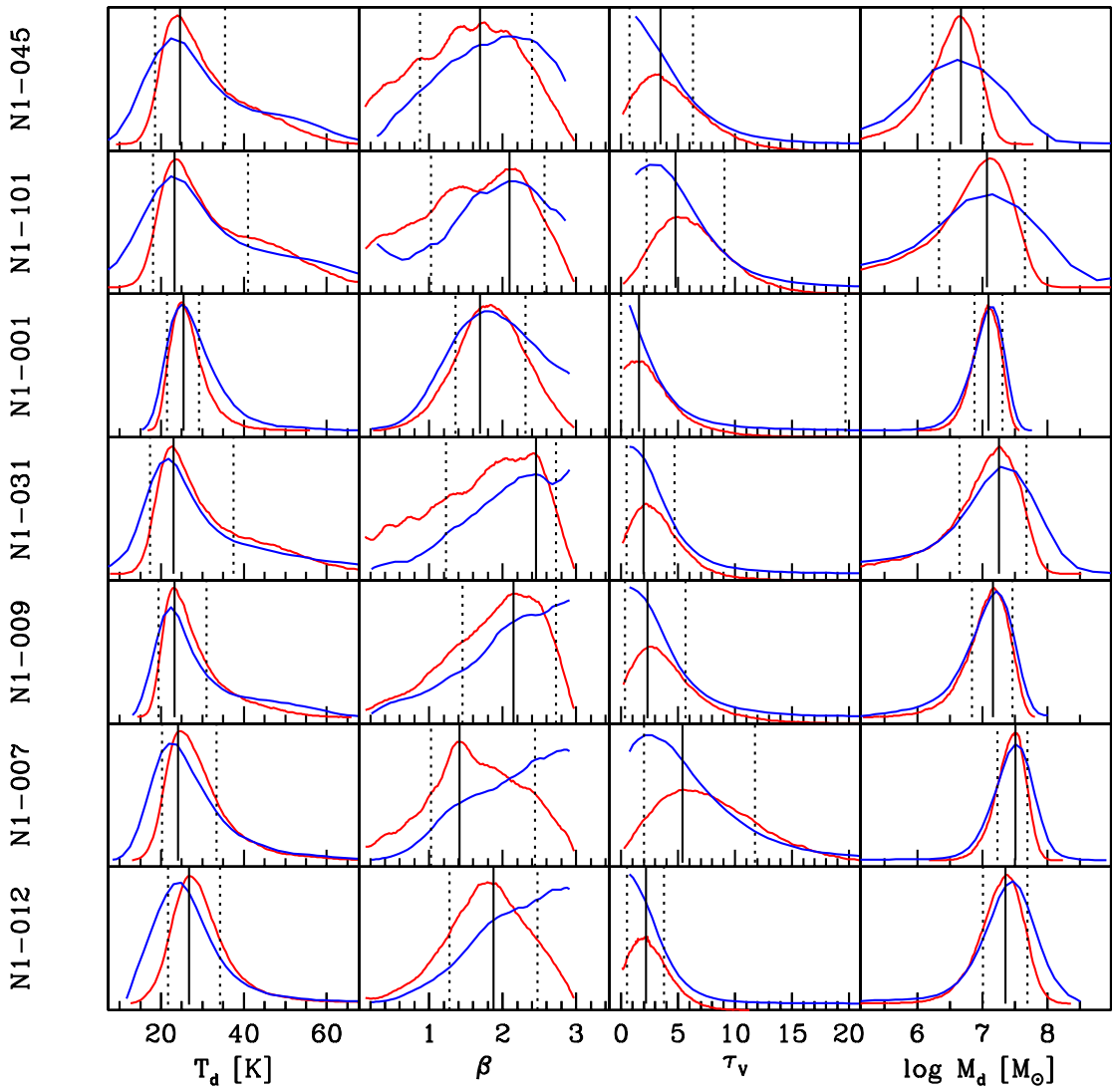

Fig. A.2: Here we compare the marginalized (red curve) and mean likelihood (blue curve) derived probability distributions for the parameters of interest. The distributions are normalized and the plots scaled to just fit the distributions as shown. The sources here and in the following figures are orders in increasing $L_{\rm IR}$. We use the marginalized distribution for our error estimates, where the best-fit value is given by the solid line (simply the peak of the distribution), and the 68% confidence limits are given by the dotted line.

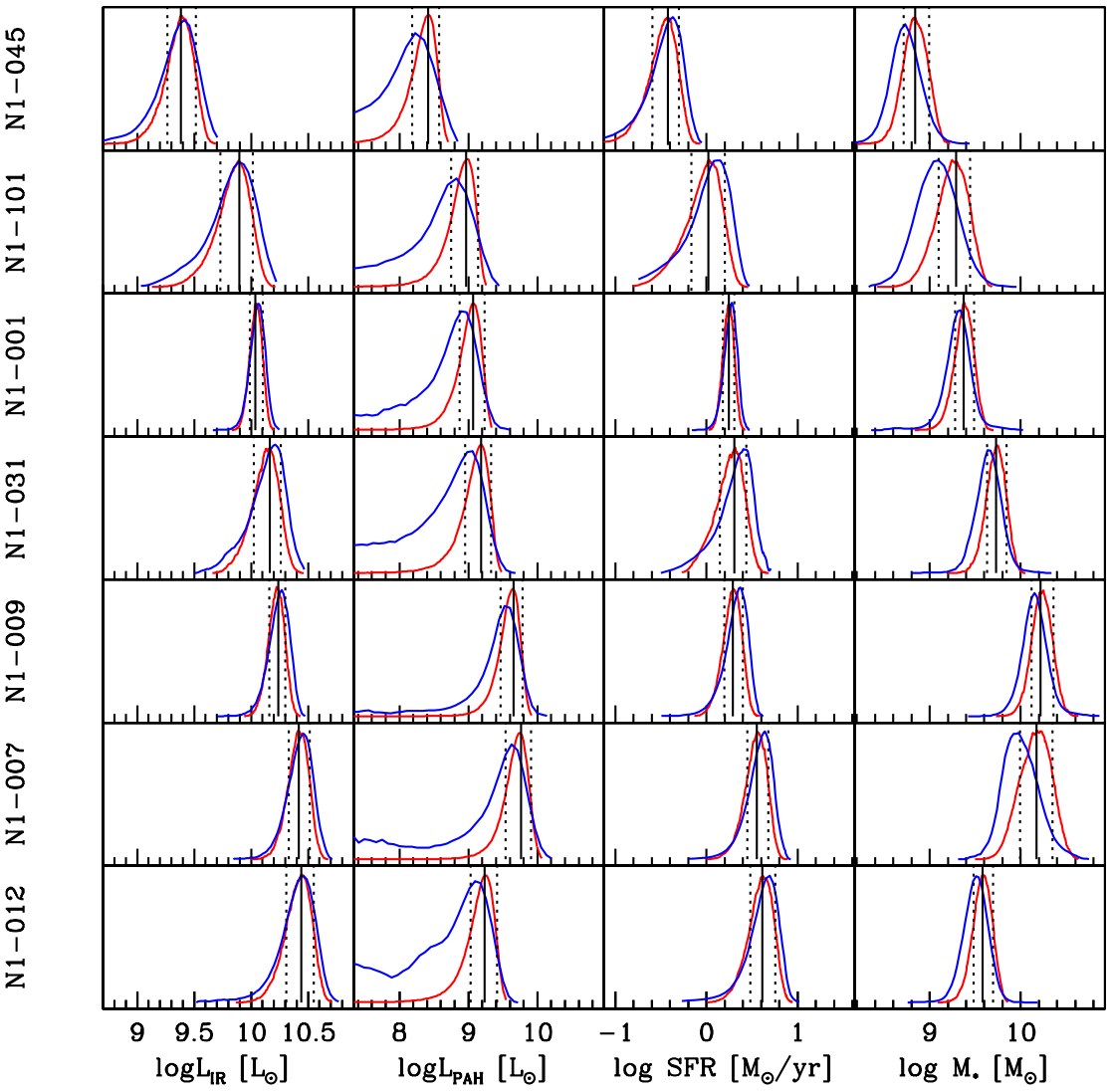

Fig. A.3: Same as Figure A.2 for the remainder of the parameters.

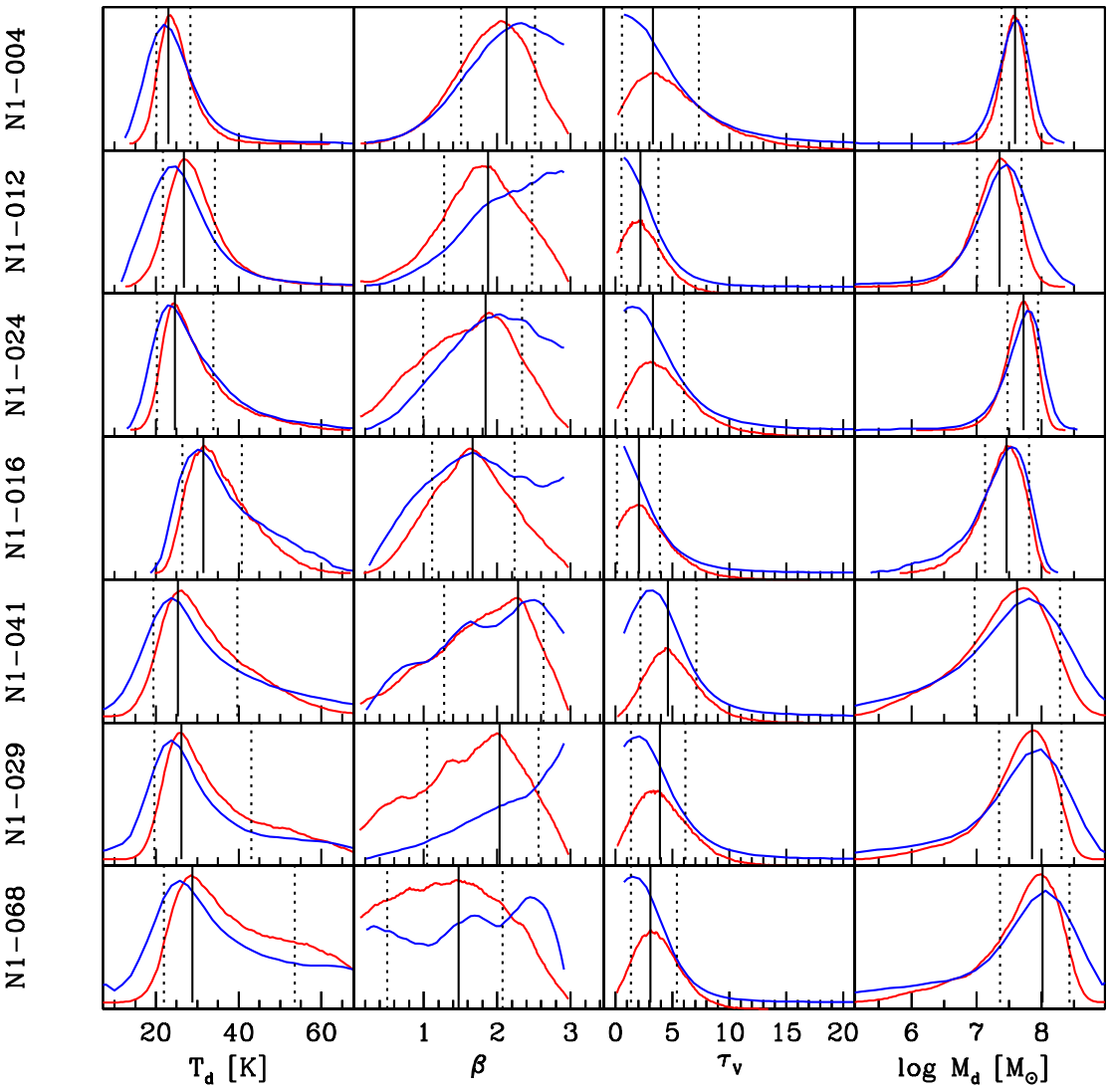

Fig. A.4: Same as Figure A.2 for the remainder of the parameters.

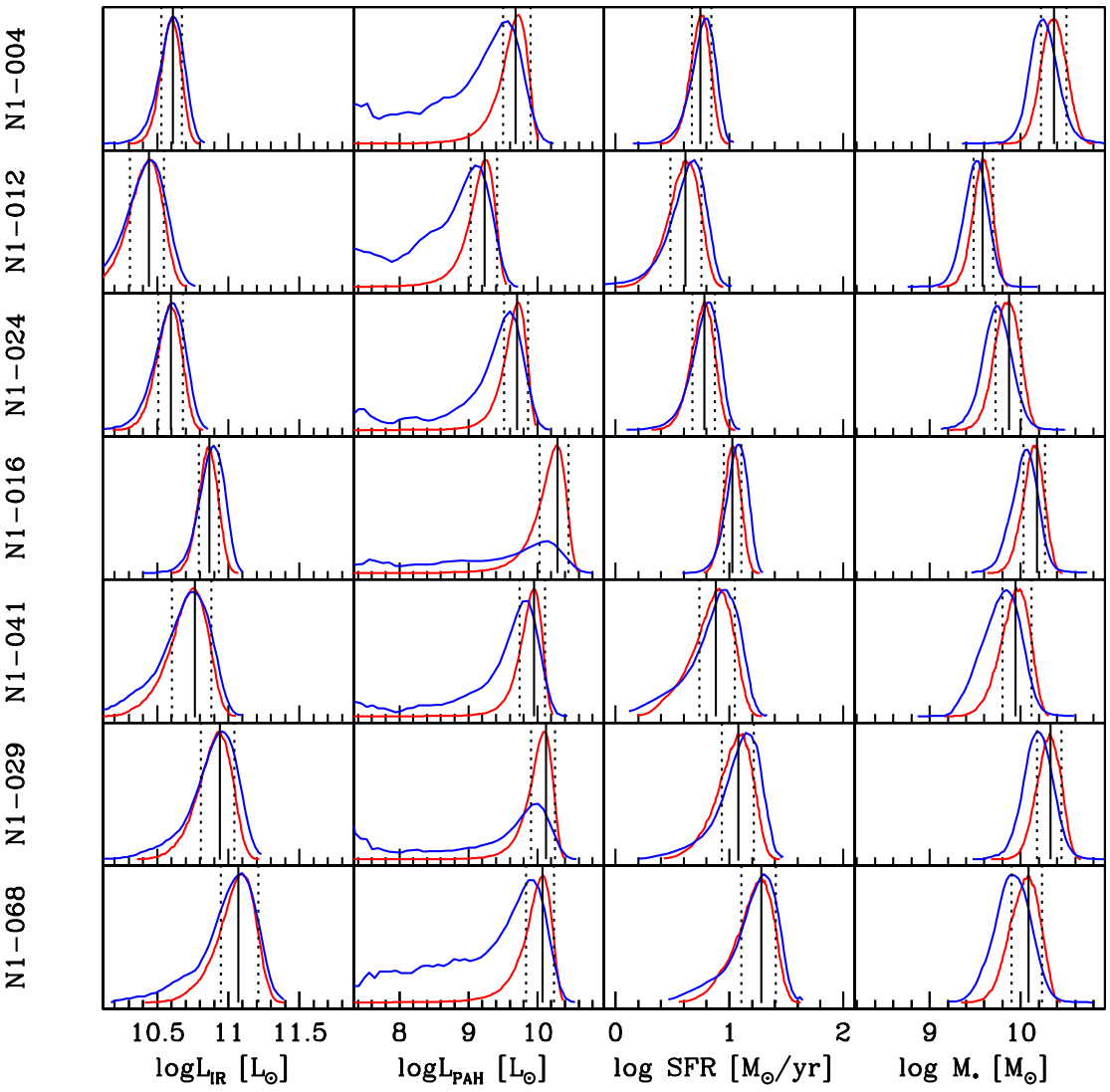

Fig. A.5: Same as Figure A.2 for the remainder of the parameters.

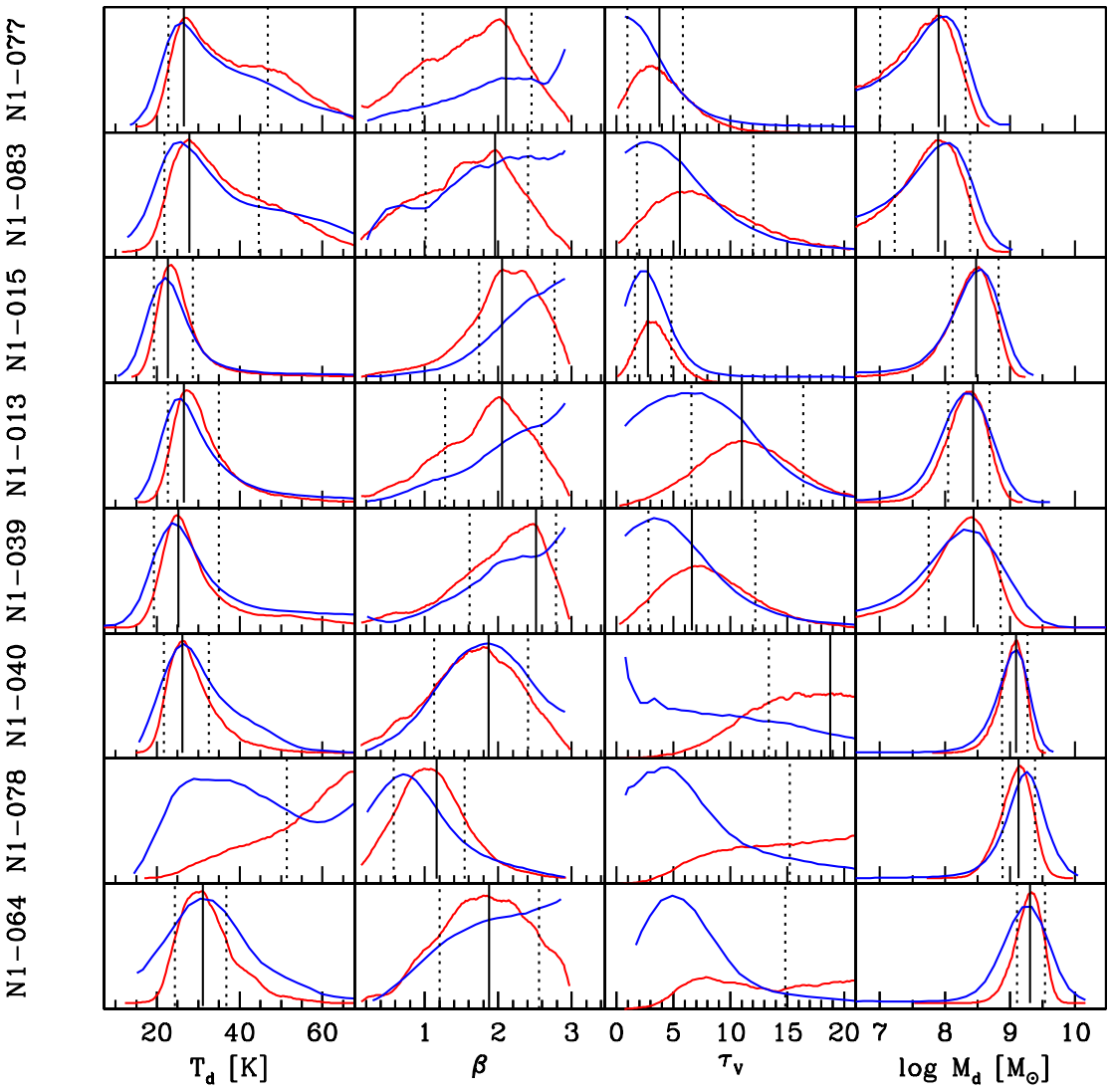

Fig. A.6: Same as Figure A.2 for the remainder of the parameters.

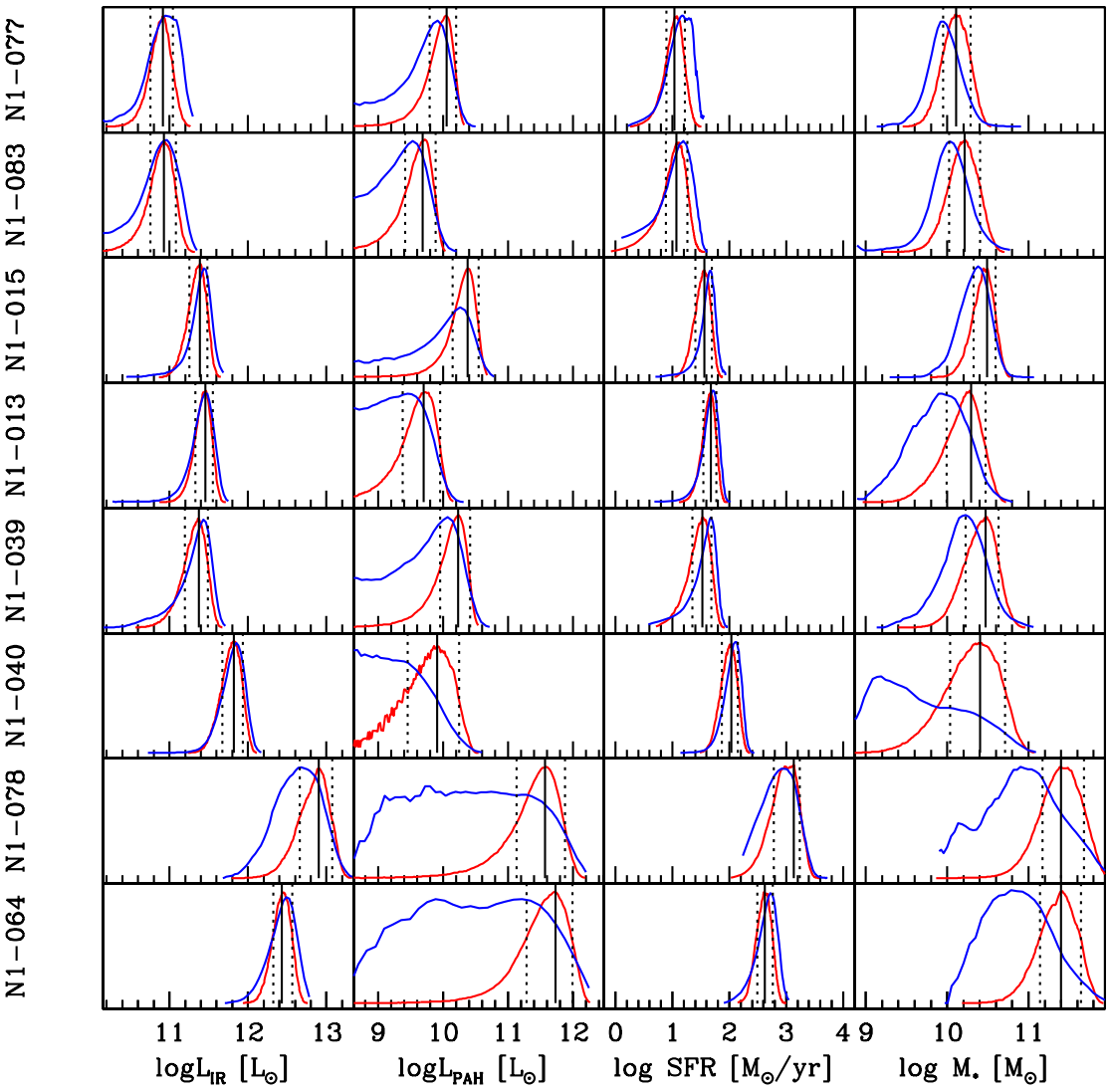

Fig. A.7: Same as Figure A.2 for the remainder of the parameters.

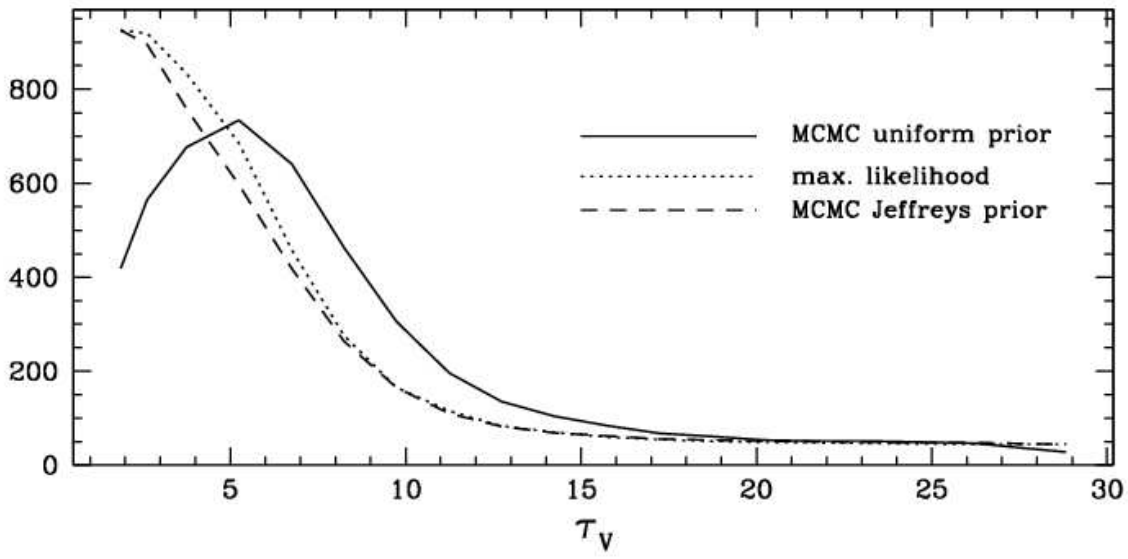

Fig. A.8: The effect of choice of prior on the τ_V probability distribution. Here we use the chain for N1-041.